

Heavy Quark Production in $p + p$ and Energy Loss and Flow of Heavy Quarks in Au+Au Collisions at $\sqrt{s_{NN}} = 200$ GeV

A. Adare,⁹ S. Afanasiev,²³ C. Aidala,¹⁰ N.N. Ajitanand,⁵⁰ Y. Akiba,^{44,45} H. Al-Bataineh,³⁹ J. Alexander,⁵⁰
A. Al-Jamel,³⁹ K. Aoki,^{29,44} L. Aphecetche,⁵² R. Armendariz,³⁹ S.H. Aronson,⁴ J. Asai,⁴⁵ E.T. Atomssa,³⁰
R. Averbeck,⁵¹ T.C. Awes,⁴⁰ B. Azmoun,⁴ V. Babintsev,¹⁹ G. Baksay,¹⁵ L. Baksay,¹⁵ A. Baldissieri,¹² K.N. Barish,⁵
P.D. Barnes,³² B. Bassalleck,³⁸ S. Bathe,⁵ S. Batsouli,^{10,40} V. Baublis,⁴³ F. Bauer,⁵ A. Bazilevsky,⁴
S. Belikov,^{4,22,*} R. Bennett,⁵¹ Y. Berdnikov,⁴⁷ A.A. Bickley,⁹ M.T. Bjornrdal,¹⁰ J.G. Boissevain,³² H. Borel,¹²
K. Boyle,⁵¹ M.L. Brooks,³² D.S. Brown,³⁹ D. Bucher,³⁵ H. Buesching,⁴ V. Bumazhnov,¹⁹ G. Bunce,^{4,45}
J.M. Burward-Hoy,³² S. Butsyk,^{32,51} S. Campbell,⁵¹ J.-S. Chai,²⁴ B.S. Chang,⁵⁹ J.-L. Charvet,¹² S. Chernichenko,¹⁹
J. Chiba,²⁵ C.Y. Chi,¹⁰ M. Chiu,^{10,20} I.J. Choi,⁵⁹ T. Chujo,⁵⁶ P. Chung,⁵⁰ A. Churnyn,¹⁹ V. Cianciolo,⁴⁰
C.R. Clevén,¹⁷ Y. Cobigo,¹² B.A. Cole,¹⁰ M.P. Comets,⁴¹ P. Constantin,^{22,32} M. Csanád,¹⁴ T. Csörgő,²⁶
T. Dahms,⁵¹ K. Das,¹⁶ G. David,⁴ M.B. Deaton,¹ K. Dehmelt,¹⁵ H. Delagrange,⁵² A. Denisov,¹⁹ D. d'Enterria,¹⁰
A. Deshpande,^{45,51} E.J. Desmond,⁴ O. Dietzsch,⁴⁸ A. Dion,⁵¹ M. Donadelli,⁴⁸ J.L. Drachenberg,¹ O. Drapier,³⁰
A. Drees,⁵¹ A.K. Dubey,⁵⁸ A. Durum,¹⁹ V. Dzhordzhadze,^{5,53} Y.V. Efremenko,⁴⁰ J. Egdemir,⁵¹ F. Ellinghaus,⁹
W.S. Emam,⁵ A. Enokizono,^{18,31} H. En'yo,^{44,45} B. Espagnon,⁴¹ S. Esumi,⁵⁵ K.O. Eyser,⁵ D.E. Fields,^{38,45}
M. Finger, Jr.,^{6,23} M. Finger,^{6,23} F. Fleuret,³⁰ S.L. Fokin,²⁸ B. Forestier,³³ Z. Fraenkel,^{58,*} J.E. Frantz,^{10,51}
A. Franz,⁴ A.D. Frawley,¹⁶ K. Fujiwara,⁴⁴ Y. Fukao,^{29,44} S.-Y. Fung,⁵ T. Fusayasu,³⁷ S. Gadrat,³³
I. Garishvili,⁵³ F. Gastineau,⁵² M. Germain,⁵² A. Glenn,^{9,53} H. Gong,⁵¹ M. Gonin,³⁰ J. Gosset,¹² Y. Goto,^{44,45}
R. Granier de Cassagnac,³⁰ N. Grau,²² S.V. Greene,⁵⁶ M. Grosse Perdekamp,^{20,45} T. Gunji,⁸ H.-Å. Gustafsson,^{34,*}
T. Hachiyu,^{18,44} A. Hadj Henni,⁵² C. Haegemann,³⁸ J.S. Haggerty,⁴ M.N. Hagiwara,¹ H. Hamagaki,⁸ R. Han,⁴²
H. Harada,¹⁸ E.P. Hartouni,³¹ K. Haruna,¹⁸ M. Harvey,⁴ E. Haslum,³⁴ K. Hasuko,⁴⁴ R. Hayano,⁸ M. Heffner,³¹
T.K. Hemmick,⁵¹ T. Hester,⁵ J.M. Heuser,⁴⁴ X. He,¹⁷ H. Hiejima,²⁰ J.C. Hill,²² R. Hobbs,³⁸ M. Hohlmann,¹⁵
M. Holmes,⁵⁶ W. Holzmann,⁵⁰ K. Homma,¹⁸ B. Hong,²⁷ T. Horaguchi,^{44,54} D. Hornback,⁵³ M.G. Hur,²⁴
T. Ichihara,^{44,45} H. Inuma,^{29,44} K. Imai,^{29,44} M. Inaba,⁵⁵ Y. Inoue,^{46,44} D. Isenhower,¹ L. Isenhower,¹
M. Ishihara,⁴⁴ T. Isobe,⁸ M. Issah,⁵⁰ A. Isupov,²³ B.V. Jacak,^{51,†} J. Jia,¹⁰ J. Jin,¹⁰ O. Jinnouchi,⁴⁵ B.M. Johnson,⁴
K.S. Joo,³⁶ D. Jouan,⁴¹ F. Kajihara,^{8,44} S. Kametani,^{8,57} N. Kamihara,^{44,54} J. Kamin,⁵¹ M. Kaneta,⁴⁵ J.H. Kang,⁵⁹
H. Kanou,^{44,54} T. Kawagishi,⁵⁵ D. Kawall,⁴⁵ A.V. Kazantsev,²⁸ S. Kelly,⁹ A. Khanzadeev,⁴³ J. Kikuchi,⁵⁷
D.H. Kim,³⁶ D.J. Kim,⁵⁹ E. Kim,⁴⁹ Y.-S. Kim,²⁴ E. Kinney,⁹ Á. Kiss,¹⁴ E. Kistenev,⁴ A. Kiyomichi,⁴⁴ J. Klay,³¹
C. Klein-Boesing,³⁵ L. Kochenda,⁴³ V. Kochetkov,¹⁹ B. Komkov,⁴³ M. Konno,⁵⁵ D. Kotchetkov,⁵ A. Kozlov,⁵⁸
A. Král,¹¹ A. Kravitz,¹⁰ P.J. Kroon,⁴ J. Kubart,^{6,21} G.J. Kunde,³² N. Kurihara,⁸ K. Kurita,^{46,44} M.J. Kweon,²⁷
Y. Kwon,^{53,59} G.S. Kyle,³⁹ R. Lacey,⁵⁰ Y.S. Lai,¹⁰ J.G. Lajoie,²² A. Lebedev,²² Y. Le Bornec,⁴¹ S. Leckey,⁵¹
D.M. Lee,³² M.K. Lee,⁵⁹ T. Lee,⁴⁹ M.J. Leitch,³² M.A.L. Leite,⁴⁸ B. Lenzi,⁴⁸ H. Lim,⁴⁹ T. Liška,¹¹ A. Litvinenko,²³
M.X. Liu,³² X. Li,⁷ X.H. Li,⁵ B. Love,⁵⁶ D. Lynch,⁴ C.F. Maguire,⁵⁶ Y.I. Makdisi,^{3,4} A. Malakhov,²³ M.D. Malik,³⁸
V.I. Manko,²⁸ Y. Mao,^{42,44} L. Mašek,^{6,21} H. Masui,⁵⁵ F. Matathias,^{10,51} M.C. McCain,²⁰ M. McCumber,⁵¹
P.L. McGaughey,³² Y. Miake,⁵⁵ P. Mikeš,^{6,21} K. Miki,⁵⁵ T.E. Miller,⁵⁶ A. Milov,⁵¹ S. Mioduszewski,⁴
G.C. Mishra,¹⁷ M. Mishra,² J.T. Mitchell,⁴ M. Mitrovski,⁵⁰ A. Morreale,⁵ D.P. Morrison,⁴ J.M. Moss,³²
T.V. Moukhanova,²⁸ D. Mukhopadhyay,⁵⁶ J. Murata,^{46,44} S. Nagamiya,²⁵ Y. Nagata,⁵⁵ J.L. Nagle,⁹ M. Naglis,⁵⁸
I. Nakagawa,^{44,45} Y. Nakamiya,¹⁸ T. Nakamura,¹⁸ K. Nakano,^{44,54} J. Newby,³¹ M. Nguyen,⁵¹ B.E. Norman,³²
R. Nouicer,⁴ A.S. Nyanin,²⁸ J. Nystrand,³⁴ E. O'Brien,⁴ S.X. Oda,⁸ C.A. Ogilvie,²² H. Ohnishi,⁴⁴ I.D. Ojha,⁵⁶
K. Okada,⁴⁵ M. Oka,⁵⁵ O.O. Omiwade,¹ A. Oskarsson,³⁴ I. Otterlund,³⁴ M. Ouchida,¹⁸ K. Ozawa,⁸ R. Pak,⁴
D. Pal,⁵⁶ A.P.T. Palounek,³² V. Pantuev,⁵¹ V. Papavassiliou,³⁹ J. Park,⁴⁹ W.J. Park,²⁷ S.F. Pate,³⁹ H. Pei,²²
J.-C. Peng,²⁰ H. Pereira,¹² V. Peresedov,²³ D.Yu. Peressounko,²⁸ C. Pinkenburg,⁴ R.P. Pisani,⁴ M.L. Purschke,⁴
A.K. Purwar,^{32,51} H. Qu,¹⁷ J. Rak,^{22,38} A. Rakotozafindrabe,³⁰ I. Ravinovich,⁵⁸ K.F. Read,^{40,53} S. Rembeczki,¹⁵
M. Reuter,⁵¹ K. Reygers,³⁵ V. Riabov,⁴³ Y. Riabov,⁴³ G. Roche,³³ A. Romana,^{30,*} M. Rosati,²² S.S.E. Rosendahl,³⁴
P. Rosnet,³³ P. Rukoyatkin,²³ V.L. Rykov,⁴⁴ S.S. Ryu,⁵⁹ B. Sahlmueller,³⁵ N. Saito,^{29,44,45} T. Sakaguchi,^{4,8,57}
S. Sakai,⁵⁵ H. Sakata,¹⁸ V. Samsonov,⁴³ H.D. Sato,^{29,44} S. Sato,^{4,25,55} S. Sawada,²⁵ J. Seele,⁹ R. Seidl,²⁰
V. Semenov,¹⁹ R. Seto,⁵ D. Sharma,⁵⁸ T.K. Shea,⁴ I. Shein,¹⁹ A. Shevel,^{43,50} T.-A. Shibata,^{44,54} K. Shigaki,¹⁸
M. Shimomura,⁵⁵ T. Shohjoh,⁵⁵ K. Shoji,^{29,44} A. Sickles,⁵¹ C.L. Silva,⁴⁸ D. Silvermyr,⁴⁰ C. Silvestre,¹² K.S. Sim,²⁷
C.P. Singh,² V. Singh,² S. Skutnik,²² M. Slunečka,^{6,23} W.C. Smith,¹ A. Soldatov,¹⁹ R.A. Soltz,³¹ W.E. Sondheim,³²
S.P. Sorensen,⁵³ I.V. Sourikova,⁴ F. Staley,¹² P.W. Stankus,⁴⁰ E. Stenlund,³⁴ M. Stepanov,³⁹ A. Ster,²⁶
S.P. Stoll,⁴ T. Sugitate,¹⁸ C. Suire,⁴¹ J.P. Sullivan,³² J. Sziklai,²⁶ T. Tabaru,⁴⁵ S. Takagi,⁵⁵ E.M. Takagui,⁴⁸
A. Taketani,^{44,45} K.H. Tanaka,²⁵ Y. Tanaka,³⁷ K. Tanida,^{44,45,49} M.J. Tannenbaum,⁴ A. Taranenko,⁵⁰ P. Tarján,¹³

T.L. Thomas,³⁸ M. Togawa,^{29,44} A. Toia,⁵¹ J. Tojo,⁴⁴ L. Tomášek,²¹ H. Torii,⁴⁴ R.S. Towell,¹ V-N. Tram,³⁰ I. Tserruya,⁵⁸ Y. Tsuchimoto,^{18,44} S.K. Tuli,² H. Tydesjö,³⁴ N. Tyurin,¹⁹ C. Vale,²² H. Valle,⁵⁶ H.W. van Hecke,³² J. Velkovska,⁵⁶ R. Vértesi,¹³ A.A. Vinogradov,²⁸ M. Virius,¹¹ V. Vrba,²¹ E. Vznuzdaev,⁴³ M. Wagner,^{29,44} D. Walker,⁵¹ X.R. Wang,³⁹ Y. Watanabe,^{44,45} J. Wessels,³⁵ S.N. White,⁴ N. Willis,⁴¹ D. Winter,¹⁰ C.L. Woody,⁴ M. Wysocki,⁹ W. Xie,^{5,45} Y.L. Yamaguchi,⁵⁷ A. Yanovich,¹⁹ Z. Yasin,⁵ J. Ying,¹⁷ S. Yokkaichi,^{44,45} G.R. Young,⁴⁰ I. Younus,³⁸ I.E. Yushmanov,²⁸ W.A. Zajc,¹⁰ O. Zaudtke,³⁵ C. Zhang,^{10,40} S. Zhou,⁷ J. Zimányi,^{26,*} and L. Zolin²³

(PHENIX Collaboration)

¹Abilene Christian University, Abilene, Texas 79699, USA

²Department of Physics, Banaras Hindu University, Varanasi 221005, India

³Collider-Accelerator Department, Brookhaven National Laboratory, Upton, New York 11973-5000, USA

⁴Brookhaven National Laboratory, Upton, New York 11973-5000, USA

⁵University of California - Riverside, Riverside, California 92521, USA

⁶Charles University, Ovocný trh 5, Praha 1, 116 36, Prague, Czech Republic

⁷China Institute of Atomic Energy (CIAE), Beijing, People's Republic of China

⁸Center for Nuclear Study, Graduate School of Science, University of Tokyo, 7-3-1 Hongo, Bunkyo, Tokyo 113-0033, Japan

⁹University of Colorado, Boulder, Colorado 80309, USA

¹⁰Columbia University, New York, New York 10027 and Nevis Laboratories, Irvington, New York 10533, USA

¹¹Czech Technical University, Zikova 4, 166 36 Prague 6, Czech Republic

¹²Dapnia, CEA Saclay, F-91191, Gif-sur-Yvette, France

¹³Debrecen University, H-4010 Debrecen, Egyetem tér 1, Hungary

¹⁴ELTE, Eötvös Loránd University, H - 1117 Budapest, Pázmány P. s. 1/A, Hungary

¹⁵Florida Institute of Technology, Melbourne, Florida 32901, USA

¹⁶Florida State University, Tallahassee, Florida 32306, USA

¹⁷Georgia State University, Atlanta, Georgia 30303, USA

¹⁸Hiroshima University, Kagamiyama, Higashi-Hiroshima 739-8526, Japan

¹⁹IHEP Protvino, State Research Center of Russian Federation, Institute for High Energy Physics, Protvino, 142281, Russia

²⁰University of Illinois at Urbana-Champaign, Urbana, Illinois 61801, USA

²¹Institute of Physics, Academy of Sciences of the Czech Republic, Na Slovance 2, 182 21 Prague 8, Czech Republic

²²Iowa State University, Ames, Iowa 50011, USA

²³Joint Institute for Nuclear Research, 141980 Dubna, Moscow Region, Russia

²⁴KAERI, Cyclotron Application Laboratory, Seoul, Korea

²⁵KEK, High Energy Accelerator Research Organization, Tsukuba, Ibaraki 305-0801, Japan

²⁶KFKI Research Institute for Particle and Nuclear Physics of the Hungarian Academy of Sciences (MTA KFKI RMKI), H-1525 Budapest 114, POBox 49, Budapest, Hungary

²⁷Korea University, Seoul, 136-701, Korea

²⁸Russian Research Center "Kurchatov Institute", Moscow, Russia

²⁹Kyoto University, Kyoto 606-8502, Japan

³⁰Laboratoire Leprince-Ringuet, Ecole Polytechnique, CNRS-IN2P3, Route de Saclay, F-91128, Palaiseau, France

³¹Lawrence Livermore National Laboratory, Livermore, California 94550, USA

³²Los Alamos National Laboratory, Los Alamos, New Mexico 87545, USA

³³LPC, Université Blaise Pascal, CNRS-IN2P3, Clermont-Fd, 63177 Aubiere Cedex, France

³⁴Department of Physics, Lund University, Box 118, SE-221 00 Lund, Sweden

³⁵Institut für Kernphysik, University of Muenster, D-48149 Muenster, Germany

³⁶Myongji University, Yongin, Kyonggido 449-728, Korea

³⁷Nagasaki Institute of Applied Science, Nagasaki-shi, Nagasaki 851-0193, Japan

³⁸University of New Mexico, Albuquerque, New Mexico 87131, USA

³⁹New Mexico State University, Las Cruces, New Mexico 88003, USA

⁴⁰Oak Ridge National Laboratory, Oak Ridge, Tennessee 37831, USA

⁴¹IPN-Orsay, Université Paris Sud, CNRS-IN2P3, BP1, F-91406, Orsay, France

⁴²Peking University, Beijing, People's Republic of China

⁴³PNPI, Petersburg Nuclear Physics Institute, Gatchina, Leningrad region, 188300, Russia

⁴⁴RIKEN Nishina Center for Accelerator-Based Science, Wako, Saitama 351-0198, JAPAN

⁴⁵RIKEN BNL Research Center, Brookhaven National Laboratory, Upton, New York 11973-5000, USA

⁴⁶Physics Department, Rikkyo University, 3-34-1 Nishi-Ikebukuro, Toshima, Tokyo 171-8501, Japan

⁴⁷Saint Petersburg State Polytechnic University, St. Petersburg, Russia

⁴⁸Universidade de São Paulo, Instituto de Física, Caixa Postal 66318, São Paulo CEP05315-970, Brazil

⁴⁹System Electronics Laboratory, Seoul National University, Seoul, Korea

⁵⁰Chemistry Department, Stony Brook University, Stony Brook, SUNY, New York 11794-3400, USA

⁵¹Department of Physics and Astronomy, Stony Brook University, SUNY, Stony Brook, New York 11794, USA

⁵²SUBATECH (Ecole des Mines de Nantes, CNRS-IN2P3, Université de Nantes) BP 20722 - 44307, Nantes, France

⁵³University of Tennessee, Knoxville, Tennessee 37996, USA

⁵⁴Department of Physics, Tokyo Institute of Technology, Oh-okayama, Meguro, Tokyo 152-8551, Japan

⁵⁵*Institute of Physics, University of Tsukuba, Tsukuba, Ibaraki 305, Japan*

⁵⁶*Vanderbilt University, Nashville, Tennessee 37235, USA*

⁵⁷*Waseda University, Advanced Research Institute for Science and Engineering, 17 Kikui-cho, Shinjuku-ku, Tokyo 162-0044, Japan*

⁵⁸*Weizmann Institute, Rehovot 76100, Israel*

⁵⁹*Yonsei University, IPAP, Seoul 120-749, Korea*

(Dated: November 1, 2018)

Transverse momentum (p_T^e) spectra of electrons from semileptonic weak decays of heavy flavor mesons in the range of $0.3 < p_T^e < 9.0$ GeV/ c have been measured at midrapidity ($|\eta| < 0.35$) by the PHENIX experiment at the Relativistic Heavy Ion Collider in $p+p$ and Au+Au collisions at $\sqrt{s_{NN}} = 200$ GeV. In addition, the azimuthal anisotropy parameter v_2 has been measured for $0.3 < p_T^e < 5.0$ GeV/ c in Au+Au collisions. The nuclear modification factor R_{AA} with respect to $p+p$ collisions indicates substantial energy loss of heavy quarks in the produced medium. Comparisons of R_{AA} and v_2 are made to various model calculations.

PACS numbers: 25.75.Dw

I. INTRODUCTION

Numerous experimental results from the Relativistic Heavy Ion Collider (RHIC) at Brookhaven National Laboratory (BNL) have firmly established that the matter created in central Au+Au collisions at $\sqrt{s_{NN}} = 200$ GeV cannot be explained by the common expectation of a weakly interacting gas of quarks and gluons at very high densities [1–4]. Strong suppression observed in measurements of the nuclear modification factor $R_{AuAu}(p_T)$ for light-flavor hadrons shows that high- p_T scattered partons suffer a significant energy-loss in the medium [5–7]. The large magnitude of the differential elliptic flow parameter $v_2(p_T)$ and its p_T and mass dependencies measured in a limited phase space approximately agree with the theoretical predictions based on an ideal hydrodynamic fluid [8–11]. In addition, the observation of universal scaling of v_2 for various hadrons suggests that the flow pattern is established at the partonic level before hadronization [12]. These experiments indicate that the medium is strongly interacting and exhibits hydrodynamic behavior.

However, it has been pointed out that qualitative evidence for a near-perfect hydrodynamic fluid is not sufficient in terms of thermodynamic and transport concepts [13, 14]. The issue is how perfect is the near-perfect fluidity observed at RHIC. The validation of the perfect fluidity requires the dimensionless ratio of shear viscosity η to entropy density s to be small.

Heavy quarks (charm and bottom) are important probes of the dense matter formed at RHIC. Because of their large masses, their dominant production mechanism is restricted to parton-parton collisions in the initial stage of the reaction. They can interact with the medium differently than light quarks and gluons due to their heavy mass. It was predicted that the energy loss of heavy quarks would be smaller than that of light quarks and

gluons due to suppression of small angle gluon radiation, called the “dead cone effect” [15, 16].

Recently, heavy quark measurements along with models for heavy quark interaction have opened new possibilities to investigate other interaction mechanisms such as collisional energy-loss and in-medium fragmentation. In some models, the heavy quark diffusion coefficient D^{HQ} controls the extent to which the initial power-law p_T spectrum approaches the thermal spectrum and the extent to which the heavy quark will follow the underlying flow of the medium. Simultaneous measurement of heavy-quark $R_{AuAu}(p_T^e)$ and $v_2(p_T^e)$ can provide an estimate of D^{HQ} .

Heavy quark measurements in $p+p$ collisions serve as a testing ground of QCD. Because of their large mass, it is expected that next-to-leading order perturbative QCD (NLO pQCD) can describe the production cross section of charm and bottom at high energy, particularly at high p_T . At the Tevatron with $\sqrt{s} = 1.9$ TeV, bottom production is well described by NLO pQCD [17]. Charm production cross sections at high p_T are found to be higher than the theory by $\approx 50\%$, but are compatible within the theoretical uncertainties [18].

There are several ways to measure heavy quark production. The most direct method is to reconstruct D or B mesons from their decay products, such as $D \rightarrow K\pi$ or $B \rightarrow J/\psi K$. PHENIX is currently not capable of measuring the decay vertex of the heavy meson, which makes this method very difficult. The method which is employed by this analysis is to measure single leptons from heavy flavor decay. Both the charm and bottom quarks have relatively large branching ratios ($\sim 10\%$) to single electrons or single muons. Production yields and momentum distributions of the parent charm or bottom hadrons can be inferred from the invariant spectrum of single leptons from the decay. This method has an advantage in heavy-ion collisions at RHIC where the first method suffers from a very large combinatorial background due to the high multiplicity of the event.

Single electrons in hadronic collisions were first observed in the early 1970’s in $\sqrt{s} = 52.7$ GeV $p+p$ collisions at the CERN ISR [19] before the discovery of charm.

*Deceased

†PHENIX Spokesperson: jacak@skipper.physics.sunysb.edu

Subsequently, several experiments reported single electron production at the ISR. In $p\bar{p}$ collisions at $\sqrt{s}=630$ GeV, UA1 [20] measured bottom production via single muons and UA2 [21] reported the charm cross section from single electron measurements. At the Tevatron collider, the CDF [22] and D0 [23] experiments measured bottom production via single muons or single electrons.

At RHIC, PHENIX first measured charm production in Au+Au collisions at $\sqrt{s_{NN}} = 130$ GeV via measurement of single electrons [24]. Subsequently, PHENIX reported results of single electron measurements in $p+p$ [25] and Au+Au collisions [26–28] at midrapidity from the 2002 data set. In Au+Au collisions, the total yield of heavy-flavor decay electrons was found to scale with the number of binary nucleon-nucleon collisions [26] as expected for a point-like process. As already mentioned, the energy loss of heavy quarks was expected to be reduced due to the dead-cone effect. Consequently, it was expected that high p_T suppression and v_2 of heavy-flavor electrons would be much weaker than those of light mesons. In contrast, a strong suppression of heavy-flavor electrons for $2 < p_T < 5$ GeV/c [28] and a non-zero electron v_2 for $p_T < 2$ GeV/c [27] were discovered. The STAR experiment has also measured the yield of electrons from heavy flavor decays at RHIC [29].

This article presents measurements of single electrons $(N_{e^+} + N_{e^-})/2$ from semileptonic decays of heavy quarks (charm and bottom) at midrapidity ($|\eta| < 0.35$) in $p+p$ and Au+Au collisions at $\sqrt{s_{NN}}=200$ GeV. The data were collected in 2004 (Au+Au), and 2005 ($p+p$). We extend the previous PHENIX analyses of electron measurements in $p+p$ and Au+Au collisions at $\sqrt{s_{NN}} = 200$ GeV to a broader p_T^e range: $0.3 < p_T^e < 9.0$ GeV/c and with a much higher precision. Part of the results have been published in [30, 31].

This article is organized as follows: Section II presents an overview of the PHENIX detector system related to the analysis. Section III presents the details of the data analysis. Section IV shows the p_T^e distribution of the invariant spectrum in the 2005 $p+p$ and invariant yields and elliptic flow in 2004 Au+Au collisions. The results are compared with theoretical predictions and discussed in Sec. V. Finally, Sec. VI gives a summary and conclusions of the analysis.

II. PHENIX DETECTOR

A detailed description of the complete PHENIX detector system can be found elsewhere [32–37]. Here we describe the parts of the detector system that are used in this analysis, namely, two global detectors and two central arm spectrometers. The global detectors are the beam-beam counter (BBC) and the zero-degree calorimeter (ZDC). Each of the central arms covers a pseudorapidity of $|\eta| < 0.35$ and an azimuthal angle of $\pi/2$. They contain the drift chamber (DC) and the multiwire proportional pad chamber (PC) for charged particle track-

ing, the ring-imaging Čerenkov detector (RICH) for electron identification, and the electromagnetic calorimeter (EMCal) for energy measurement. Figure 1 shows the beam view of the PHENIX detector.

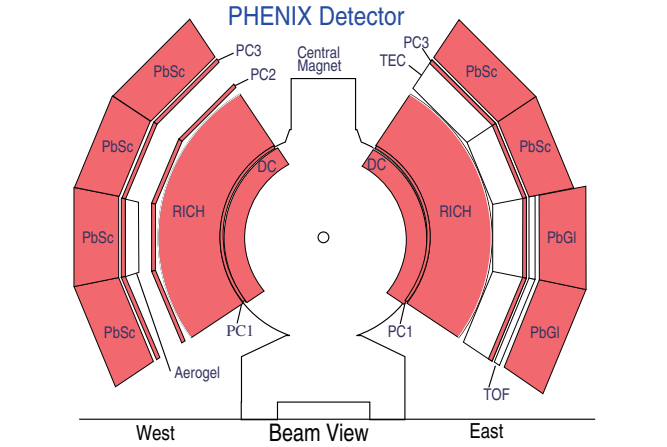


FIG. 1: (Color online) Beam view (at $z = 0$) of the PHENIX central arm detector in 2004 (Au+Au) and 2005 ($p+p$). The detectors used in the present analysis are the drift chamber (DC) and the multiwire proportional pad chambers (PC1, PC2, PC3) for charged particle tracking, the ring-imaging Čerenkov detector (RICH) for electron identification, and the electromagnetic calorimeters, which are Lead Glass (PbGl) and Lead Scintillator (PbSc), for energy measurement.

A. Global detectors

The BBC and the ZDC measure the collision time and the collision vertex position z_{vtx} along the beam. In Au+Au collisions, they are used to determine the centrality of the collision [37]. They also provide the first level, minimum bias (MB) trigger information for beam-beam collisions.

Two sets of BBCs are placed at ± 1.44 m from the nominal interaction point along the beam line (one on the north side and one on the south). Each BBC consists of 64 Čerenkov counter modules, arranged radially around the beam pipe. Each module is made of a 3 cm long quartz radiator and a photomultiplier tube (PMT). The PMTs can operate in a high magnetic field (~ 0.3 T) that lies mostly parallel to the beam axis. The BBC is used to estimate the number of charged particles in the pseudorapidity region $3.0 < |\eta| < 3.9$. The vertex position resolution of the BBC is ~ 0.6 cm for Au+Au collisions and a few cm in $p+p$ collisions.

The ZDC measures the total energy carried by the forward neutrons produced along the beam direction. These neutrons are produced either by Coulomb dissociation of the beam particles or by evaporation from beam spectators. The ZDCs are placed at ± 18 m from the interaction point along the beam line. The angular acceptance of each ZDC is $|\theta| < 2$ mrad ($|\eta| > 6$). Each ZDC consists

of three modules of two-interaction-length deep tungsten-quartz Čerenkov sampling calorimeters. The energy resolution of the ZDC is $\delta E/E \sim 218/\sqrt{E}$ (GeV) % [38].

B. Central magnet

The transverse momentum of each charged particle is determined by its bending curvature in the magnetic field provided by the PHENIX central magnet (CM) system [33]. The CM is energized by two pairs of concentric coils and provides an axial magnetic field parallel to the beam pipe. The coils can be run with the fields for the two coil sets adding (the “++” and “--” configurations) or canceling (“+-” configuration). During the Au+Au measurement in 2004 and the $p + p$ measurement in 2005, the CM was operated in the “++” and “--” configurations. In the “+-” and “--” configurations, the field component parallel to the beam axis has an approximately Gaussian dependence on the radial distance from the beam axis, dropping from 0.9 T at the center to 0.096 T (0.048 T) at the inner (outer) radius of DCs. The total field integral is $\int B \cdot dl = 1.15$ T·m.

C. Tracking detectors

The DC and PC [34] in the central arms measure charged particle trajectories in the azimuthal direction to determine the transverse momentum (p_T) of each particle. By combining the polar angle information from the innermost PC (PC1) with the p_T , the total momentum (p) is determined.

The DC is positioned between 2.02 and 2.46 m in radial distance from the z axis for both the West and East arms. Each DC occupies a pseudorapidity of $|\eta| < 0.35$ and $\pi/2$ in azimuth. Each DC volume consists of 20 sectors, each of which covers 4.5 degrees in azimuth. Each sector has six types of wire modules stacked radially, named X1, U1, V1, X2, U2 and V2. Each module is further divided into 4 drift cells in the ϕ direction. A plane of sense wires is at the center of a drift cell, with 2 to 2.5 cm drift space. The X wires run parallel to the beam axis and measure the particle trajectory in the r - ϕ plane. The U and V wires have a stereo angle of about 6.0 degrees relative to the X wires in order to measure the z -coordinate of the track. The single X wire resolution is ~ 150 μm . The intrinsic tracking efficiency of the X modules is greater than 99 %. Helium bags were placed between the beam pipe and the DCs to reduce the photon conversions and multiple scattering.

The PC determine the spacepoints along the straight line particle trajectories outside the magnetic field. They are multiwire proportional chambers that form three separate layers of the central tracking system. The first PC layer (PC1) is located between the DC and RICH at 2.47-2.52 m in radial distance from the interaction point, while the third layer (PC3) is located in front of EMCal occu-

pying 4.91-4.98 m from the interaction point. The second layer (PC2) is placed behind RICH occupying 4.15-4.21 m in radial distance in the West arm only. Position information from the PC1 and the DC, along with the vertex position measured by the BBC, are used in the global track reconstruction to determine the polar angle of each charged track.

D. Ring-imaging Čerenkov detector (RICH)

The RICH is a threshold-type gas Čerenkov counter and the primary detector used to identify electrons in PHENIX [35, 39]. It is located in the radial region of 2.5-4.1 m just outside PC1. The RICH in each central arm covers a pseudorapidity range of $|\eta| < 0.35$ and $\pi/2$ in azimuthal angle. Each volume contains mirror panels (0.53 % of a radiation length thick), forming two intersecting spherical surfaces, with a total reflecting area of 20 m². The spherical mirrors focus Čerenkov light onto two arrays of $80(\phi) \times 16(z) = 1280$ PMTs, each located on either side of the RICH entrance window as shown in Fig. 2. Each PMT has a magnetic shield that allows it to operate in a magnetic field up to 100 Gauss. CO₂ gas at atmospheric pressure ($n = 1.000410$) was used as the Čerenkov radiator. The RICH has a Čerenkov threshold of $\gamma = 35$, which corresponds to $p > 20$ MeV/ c for an electron and $p > 4.9$ GeV/ c for a pion.

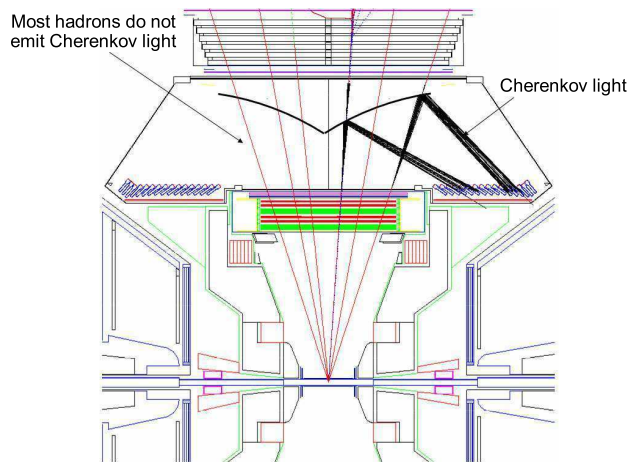


FIG. 2: (Color online) Top view (at $y = 0$) of the ring-imaging Čerenkov detector (RICH) in the PHENIX East arm.

The average number of hit PMTs per electron track is about 5, and the average number of photo-electrons detected is about 10. The e/π separation is $\sim 10^4$ in $p + p$.

E. Electromagnetic calorimeter (EMCal)

The EMCal [36] consists of two arms, each covering a pseudorapidity region of $|\eta| < 0.35$ and $\pi/2$ in azimuthal

angle. Each of the two arms consists of four rectangular sectors. Two adjacent sectors of the East arm are based on lead-glass (PbGl) calorimetry, whereas the remaining sectors are based on lead-scintillator (PbSc) calorimetry. The radial distance from the z axis is 5.10 m for PbSc and 5.50 m for PbGl.

The PbSc is a Shashlik-type sampling calorimeter made of alternating tiles of lead and scintillator. It consists of $10.5 \times 10.5 \times 37$ cm³ ($18.2 X_0$) rectangular modules, each of which is constructed from alternating layers of 1.5 mm thick lead and 4 mm polystyrene-based scintillator layers. The light from the scintillator is collected by optical fibers that run longitudinally through the module volume and are brought to four PMTs in the back end. This structure divides each module into four equal square cross section towers, from which the light is collected separately by the fibers. A PbSc sector is subdivided into 18 ($3(\phi) \times 6(z)$) super-modules made of 12×12 towers. Thus a PbSc sector consists of $36(\phi) \times 72(z) = 2592$ towers. The nominal energy resolution is $\delta E/E \sim 4.5\% \oplus 8.3/\sqrt{E}$ (GeV) %.

The PbGl consists of $4 \times 4 \times 40$ cm³ rectangular modules, each assembled from 4 lead-glass crystals. Light emitted by particles depositing energy in the crystals is collected by a PMT at the back of each module. Twenty four of them ($4(\phi) \times 6(z)$) are combined together to form a PbGl-module. Six PbGl-modules ($3(\phi) \times 2(z)$) comprise a PbGl-super-module and 32 of them ($4(\phi) \times 8(z)$) constitute a sector. This means a PbGl sector consists of $48(\phi) \times 96(z) = 4608$ PbGl counters. The PbGl has a nominal energy resolution of $\delta E/E \sim 4.3\% \oplus 7.7/\sqrt{E}$ (GeV) %.

The EMCal served as the electron trigger device in the 2005 $p+p$ data taking. The trigger (PH) is fired whenever there is any hit which produces an energy of more than 1.4 GeV in an EMCal trigger tile unit. The trigger tile consists of 4×4 non-overlapping towers. All trigger bits output from the tiles are summed in each super module online. Since there are 172 EMCal super-modules (108 PbSc + 64 PbGl), the PH trigger has 172 output channels. 95 % of them were live in the 2005 $p+p$ data. All the output bit information is summed and used for the event-trigger decision. The trigger efficiency is evaluated in section III G.

III. ANALYSIS

A. Data set and event selection (Au+Au)

The data for Au+Au collisions at $\sqrt{s_{NN}} = 200$ GeV were taken during the 2004 run of RHIC. The minimum bias (MB) trigger was defined as:

$$\text{MB} \equiv (\text{BBC} \geq 2) \&\& (|z| < 38 \text{ cm}). \quad (1)$$

Here, $\text{BBC} \geq 2$ means that at least two hits are required in both the North and South BBCs. The offline

trigger also requires at least one hit in one of the ZDCs. The vertex position along the beam line is determined online from the timing difference between the two BBCs. The MB trigger efficiency for inelastic Au+Au collisions is evaluated as $92.2^{+2.5}_{-3.0}\%$.

In the offline analysis, a tighter vertex cut ($|\text{bbc}z| < 20$ cm) is required to eliminate conversion electrons from forward materials. Here **bbc** z is the vertex position determined by BBC in the offline analysis. Any abnormal data due to unusual beam or detector conditions are removed. Table I summarizes the number of MB events used for the analysis of electron spectra. For the v_2 analysis, only those events with a good reaction plane calibration were used. The number of MB events used for the v_2 analysis was 7.1×10^8 events.

The MB events are divided into five centrality classes of 0–10%, 10–20%, 20–40%, 40–60%, and 60–92%. See section III C for the centrality determination.

There are two groups of runs: normal runs and converter runs. In the converter runs, an additional photon converter was inserted around the beam pipe. See section III J for the converter runs and their use for the analysis.

TABLE I: Number of events for each centrality class for runs with and without additional converter material installed.

Centrality class	Normal runs	Converter runs
0–92%	7.48×10^8	5.79×10^7
0–10%	8.06×10^7	6.31×10^6
10–20%	8.07×10^7	6.29×10^6
20–40%	1.61×10^8	1.25×10^7
40–60%	1.61×10^8	1.24×10^7
60–92%	2.65×10^8	2.04×10^7

B. Data set and event selection ($p+p$)

The data for $p+p$ collisions at $\sqrt{s} = 200$ GeV were collected during the polarized $p+p$ collisions in 2005. The proton beams had approximately 50% longitudinal polarization with alternating spin orientations in successive bunches. The polarization of the protons has negligible effect on the cross section.

Two data sets are used for the electron analysis: (1) the minimum bias (MB) data set and (2) a “photon” (PH) trigger data set. The MB trigger for $p+p$ required at least one hit in both the North and South BBC detectors in coincidence with the beam bunch crossing and the event vertex position within $|\text{bbc}z| < 30$ cm from the nominal collision point along the beam axis. The PH trigger required a minimum energy deposit of 1.4 GeV in an overlapping tile of 4×4 EMCal towers in coincidence with the MB trigger. The PH trigger had nearly 100% trigger efficiency for electrons with p_T above 2 GeV/ c in the active trigger tiles.

The MB trigger cross section is $\sigma_{\text{BBC}} = 23.0 \pm 2.2$ mb. Since only $\simeq 50\%$ of inelastic $p + p$ collisions satisfy the MB trigger condition, only a fraction of the inclusive electron production events were triggered by the PH trigger. This fraction is assumed to be momentum and process independent, and is determined to be $\epsilon_{\text{bias}} = 0.79 \pm 0.02$ [40] from the yield ratio of high p_T π^0 's with and without the BBC trigger. The value of ϵ_{bias} is slightly higher than that of 2002 (0.75) [25], due to a lower BBC threshold.

After the selection of good runs and the vertex cut, an integrated luminosity (\mathcal{L}) of 45 nb^{-1} in the MB data set and 1.57 pb^{-1} in the PH data set are used for the analysis. During a part of the 2005 $p + p$ run, the same photon converter that was used in the 2004 Au+Au run was inserted around the beam pipe. The integrated luminosity in the converter run period is approximately 7% of the total luminosity.

C. Centrality (Au+Au)

The centrality of each Au+Au collision is determined by the measurements of BBC charge and ZDC energy. Figure 3 shows the correlation between BBC total charge and ZDC total energy for real data, each of which is normalized by the maximum value. The amount of BBC charge is proportional to the particle multiplicity and is correlated to the overlapping area of two colliding nuclei. In contrast, the total ZDC energy is smaller in peripheral collisions than it is in central collisions. In the most peripheral collisions, a large fraction of the nuclei become spectators. The number of free neutrons reaching the ZDC becomes small, due to the formation of deuterons or heavier charged nuclei from the spectator neutrons and protons, which are swept by the magnets. The centrality determination from the BBC and ZDC energy is schematically shown in Fig. 3. Each centrality class contains approximately the same number of events. The most peripheral class is normalized to be 92%.

The relation between centrality, the number of binary collisions (N_{coll}), and the number of participants (N_{part}) is obtained from a Glauber Monte Carlo simulation [41]. The systematic uncertainties in N_{coll} and N_{part} are calculated from the uncertainty in the Glauber parameters, the centrality determination, and BBC and ZDC responses. Table II summarizes the average N_{coll} , N_{part} , the associated nuclear overlap function (T_{AuAu}) and their systematic errors for each centrality class.

D. Track Reconstruction

Charged particles are reconstructed by the DC and PCs. Figure 4 shows a trajectory up to PC3 and associated kinematic parameters. Assuming that the track originates on the beam axis, the intersections of the trajectory with each detector plane are uniquely determined by four initial kinematic parameters: z_{vtx} , θ , ϕ_v , and the

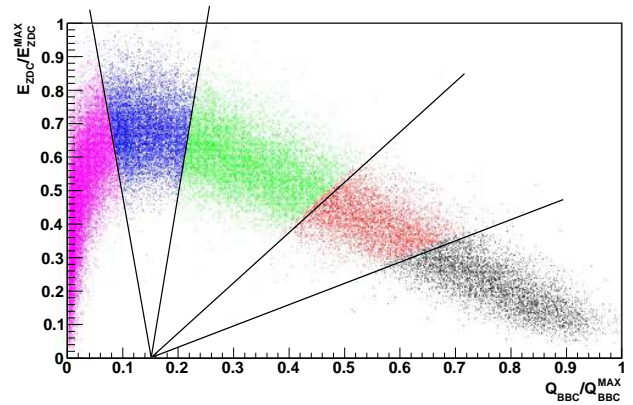


FIG. 3: (Color online) The correlation between fractional BBC charge Q/Q_{max} and fractional of ZDC energy E/E_{max} . The sections from right to left correspond to centrality classes 0–10 %, 10–20 %, 20–40 %, 40–60 %, and 60–92 %.

TABLE II: N_{part} , N_{coll} and T_{AuAu} [41] by Glauber calculation for Au+Au collisions at $\sqrt{s_{\text{NN}}} = 200$ GeV.

Centrality class	$\langle N_{\text{part}} \rangle$ (syst)	$\langle N_{\text{coll}} \rangle$ (syst)	$\langle T_{\text{AuAu}} \rangle$ (MB^{-1}) (syst)
0–92%	109.1 (4.1)	257.8 (25.4)	6.14 (0.45)
0–10%	325.2 (3.3)	955.4 (93.6)	22.75 (1.56)
10–20%	234.6 (4.7)	602.6 (59.3)	14.35 (1.00)
20–40%	140.4 (4.9)	296.8 (31.1)	7.07 (0.58)
40–60%	59.95 (3.6)	90.70 (11.8)	2.15 (0.26)
60–92%	14.50 (2.5)	14.50 (4.00)	0.35 (0.10)

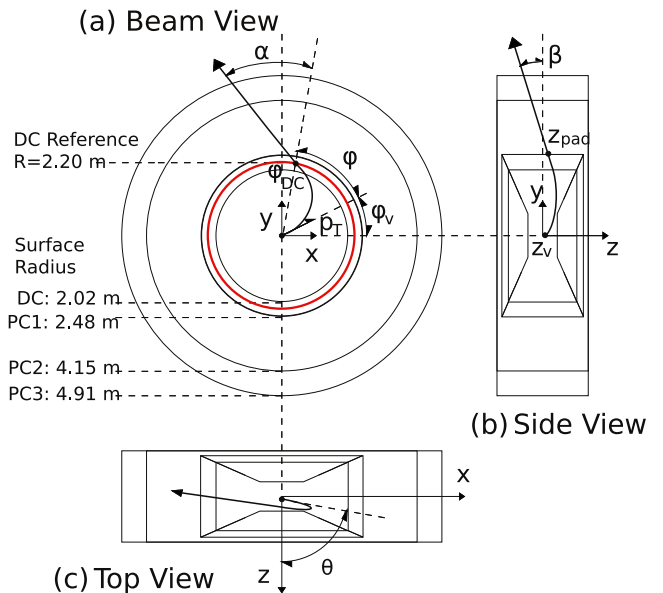


FIG. 4: (Color online) A charged particle trajectory and the kinematic parameters are shown in (a) beam view, (b) side view, and (c) top view of PHENIX central region.

transverse momentum p_T . Here, z_{vtx} is the interaction vertex along the z -axis, θ is the angle between the initial direction of the particle track and z -axis, and ϕ_v is the initial azimuthal angle of the trajectory. These initial parameters are reconstructed from measured variables: α , β , z_{pad} , and ϕ_{DC} . α is the angle between the projection of the trajectory in the $x-y$ plane and the radial direction, at the intersection point of the trajectory with the circle of DC reference radius ($R_{\text{DC}} = 2.2 \text{ m}$). z_{pad} is the intersection point of the trajectory with PC1 surface radius ($R_{\text{PC1}} = 2.48 \text{ m}$). β is obtained by considering the plane which includes the z -axis and z_{pad} . It is defined as the angle between the projection of the trajectory to the plane and the line connecting the vertex to the position of the pad chamber hit. ϕ_{DC} is the azimuthal angle of intersection point of the trajectory with the circle of radius with R_{DC} .

The tracking process starts by collecting hits in DC X1 and X2 wires. The hits are projected to the $x-y$ plane at $z = 0$. Then, a Hough transform is applied to find the sets of hit points based on the assumption of the track having a straight line trajectory inside the DC volume [42, 43]. The technique is performed using all possible X1 and X2 hit combinations taking α and ϕ_{DC} as the parameters in Hough space. After this process, the direction of the found track line is specified by α and ϕ_{DC} . The hits in the U and V wires and PC1 hits are associated with the track in order to obtain z_{pad} and β . After the pattern recognition and track reconstruction, the initial momentum vector of the track at the collision vertex is calculated. A look-up-table technique is used for fast processing [44, 45]. After the initial kinematic parameters are obtained, each reconstructed track is associated with hit information from the outer detectors (PC2, PC3, RICH, and EMCal).

E. Electron Identification

Electron candidates are selected from reconstructed charged tracks based on information from the RICH and EMCal. For each of the reconstructed tracks, the following variables are calculated and used for electron identification (eID);

- **quality** – Tracks are required to have hits in both the X1 and X2 sections of the DC and be uniquely associated with hits in the U or V stereo wires. At least one matching PC1 hit is also required.
- **emcsdphi_e** – Displacement in ϕ of the electron hit position of the associated EMCal cluster from the projected position of the track in units of standard deviations. For example, **emcsdphi_e** < 2 means that the position of the associated EMCal cluster in ϕ is within 2σ of the projected track position. This variable was calibrated specifically for electrons.
- **emcsdz_e** – Same as **emcsdphi_e**, but for the z coordinate.

TABLE III: Electron ID cuts used in Au+Au analysis

eID cuts for Au+Au
$\sqrt{\text{emcsdphi}_e^2 + \text{emcsdz}_e^2} < 2.0$
$n0 \geq 2$
$n1 \geq 3$ if $p_T < 5.0 \text{ GeV}/c$
$n1 \geq 5$ if $p_T > 5.0 \text{ GeV}/c$
$\text{disp} < 5.0$
$\text{chi2}/\text{npe0} < 10.0$
$\text{prob} > 0.01$ if $p_T < 5.0 \text{ GeV}/c$
$\text{prob} > 0.2$ if $p_T > 5.0 \text{ GeV}/c$
$\text{dep} > -2.0$

- **prob** – The probability that the associated EMCal cluster is an electromagnetic shower. This variable is calculated from the χ^2 value between the actual tower energy distribution of the cluster and the expected distribution for an electromagnetic shower. For example, a cut, **prob** > 0.01 , has 99% efficiency for a photon or electron shower, while it rejects a large fraction of hadrons.
- **n0** – Number of hit RICH PMTs in an annulus region with inner radius of 3.4 cm and outer radius of 8.4 cm around the track projection on the RICH. The expected radius of a Čerenkov ring emitted by an electron is 5.9 cm.
- **n1** – The number of hit RICH PMTs within 11 cm around the projection point of the track.
- **chi2/npe0** – A χ^2 -like shape variable of the RICH ring associated with the track.
- **disp** – A variable representing the displacement of the RICH ring center from the projected track position. Units are cm.
- **dep** – A variable of energy momentum matching. This variable is calculated as **dep** $= (E/p - 1)/\sigma_{E/p}$, where E is the energy measured by EMCal; p is the momentum of the track; and $\sigma_{E/p}$ is the standard deviation of Gaussian-like E/p distribution. E/p is less than 1 for hadrons since hadrons do not deposit their full energy in the calorimeter. $\sigma_{E/p}$ depends on the momentum of the electron.

Tables III and IV summarize the eID cuts used for the Au+Au and $p+p$ analyses, respectively. For tracks with p_T below 4.8 GeV/c, the RICH is fired only by electrons. Thus the RICH is the primary means of electron detection in this p_T region. The E/p cuts remove remaining background. The main cause of electron misidentification below 5 GeV/c is that a charged hadron track is accidentally associated with hits in the RICH detector. Since the particle multiplicity in $p+p$ is very small, typically few tracks in each of the central arm spectrometers, the probability of such an accidental overlap

TABLE IV: Electron ID cuts used in $p + p$ analysis

eID cuts for $p + p$	
emcsdphi_e < 4	
emcsdz_e < 4	
n0 \geq 2	
n1 \geq 2	
prob > 0.01	
0.50 < E/p < 1.3(0.2 < p < 0.3 GeV/c)	
0.55 < E/p < 1.3(0.3 < p < 0.4 GeV/c)	
0.60 < E/p < 1.3(0.4 < p < 0.6 GeV/c)	
0.65 < E/p < 1.3(0.6 < p < 0.8 GeV/c)	
0.70 < E/p < 1.3(0.8 < p < 5.0 GeV/c)	

is much smaller. This permits us to use looser electron cuts in the $p + p$ analysis. Note that although hadrons could fire the RICH above 4.8 GeV/c, the number of photoelectrons is small for hadrons below 5 GeV/c, and such hadrons are easily distinguishable from electrons. Thus we tighten our cuts above 5 GeV/c without worrying about extra hadron contamination.

In $p + p$ collisions the hadron contamination after the eID cuts is very small. The contamination level is estimated by reversing the **prob** cuts to enhance the hadron background. The estimated hadron contamination is 3% at $p_T = 0.3$ GeV/c and less than 1% for $0.8 < p_T < 5$ GeV/c with eID efficiency of approximately 90%. In Au+Au, there still remains hadron background due to accidental overlap between a track and RICH hits. This background is estimated and subtracted as described below.

Figure 5 (a) and (b) show E/p distributions for two typical p_T ranges in Au+Au collisions. All cuts in table III are applied except for the **dep** cut since it is just a p_T -dependent cut in E/p . The square points are the estimated distributions of the remaining hadron background which are randomly associated with a ring in the RICH. This estimation is performed by swapping the north and south sides of the RICH in the same event in software, and reconstructing the track matching to RICH. That is, DC tracks from the south are matched with RICH hits in the north, and vice-versa. Since the north and the south sides of the RICH are identical and there was only ~ 1 percent of dead channels in the RICH PMTs, this method gives a proper statistical estimate of the random hadron background in the electron sample.

After subtraction of the random hadron associations (shown as squares in Fig. 5 (a) and (b)), an additional low E/p tail remains in the distribution at high p_T , as shown in Fig. 5 (b). This tail is due to electrons from kaon decay (K_{e3}) and photon conversions that occur far from the collision vertex. These background electrons are reconstructed with a momentum higher than the actual momentum of the electrons, and as such have a low E/p .

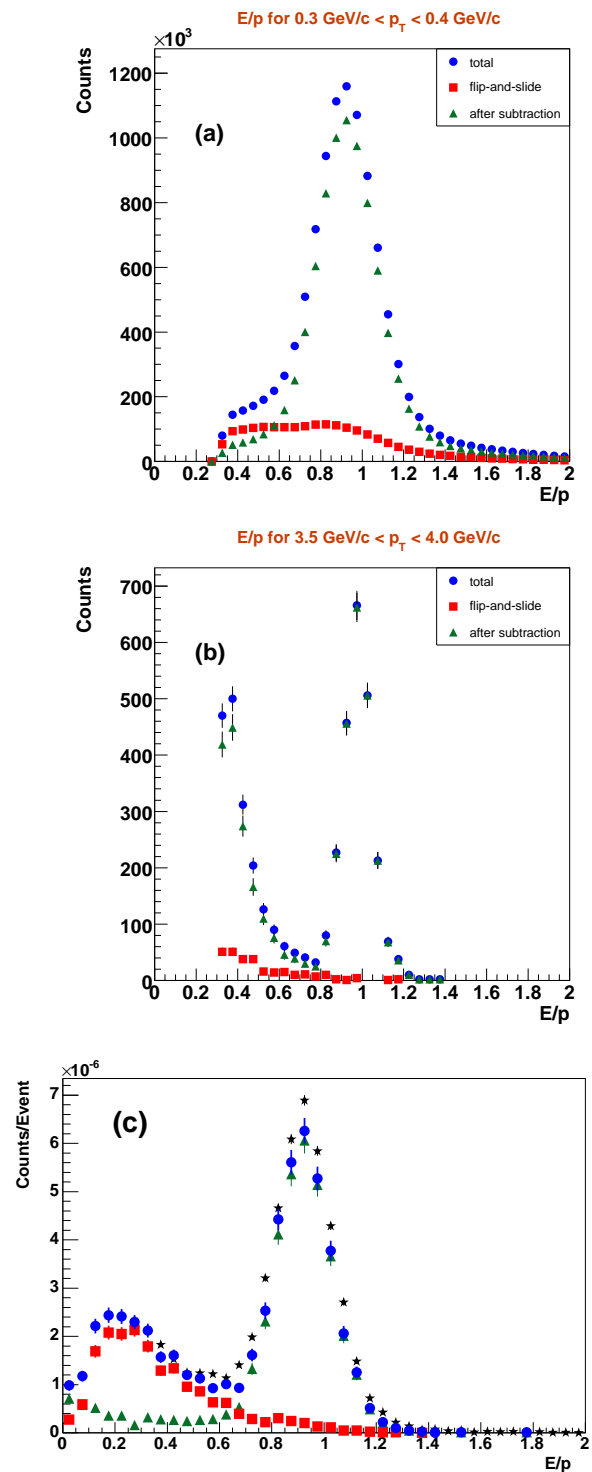


FIG. 5: (Color online) E/p distributions for various p_T ranges. (a) and (b) are for Au+Au collisions. (c) is for $p + p$ collisions, where the black stars are the data points and the solid circles show the GEANT [46] simulation. The triangles and squares show the contributions from simulation of π^0 and K_{e3} , respectively. See text for more details.

A full GEANT [46] simulation of the PHENIX detector was performed to determine the background from K_{e3} decays and from photon conversions. Figure 5(c) shows the E/p distribution in $p+p$ for $0.8 < p_T < 1.0$ GeV/c compared with the GEANT simulation. The black stars are the data points and the circles show the simulation. The triangles and squares show the contributions from simulation of π^0 and K_{e3} , respectively. The simulated π^0 and K_{e3} decays went through the same offline analysis chain as in the real data, and identical electron identification cuts were applied. In the $p+p$ data, the contamination of hadron mis-identification is negligible. In the π^0 simulation, electrons are mainly produced either by the Dalitz decay or by photon conversion in the beam pipe. These conversion electrons produce the peak around $E/p = 1$. Note that in Fig. 5(c) the data is above the simulation since the data also contain nonphotonic electrons. A small number of conversions in the helium bag contribute to the tail in the low E/p region. The main cause of the low E/p tail is K_{e3} decay, shown as squares. Since the simulation reproduces the low E/p tail of the data very well, we conclude that the K_{e3} background under the Gaussian peak, which will remain after the **dep** or E/p cuts, can be determined from the simulation.

There is no adjusted normalization in this simulation/data comparison. In the simulation, we assume $d\sigma/dy(pp \rightarrow \pi^0) = 46.0$ mb, $d\sigma/dy(pp \rightarrow K^L) = d\sigma/dy(pp \rightarrow K^\pm) = 4.0$ mb at midrapidity. The momentum distribution of π^0 and kaons are based on PHENIX measurements in $p+p$.

For p_T above 4.8 GeV/c, charged pions begin to radiate Cherenkov light in the RICH. Thus tighter electron selection cuts are applied to reject pion background. In both the Au+Au and $p+p$ analyses, tighter cuts of **n1** ≥ 5 and **prob** > 0.2 are added. In the $p+p$ analysis, the E/p cut is tightened to $0.8 < E/p < 1.3$. With these cuts, the electron measurement is extended to 9 GeV/c in p_T . The tighter cuts are applied to tracks above 5 GeV/c, as the Cherenkov radiation is very weak between 4.8 and 5 GeV/c, and the data were binned in multiples of 0.5 GeV/c.

The remaining hadron background with the tighter cuts is studied using the shape of the E/p distribution. Here we rely on the fact that the distribution of the **prob** and E/p variables are roughly independent of p_T for hadrons at high p_T , and that a cut on **prob** <0.01 eliminates the vast majority of electrons. First, we obtain a sample of hadrons in the p_T range of 1-4 GeV/c by imposing a veto on the RICH. The hadron sample is then divided into two samples, one with **prob** >0.01 and the other with **prob** <0.01 . The ratio of these two hadron samples is taken. The upper plots in Fig. 6 show the two hadron samples and their ratio. The E/p distributions for p_T above 5 GeV/c are then estimated from the data with cuts identical to those described above, except with the **prob** cut reversed to **prob** <0.01 . These E/p distributions are then divided by the ratio shown in the upper right plot of Fig. 6 to obtain an estimate of

the E/p distributions of hadrons passing the **prob** >0.01 cut.

The lower plots of Fig. 6 show the estimate for the hadronic background along with the total E/p distribution. This procedure actually gives an overestimation of the background, as some electrons do pass the **prob** <0.01 cut. This can be seen in the lower left plot as a peak in the hadronic sample. From these plots, we determine that any hadronic background below 8 GeV/c is negligible. Between 8-9 GeV/c in p_T , we estimate a background of 20%, with an uncertainty of 10%. The eID efficiency of the tighter cuts is p_T independent. In $p+p$, it is determined to be 57% of that for $p_T < 5$ GeV/c by applying the same tighter cuts for $p_T < 5$ GeV/c.

F. Acceptance correction

The acceptance correction in this analysis covers the following three components: the geometrical acceptance correction (ϵ^{geo}), the eID efficiency (ϵ^{eID}) and the reconstruction efficiency (ϵ^{reco}). ϵ^{geo} accounts for the fraction of electrons that do not hit any detectors due to the finite solid angle covered by the detectors. ϵ^{eID} is the correction factor for signal loss by eID cuts. ϵ^{reco} takes into account that the measured electron spectrum in the detector is different from the real spectrum due to detector responses and the track reconstruction method. All the values are computed at once by the full detector simulation for single e^\pm events. Single e^+ and e^- events are generated uniformly in phase space ($0 < p_T^e < 15$ GeV/c, $|y| < 0.5$, and $0 < \phi < 2\pi$). They are processed by the full GEANT simulation program of the PHENIX detector[46]. The output simulation data files are processed by the event reconstruction chain of PHENIX. The acceptance correction factor ($\epsilon_{\Delta y}^{\text{acc}}$) is calculated as follows:

$$\epsilon_{\Delta y}^{\text{acc}} \equiv \epsilon^{\text{geo}} \cdot \epsilon^{\text{reco}} \cdot \epsilon^{\text{eID}} = \frac{dN_e^{\text{out}}/dp_T^e}{dN_e^{\text{in}}/dp_T^e}, \quad (2)$$

The p_T^e distributions of input and output electron yields are dN_e^{in}/dp_T^e and dN_e^{out}/dp_T^e , respectively. The same eID cuts and fiducial cuts used in real data processing are applied to the output. Since the input electrons are generated flat in p_T^e , we must take into account that the smearing of the spectrum due to imperfect momentum reconstruction affects a steeply falling spectra differently than our simulated spectra. Each track reconstructed in the simulation is weighted by the p_T^e of the corresponding input electron.

Figure 7 shows three curves of $\epsilon_{\Delta y}^{\text{acc}}$ as a function of p_T for $(N_{e^+} + N_{e^-})/2$. The top, middle and bottom curves are calculated with each set of eID cuts applied for $0.3 < p_T < 5.0$, $5.0 < p_T < 7.0$, and $7.0 < p_T < 9.0$ GeV/c respectively.

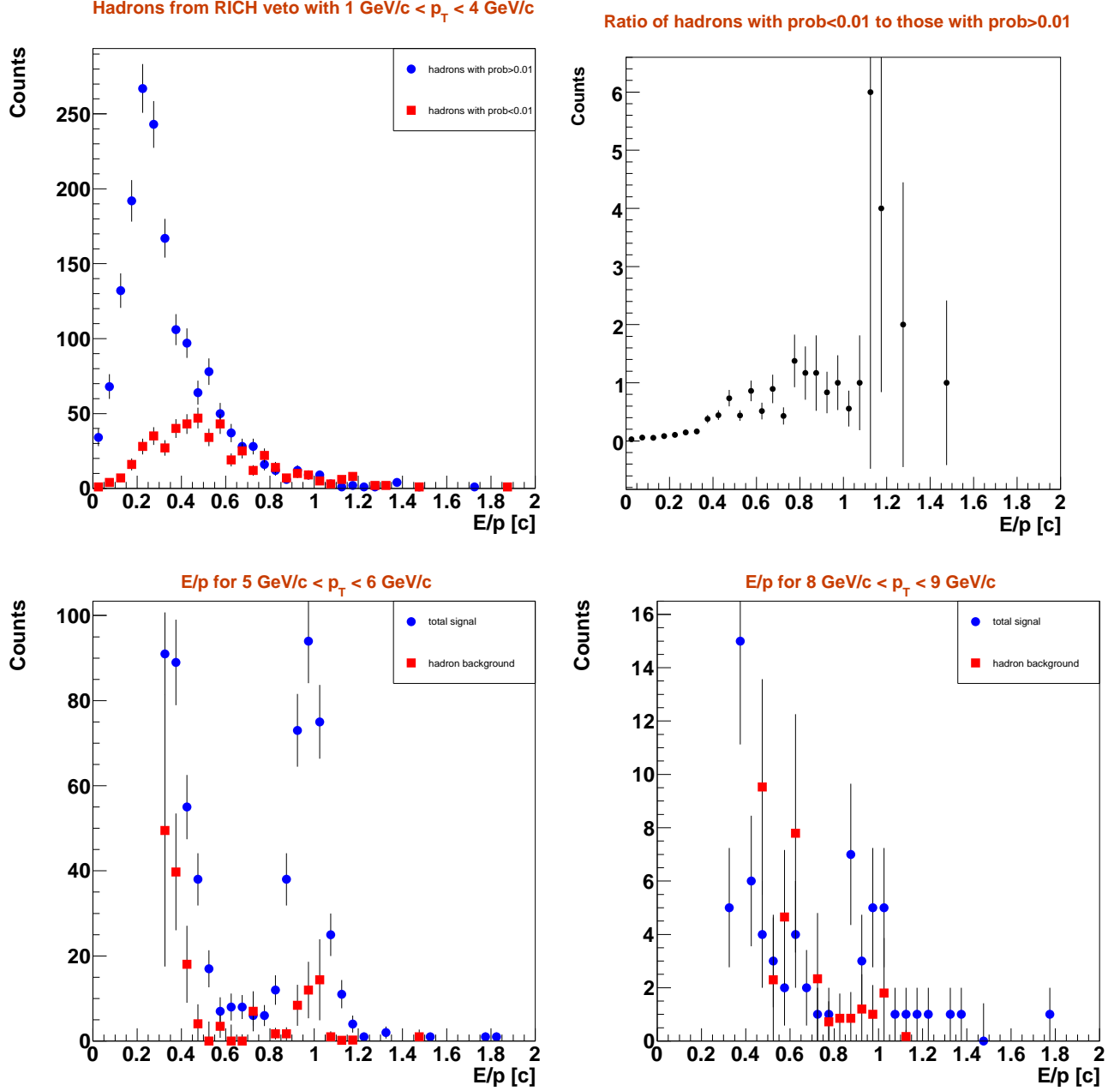


FIG. 6: (Color online) E/p distributions for (upper) hadron samples from a RICH veto cut which are used in the contamination study and (lower) the indicated high- p_T ranges, shown along with the estimation of the hadronic contamination.

G. Trigger efficiency ($p+p$)

The trigger efficiency of the PH trigger in $p+p$ collisions is determined from the MB data set as the fraction of electrons that satisfies the PH trigger. Since the trigger condition determined by the online level-1 trigger processor was recorded, we can apply the same PH trigger to the events recorded in the MB trigger in the offline analysis. We require that the PH trigger bits of the event are set, and that the trigger tile that fires the PH trigger is hit by the electron candidate track selected by the offline

analysis.

Figure 8 shows the trigger efficiency of the PH trigger thus determined. The effective trigger threshold is about 1.4 GeV, and the efficiency saturates above 2 GeV. The trigger efficiency at the plateau is $\approx 86\%$, consistent with the fraction of active trigger tiles. The curve is a Fermi-like function that is fitted to the data. The fitted function is used as the trigger efficiency in the analysis.

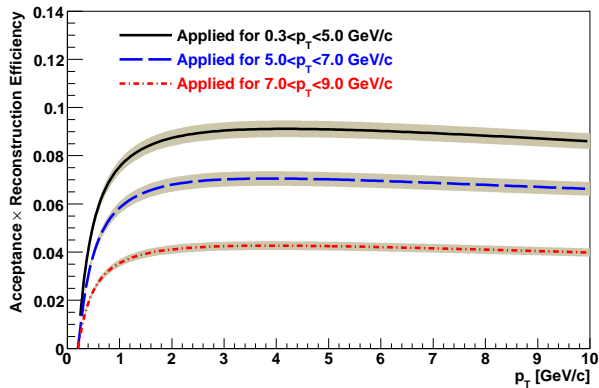


FIG. 7: (Color online) $\epsilon_{\Delta y}^{\text{acc}}$ for $(N_{e^+} + N_{e^-})/2$ as a function of p_T . The top, middle and bottom curves are calculated with eID cuts applied for $0.3 < p_T < 5.0$, $5.0 < p_T < 7.0$, and $7.0 < p_T < 9.0$ GeV/c respectively.

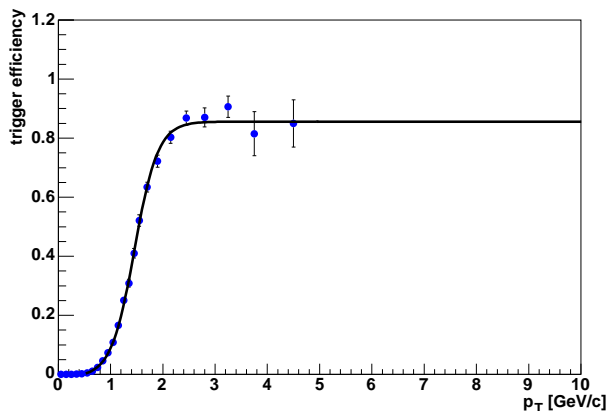


FIG. 8: (Color online) Efficiency of the PH trigger in $p + p$ determined from the minimum-bias data set.

H. Occupancy correction (Au+Au)

In addition to the efficiency for a single electron passing through the detector to pass the fiducial and eID cuts due to detector dead area and the efficiencies described above, there is also a finite efficiency loss for particle detection due to the presence of other particles nearby. To get a quantitative understanding of the multiplicity-dependent efficiency loss, we embed simulated single electrons and positrons into data files containing detector hits from real collisions. The same simulated particles are used in this method as those used to estimate the single particle efficiency loss. The simulated particles are embedded into events such that the z vertex of the simulated particle and the event are similar. The simulated e^\pm are run through the GEANT simulator of PHENIX, and the hits are added to the data files containing hits from a real Au+Au event. Next, these new files containing the embedded e^\pm are run through the entire reconstruction soft-

ware to produce track candidates containing the variables upon which we make identification cuts. We then define the embedding efficiency as

$$\epsilon_{\text{embed}} = \frac{\# \text{ reconstructed } e^\pm \text{ from embedded data}}{\# \text{ reconstructed } e^\pm \text{ from single track data}} \quad (3)$$

where a reconstructed particle from embedded data has most of its detector hits associated with hits from the simulated particle.

As a systematic cross-check on this method for determining the multiplicity-dependent efficiency loss, a data-driven method was employed. The general strategy of this data-driven method is to select a very pure sample of electron conversion pairs from the data with an invariant mass cut. We apply tight eID cuts to one of the tracks in a given pair to increase the chance that the pair really is an electron pair. Then, we measure the efficiency loss as a function of collision centrality of tighter cuts (cuts actually used in the analysis) relative to that of the loose cuts. We then still need simulation to determine the multiplicity-dependent loss due to the loose eID cuts, but simulation is more reliable when we use loose cuts. In order to get a pure sample of electrons, we isolate e^\pm pairs from photon-conversions in the beampipe and from π^0 Dalitz decays. We assume, reasonably, that the multiplicity-dependent efficiency loss for these electrons is the same as for all electrons.

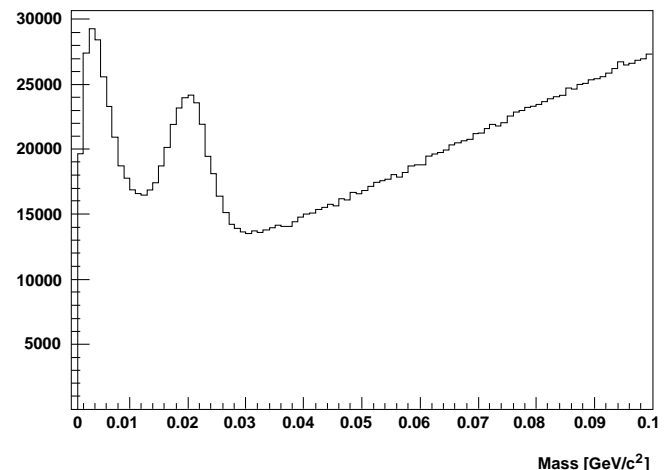


FIG. 9: Invariant mass distribution of e^\pm pairs from min-bias Au+Au data used for the multiplicity-dependent efficiency loss estimate.

Figure 9 shows the invariant mass distribution of e^\pm pairs from the data. The peak at ~ 20 MeV/ c^2 corresponds to the apparent mass of electrons from photon conversions in the beampipe. The peak at ~ 5 MeV/ c^2 corresponds to e^\pm from π^0 Dalitz decays. As mentioned above, we would like to have electrons identified by using both loose cuts and tight cuts. However, if loose cuts are applied to both the electron and the positron in the pair, then the sample will contain contamination from hadrons. In order to make sure that the pair is really

an e^\pm pair, we apply tight eID cuts to one of the particles in the pair. We restrict ourselves to pairs with one of the particles in the acceptance of the Time of Flight detector [35] so that we can use the TOF for electron identification.

The cuts used for the analysis for $p_T < 5$ GeV/ c are then applied to the other particle in the pair, and the relative efficiency loss is calculated. As described in the previous section, for $p_T > 5$ GeV/ c we obtain the efficiency by the relative electron yield between the samples with the cuts used for the two p_T ranges. This relative yield includes multiplicity-dependent effects, so we only explicitly calculate the multiplicity-dependent efficiency loss for the cuts used for $p_T < 5$ GeV/ c . Some of the relative efficiency loss using the method just described is due to the single particle efficiency. To obtain an estimate of the multiplicity-dependent component of this relative loss, we divide the relative loss by the loss for peripheral collisions (60%-93% centrality), since the multiplicity-dependent loss in peripheral collisions is very low. So we have defined the multiplicity-dependent efficiency loss from the data-driven method for centrality C as

$$\epsilon_{\text{mult}}^{\text{data},C} = \frac{\epsilon_{\text{eID}}^{\text{data},C}}{\epsilon_{\text{eID}}^{\text{data},60-93\%}} \quad (4)$$

with

$$\epsilon_{\text{eID}}^{\text{data},C} = \frac{\epsilon_{\text{tight cuts}}^C}{\epsilon_{\text{loose cuts}}^C}. \quad (5)$$

Ideally we would measure the above efficiency with no bias caused by making the initial loose cuts. We correct the multiplicity-dependent efficiency loss by using the efficiency from the embedding simulation for the loose cuts, $\epsilon_{\text{loose}}^{\text{embed},C}$ to obtain the more accurate estimate of the multiplicity-dependent loss from the otherwise data-driven method.

TABLE V: Multiplicity-dependent efficiency loss calculated by two methods. $\epsilon^{\text{embed},C}$ is the efficiency loss calculated from the embedding simulation. $\epsilon_{\text{loose}}^{\text{embed},C}$ is the same as above but with the loose cuts.

Centrality	$\epsilon^{\text{embed},C}$	$\frac{\epsilon_{\text{mult}}^{\text{data},C}}{\epsilon_{\text{loose}}^{\text{embed},C}}$
00-93%	0.852	0.882
0-10%	0.771	0.769
10-20%	0.835	0.856
20-40%	0.900	0.924
40-60%	0.952	0.977
60-93%	0.982	0.997

Table V displays the various embedding efficiencies described above. The difference between the left and right columns gives an idea of the systematic error involved in this estimation. The use of the sample of conversion and Dalitz e^\pm pairs will be discussed further in the section pertaining to systematic error analysis.

I. Electron background cocktail

The inclusive electron spectra consists primarily of three components: (1) “nonphotonic” electrons from heavy-flavor decays, (2) “photonic” background from Dalitz decays of light neutral mesons and photon conversions (mainly in the beam pipe), and (3) “nonphotonic” background from $K \rightarrow e\pi\nu$ (K_{e3}), and dielectron decays of vector mesons.

At high electron p_T , Drell-Yan processes also account for a small but non-negligible contribution to the electron spectrum. Also, heavy quarkonia decays contribute at high electron p_T , which, although arguably can be included in electrons from “heavy-flavor” decays, should be distinguished from open heavy flavor decays for the purpose of interpreting the measurement.

The photonic background is much larger than the nonphotonic background. The signal of electrons from heavy-flavor decays is small compared to the photonic background at low p_T ($S/B < 0.2$ for $p_T < 0.5$ GeV/ c) but rises with increasing p_T ($S/B > 1$ for $p_T > 2$ GeV/ c). In order to extract the heavy-flavor signal, the background has to be subtracted from the inclusive electron spectra. One technique to accomplish this task is the so-called “cocktail subtraction” method described in detail here.

A cocktail of electron spectra from background sources is calculated using a Monte Carlo event generator of hadron decays and then subtracted from the inclusive electron spectra. This technique requires that the phase space distributions of the relevant background sources be well known. The PHENIX measurements of the relevant electron sources are precise enough to constrain the background within a systematic uncertainty better than 15 % for all p_T . This uncertainty is of the same order as the signal to background ratio at the lowest p_T and, therefore, it is not sufficiently small to extract the heavy-flavor signal via the cocktail subtraction over the full p_T range. Hence, at low p_T , a complementary technique to subtract the background, the so-called “converter subtraction” method, is used to extend the heavy-flavor measurement to the lowest p_T with good precision. Consequently, the converter subtraction is the key to extracting the total heavy-flavor yield or cross section since most of the electrons from heavy-flavor decays have low p_T . However, towards high p_T , *e.g.* for $p_T > 2$ GeV/ c where the converter subtraction starts to suffer from a lack of statistical precision, it is beneficial to apply the cocktail subtraction since the signal to background ratio is large, statistics is irrelevant due to the Monte Carlo nature of the cocktail subtraction, and the cocktail input is known with small systematic uncertainties as discussed in the following.

The most important background source, except for the highest electron p_T where contributions from direct radiation become dominant (see below), comes from the neutral pion. The contribution of π^0 decays to the photonic background is twofold. First, the Dalitz decay of neutral

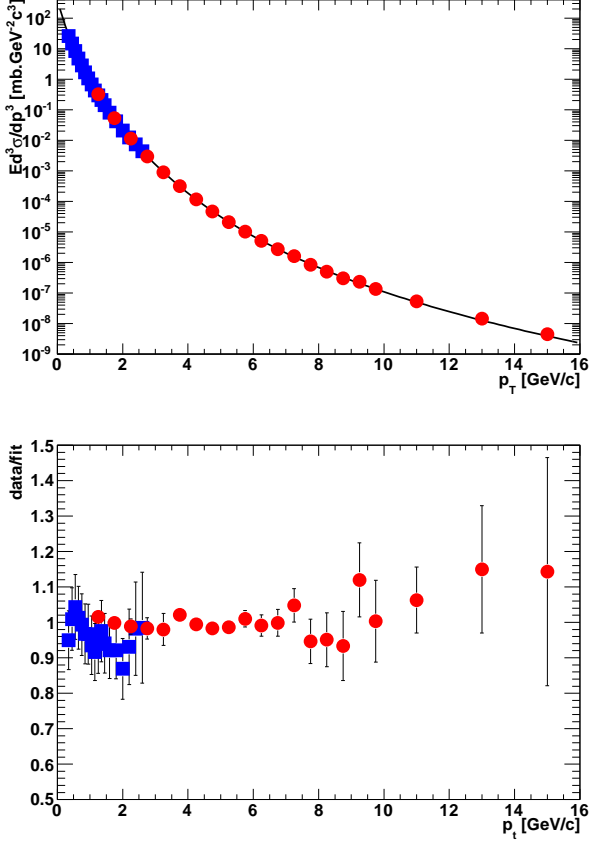


FIG. 10: (Color online) (upper) Invariant differential cross section of charged pions (squares at low p_T) and neutral pions (circles) for $p + p$ collisions, together with a fit according to Eq. 6. (lower) Ratio of the data to the fit.

pions ($\pi^0 \rightarrow e^+e^-\gamma$) is a primary source of electrons from the collision vertex. Second, the conversion of photons from the decay $\pi^0 \rightarrow \gamma\gamma$ in material in the PHENIX central arm aperture (mainly in the beam pipe) gives rise to a secondary source of electrons originating away from the original collision vertex. It is crucial to note that the contribution from photon conversions is smaller than the contribution from Dalitz decays. This is due to the carefully minimized material budget in the PHENIX central arms. Apart from the beam pipe, which is made out of Beryllium and contributes less than 0.3 % of a radiation length to the material budget, helium bags constitute the only material between the beam pipe and the tracking and electron identification detectors in PHENIX. As was verified in a full GEANT simulation of π^0 decays, the ratio of electrons from the conversion of photons from $\pi^0 \rightarrow \gamma\gamma$ decays to electrons from π^0 Dalitz decays is 0.403 with a systematic uncertainty of about 10 %. This ratio is independent of p_T in the range relevant here, *i.e.* for $p_T > 1 \text{ GeV}/c$. For heavier mesons this ratio is rescaled in the cocktail to properly account for the fact that the branching ratio for the Dalitz decay relative to

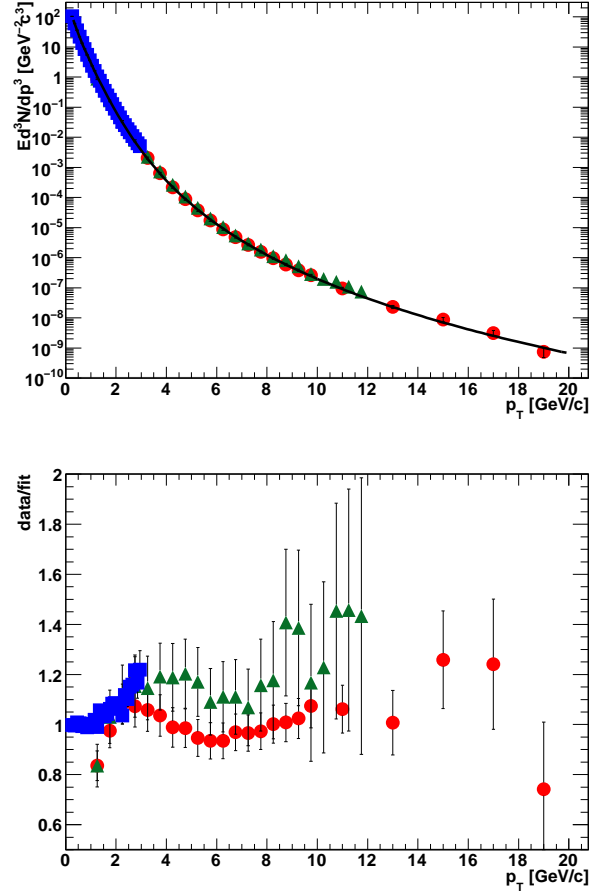


FIG. 11: (Color online) (upper) Invariant multiplicity of charged pions (squares at low p_T) and neutral pions for Au+Au collisions from 2002 (triangles) and 2004 (circles) together with a fit according to Eq. 6. (lower) Ratio of the data to the fit to the 2004 data.

the $\gamma\gamma$ decay grows slightly with increasing parent meson mass. Consequently, once the phase space distributions of π^0 and heavier mesons are available it is straight forward to determine both the Dalitz decay contribution to the background electron spectrum as well as the corresponding contribution from the conversion of photons from the same parent mesons.

The phase space distributions of π^0 are obtained via simultaneous fits to the charged and neutral pion spectra. This approach is only valid under the assumption that the invariant π^0 spectra and the averaged charged pion spectra $(\pi^+ + \pi^-)/2$ are the same. While this assumption in general is well justified, at low p_T , *i.e.* for $p_T < 1 \text{ GeV}/c$, the decay of η mesons into three π^0 creates a tiny charge asymmetry. However, according to a PYTHIA [47] calculation and consistent with data, this asymmetry is only about 2% and can be safely ignored in this context.

Figure 10 shows the comparison of the neutral and charge-averaged invariant differential cross sections of pi-

ons in $p+p$ collisions at $\sqrt{s} = 200$ GeV in comparison with a simultaneous fit to the data with a modified Hagedorn parametrization:

$$E \frac{d^3\sigma}{d^3p} = \frac{c}{(\exp(-ap_T - bp_T^2) + p_T/p_0)^n} \quad (6)$$

where a , b , c , p_0 , and n are fit parameters. Both an absolute comparison as well as the ratio of the data to the fit are shown to demonstrate the excellent quality of the parametrization.

For Au+Au collisions the π^0 invariant differential multiplicity distributions are obtained by equivalent fits to the measured π^0 [6, 48] and π^\pm [49] spectra independently for various centrality selections. Figure 11 shows the comparison of data and parametrization on absolute and relative scales for minimum bias Au+Au collisions as an example.

It is obvious that the neutral pion spectrum from 2004 is systematically different from the 2002 result. The difference between the parametrization and both sets of neutral pion spectra gives rise to an additional systematic uncertainty in the resulting electron cocktail. The difference between the parametrizations is assumed to be one standard deviation of error due to this systematic difference. This systematic uncertainty reaches its maximum value for electrons in the p_T range between 3 and 5 GeV/ c and is significantly less for lower as well as higher p_T .

Given that pion decays are the most important cocktail ingredient at low and intermediate p_T it is obvious that the cocktail systematic uncertainty is largely dominated by the uncertainty in the pion spectra as well. To evaluate this uncertainty the full cocktail calculation is repeated with the pion cross section moved up or down by one standard deviation in the systematic uncertainty, propagating the uncertainty in the pion spectra to the electron cocktail. With a systematic uncertainty of 10% almost independent of p_T , some of which originates from the difference between the Run 2 and Run 4 π^0 measurements, the pion input represents the largest contributor to the electron cocktail uncertainty, except for at the highest p_T where direct radiation becomes important.

Other light mesons contributing to the electron cocktail are the η , ρ , ω , η' , and ϕ mesons via their Dalitz decays and/or the conversion of photons from their decays. However, only the η meson is of any practical importance here.

For the cocktail calculation, the shape of the invariant p_T distributions and the relative normalizations to the π^0 are required as input parameters. The p_T spectra are derived from the pion spectrum by m_T scaling, *i.e.* the same modified Hagedorn parametrizations are used (Eq. 6), but with p_T replaced by $\sqrt{p_T^2 + m_{meson}^2 - m_{\pi^0}^2}$. The resulting η/π^0 ratios agree as a function of p_T well within experimental uncertainties for $p_T > 2$ GeV/ c with corresponding PHENIX data for $p+p$ and Au+Au collisions.

TABLE VI: Ratios of mesons to neutral pions in $p+p$ collisions

meson to pion ratios	
η/π^0	$= 0.48 \pm 0.03$ [50]
ρ/π^0	$= 1.00 \pm 0.30$ [51]
ω/π^0	$= 0.90 \pm 0.06$ [52]
η'/π^0	$= 0.25 \pm 0.075$ [51]
ϕ/π^0	$= 0.40 \pm 0.12$ [51]

Since the chosen approach of m_T scaling ensures that at high p_T the spectral shapes of all meson distributions are the same, the normalization of the meson spectra relative to the pion spectrum can be given by the ratios of mesons to pions at high p_T (5 GeV/ c is used here). The values used for $p+p$ collisions are shown in Table VI.

For Au+Au collisions the same central values are used, but the uncertainties of the ratio η/π^0 and ω/π^0 are, conservatively, increased to 0.10 and 0.27, respectively, since precision measurements are available for the production of these mesons in $p+p$ collisions but not in Au+Au collisions at all centralities.

The contribution from the K_{e3} decay and the semi-leptonic decay of K_S^0 can only be determined via a full GEANT simulation, taking into account the exact electron identification cuts. The electron cocktail includes parametrizations based on such GEANT simulations using the charged kaon spectra measured in $p+p$ and Au+Au collisions as input [49]. Systematic uncertainties are fully propagated from the kaon spectra to the spectra of reconstructed electrons from K_{e3} decays. In any case, the contribution from kaon decays is only relevant (*i.e.* larger than 10%) for electrons with $p_T < 1$ GeV/ c .

Contributions to the electron cocktail from direct radiation are twofold. First, real photons produced in initial hard scattering processes, *i.e.* so-called direct photons, convert in material in the PHENIX aperture exactly as photons from light neutral meson decays. Second, every source of real photons also presents a source of virtual photons. Consequently, direct real photon production is accompanied by direct virtual photon production, *i.e.* the emission of e^+e^- pairs. In the case of the neutral pion these two sources are the $\gamma\gamma$ decay of the π^0 and the corresponding Dalitz decays, which are also called internal conversions. The measured real direct photon spectra are parametrized and the conversion electron spectra of these are added to the electron cocktail.

Figure 12 shows comparisons of the measured direct photon spectrum with the cocktail parametrization for (upper) $p+p$ [53] and (lower) minimum bias Au+Au collisions [54]. In accordance with direct photon measurements in Au+Au collisions, the direct photon yield is assumed to scale with the number of binary collisions as a function of the centrality for p_T below 12 GeV/ c in the Au+Au electron cocktail. Note that although the parametrization used underestimates the central value of the direct photon measurement below 5 GeV/ c , the con-

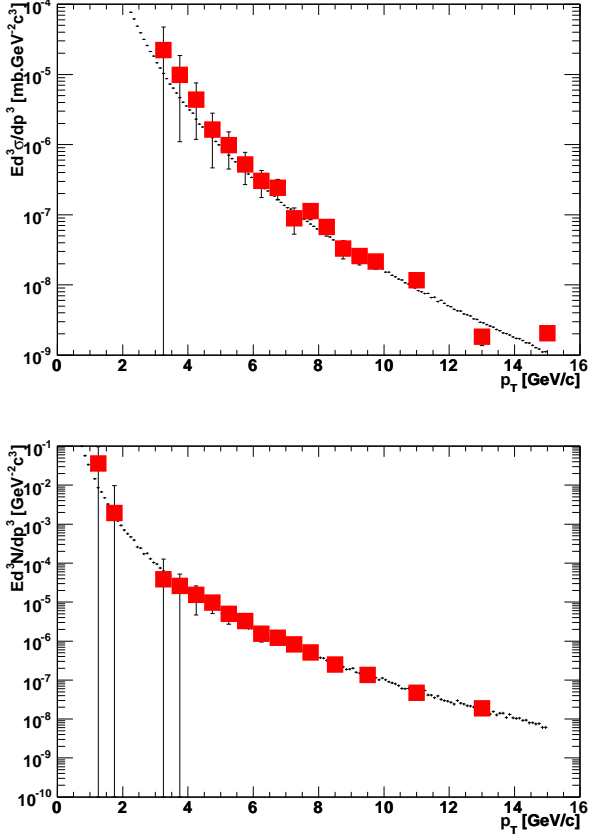


FIG. 12: (Color online) Measured direct photon spectrum (red squares) compared with the cocktail parametrization (histogram) for (upper) $p+p$ and (lower) Au+Au collisions.

tribution from direct photons in this p_T range is small enough that effects of this slight underestimation can be neglected.

The ratio of virtual direct photons to real direct photons depends on p_T because the phase space for dielectron emission increases with increasing p_T [55]. The very same effect is seen in the Dalitz decays of light neutral mesons. For instance, the Dalitz decay branching ratio relative to the two photon decay branching ratio is larger for the η meson than for the π^0 . Consequently, the ratio of virtual and real direct photon emission increases with p_T .

Figure 13 shows the resulting electron cocktails for $p+p$ and Au+Au collisions at 200 GeV. Systematic errors are estimated for all cocktail ingredients, propagated to the corresponding electron spectra, and then added in quadrature to determine the total cocktail systematic error. The following systematic errors are assigned to the various inputs:

- pion spectra: obtained via full cocktail calculations using pion spectra moved up (down) by the systematic uncertainty of the pion spectra as input (al-

most no p_T dependence). This is the dominant systematic uncertainty, except for the case of high p_T electrons (above 5 GeV/ c) in central Au+Au collisions, where direct radiation dominates the electron background and, at the same time, dominates the systematic uncertainty in the electron cocktail.

- meson to pion ratios: the systematic uncertainties are listed in Table VI. Since the contributions from all other mesons are much smaller than the contribution from η decay only the η is of any practical relevance. This contribution is small compared to the uncertainty in the pion spectra and it depends only slightly on p_T .
- conversion material in the aperture: the contribution from photon conversions obviously depends on the material present in the aperture. A careful analysis of fully reconstructed dielectrons from photon conversions suggests that this uncertainty is not larger than 10 %. It is crucial to note that the contribution from photon conversion to the background electron spectra is less than half of the contribution from direct Dalitz decays as a consequence of the careful minimization of the material budget in the PHENIX central arm aperture. For a reliable measurement of nonphotonic electrons this is an essential prerequisite.
- K_{e3} decay: this contribution is estimated via a full GEANT simulation. Given the limited statistics of this calculation a 50 % systematic error is assigned.
- direct radiation: this contribution is directly propagated from the systematic error quoted for the direct photon measurement. It is relevant only at high p_T in central Au+Au collisions.

In previous analyses, the single electron background cocktail has not included contributions originating from quarkonia decay (J/ψ and Υ) or Drell-Yan processes. Each of these processes has a small total cross section relative to the electron cocktail background. However, with increasing p_T these processes begin to contribute meaningfully and are included in the cocktail.

PHENIX has measured the J/ψ p_T spectrum from 0 to 9 GeV/ c in $p+p$ collisions [56]. To determine the appropriate input to the Monte Carlo event generator used to calculate the components of the electron cocktail, two functional fits to the J/ψ data are performed. The first uses the so-called Kaplan function $p_0 \left(1 + (p_T/p_1)^2\right)^{-n}$, and the second assumes the m_T scaling function used in [57]. Since both functions may provide valid representations of the true J/ψ spectral shape, the average of these two functional fits to the data determines the central values used in the cocktail. The upper (lower) systematic uncertainties of the spectral shape are determined by normalizing each of the functional forms up (down) by 10% and using the largest (smallest) result for the systematic

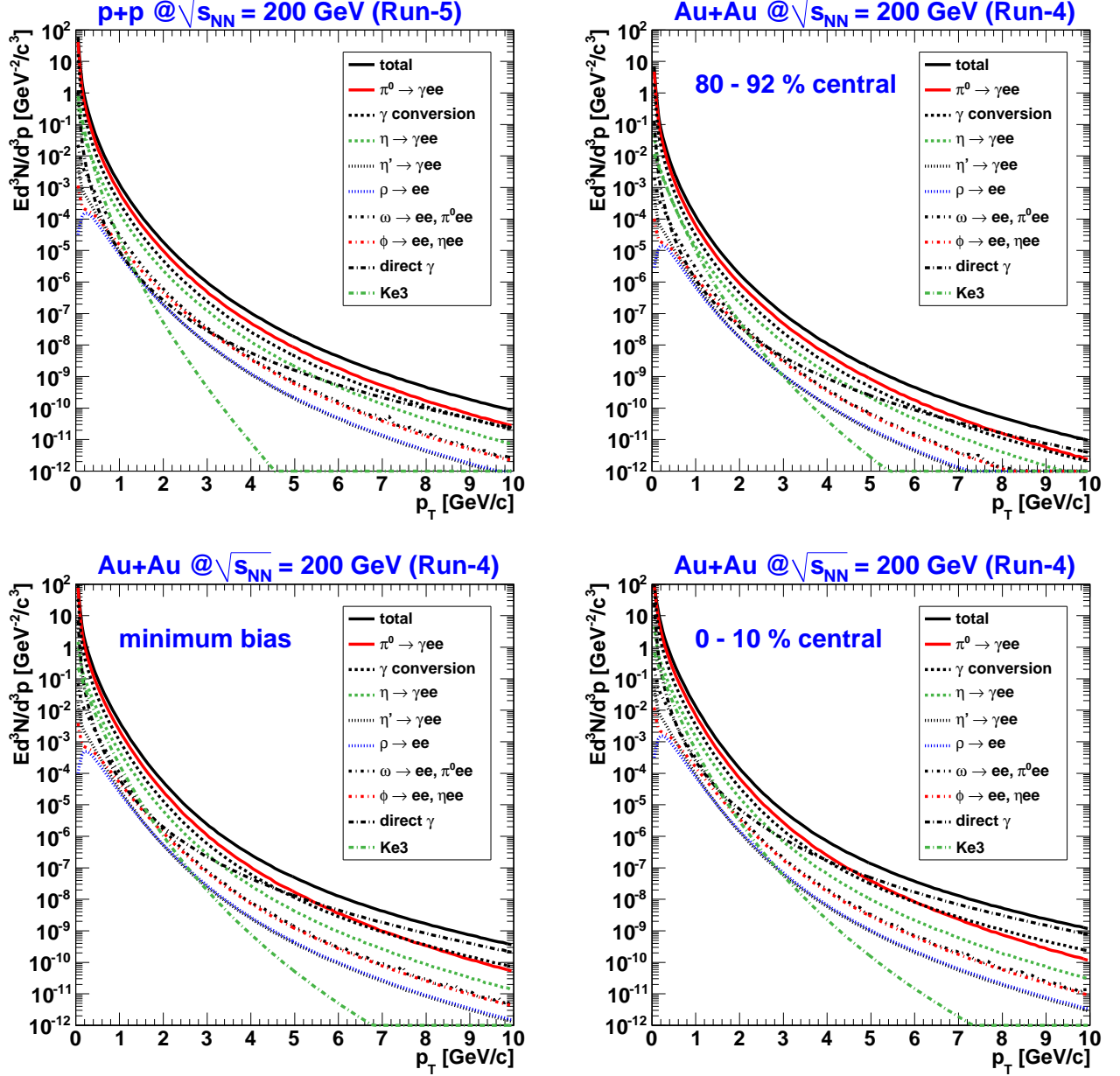


FIG. 13: (Color online) Invariant differential cross sections and multiplicity of electrons for electron cocktails in $p+p$ and Au+Au collisions at 200 GeV for the indicated centrality ranges.

error. In practice, the lower bound of the spectral shape is determined by the smaller Kaplan function normalized down a further 10%, while the upper bound is set by the larger m_T scaling function normalized up 10%.

While measured J/ψ p_T spectra exist at RHIC energies, the Υ p_T spectra have not been measured. Since the overall production cross section for Υ is estimated to be roughly 1% of that of the J/ψ , contributions from Υ decay contribute much less to the single electron cocktail. A NLO calculation for Υ production in the color evaporation model provides the input to the Monte Carlo calculation of the central value estimates [58]. Without a

measured Υ p_T spectrum to characterize the systematic uncertainty to the Monte Carlo input, the same relative systematic uncertainties derived from the J/ψ data are applied to the Υ cocktail estimate. Compared to the quoted uncertainties in the NLO calculation, the use of data-driven systematic uncertainties for the Υ provides a more conservative estimate.

A leading-order (LO) Drell-Yan calculation [59] of the single-inclusive lepton p_T spectrum, $p+p \rightarrow (e^+ + e^-)/2 + X$, is also included in the updated electron cocktail. The calculation is for $|y| < 0.5$ and uses the CTEQ6M parton distributions [60]. The scale used is p_T , no cut is placed

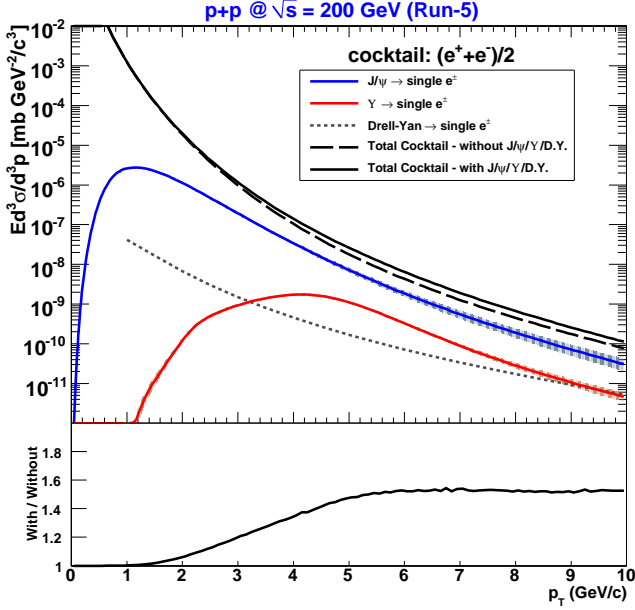


FIG. 14: (Color online) Electron background cocktail with quarkonium and Drell-Yan contributions for $p + p$ collisions.

on the lepton pair mass, and a K-factor of 1.5 is applied.

Figure 14 shows the cocktail for $p+p$ collisions with the quarkonium and Drell-Yan contributions. The bottom section of the plot shows the ratio of the cocktail with the quarkonium and Drell-Yan to that without.

PHENIX has measured the J/Ψ p_T spectrum out to 5 GeV/ c in Au+Au collisions at 200 GeV [61]. In order to extrapolate out to higher p_T , the measured J/Ψ spectrum from $p + p$ collisions is scaled by R_{AA} and N_{coll} . Above 5 GeV/ c , two extreme scenarios are considered, and the difference in the two resulting estimates for the extrapolation is assumed as a systematic error. In the first scenario, the R_{AA} is kept constant from its value at 5 GeV/ c . In the second scenario, the R_{AA} is assumed to increase linearly from its value at 5 GeV/ c up to a value of 1 at 10 GeV/ c , above which it is assumed to be constant. Figure 15 shows the cocktail with quarkonium and Drell-Yan contributions for 0-20% centrality Au+Au collisions.

The J/Ψ spectrum in Au+Au collisions has not been measured separately for 0–10% and 10–20% centralities. In order to estimate the electron background in these centralities separately, we assume that the R_{AA} of J/Ψ is the same in 0–10% and 10–20% centrality collisions.

J. Converter subtraction method

The yields of photonic and nonphotonic electrons are obtained by measuring the difference between inclusive electron yields with and without a photon converter of precisely known thickness: a brass sheet of 1.680 % radiation length (X_0). Figure 16 shows the corresponding

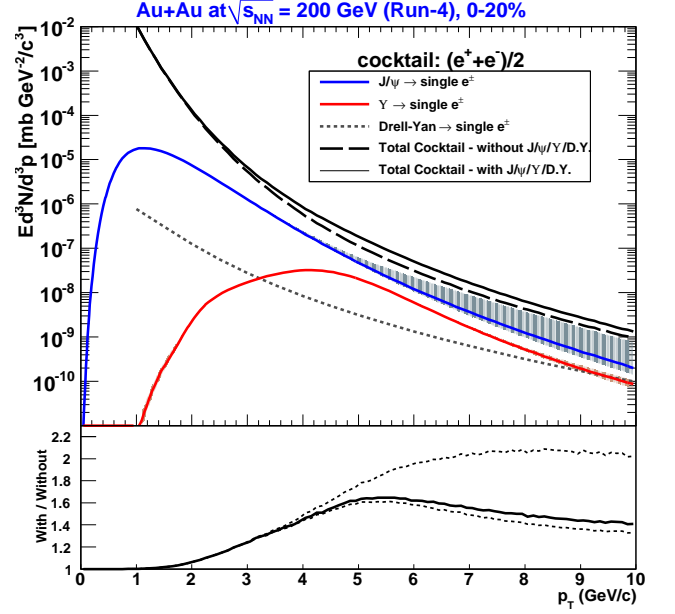


FIG. 15: (Color online) Electron background cocktail with quarkonium and Drell-Yan contributions for 0-20% centrality Au+Au collisions.

p_T^e spectra for MB events.

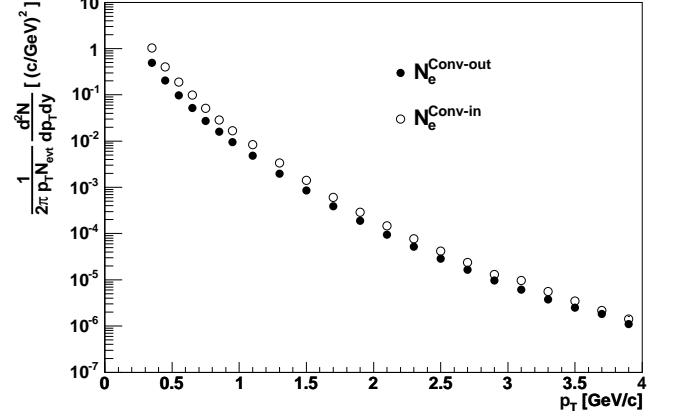


FIG. 16: Invariant yields of inclusive electrons with (open circles) and without (filled circles) the photon converter for MB events.

These yields can be expressed as the following relations:

$$N_e^{\text{Conv-out}} = N_e^\gamma + N_e^{\text{Non-}\gamma}, \quad (7)$$

$$N_e^{\text{Conv-in}} = R_\gamma N_e^\gamma + (1 - \epsilon) N_e^{\text{Non-}\gamma}. \quad (8)$$

Here, $N_e^{\text{Conv-in}}$ ($N_e^{\text{Conv-out}}$) is the measured electron yield with (without) the converter. N_e^γ ($N_e^{\text{Non-}\gamma}$) is the photonic (nonphotonic) electron yield. ϵ represents a small loss of $N_e^{\text{Non-}\gamma}$ due to the converter. This blocking

factor has been already evaluated in a previous measurement ($\epsilon \sim 2.1\%$) [26]. The main issue in this calculation is to determine R_γ , i.e., to understand how much the photonic electron yield is increased by the converter. The main source of photonic electrons is a mixture of mesons (π^0 , η , η' , ω , and ϕ) decaying into real or virtual photons with their different p_T slopes.

TABLE VII: Radiation length (L) of material near the interaction point. The conversion probability (P^{Conv}) is calculated for the case of electrons emitted at $p_T^e = 1.0$ GeV/ c .

Material	L (X_0)	P^{Conv}
Beam pipe (Be)	0.288%	0.201%
Air ($r < 30$ cm)	0.099%	0.069%
Total	0.387%	0.270%
Converter (brass)	1.680%	1.226%

To calculate R_γ , it is necessary to know exactly the material amounts near the interaction point. Table VII shows a list of each material thickness in units of radiation length. To reduce the air contribution, a helium bag was installed in the space surrounded by the DC ($0.3 < r < 1.0$ m). The converter sheet was rolled just around the beam pipe in converter runs. The conversion probability (P^{Conv}) in Tab. VII is calculated for the case of electrons emitted at $p_T^e = 1.0$ GeV/ c . The equivalent conversion probability of a virtual photon in π^0 Dalitz decay (P^{Dalitz}) is 0.598% [62]. R_γ can be estimated with these values at $p_T^e = 1.0$ GeV/ c .

$$R_\gamma = \frac{P^{\text{Conv}} + P^{\text{Dalitz}} \text{ (with converter)}}{P^{\text{Conv}} + P^{\text{Dalitz}} \text{ (without converter)}} \sim 2.41. \quad (9)$$

To obtain a more realistic value of R_γ considering geometrical effects, GEANT-based Monte-Carlo simulations [46] for photon conversions were performed with and without the converter. R_γ is determined for π^0 and η separately. We use the π^0 spectrum measured by PHENIX as the input for the π^0 simulation and assume m_T scaling ($p_T \rightarrow \sqrt{p_T^2 + m_\eta^2 - m_{\pi^0}^2}$, normalized at high p_T to $\eta/\pi^0 = 0.48 \pm 0.1$) to obtain the input for the η simulation. Since the η mass is larger than the π^0 mass, the phase space of η Dalitz decay is slightly larger than that of π^0 Dalitz decay. The relative branching ratio (Dalitz decay)/(two γ decay) is 1.2% for π^0 and 1.5% for η [63]. This difference makes R_η^γ smaller than R_π^γ . Contributions from other mesons which undergo Dalitz decay (η' , ρ , ω , and ϕ) are small (6% at $p_T = 3$ GeV/ c , and smaller at lower p_T). The particle ratios at high p_T ($\eta'/\pi^0 = 0.25 \pm 0.13$, $\rho/\pi^0 = \omega/\pi^0 = 1.0 \pm 0.5$, $\phi/\pi^0 = 0.4 \pm 0.2$) are used to determine R_γ . The ϕ/π^0 ratio used here is consistent with our π^0 and ϕ measurement. The uncertainties in the particle ratios are included in the systematic uncertainties of R_γ . For this method, it is essential that the amount of material is accurately modeled

in the simulation. We compared the yield of identified photon conversion pairs in the data and in the simulation, and concluded that the simulation reproduces R_γ within $\pm 2.7\%$. This uncertainty is included in the overall systematic uncertainty.

In the upper plot in Fig. 17, R_γ is indicated as a solid curve, which is compared with the ratio of the inclusive electron yield with/without the photon converter (R_{CN}):

$$R_{\text{CN}} \equiv \frac{N_e^{\text{Conv-in}}}{N_e^{\text{Conv-out}}} = \frac{R_\gamma + (1 - \epsilon)R_{\text{NP}}}{1 + R_{\text{NP}}}. \quad (10)$$

Here, R_{NP} is the ratio of nonphotonic/photonic electron yields ($N_e^{\text{Non-}\gamma}/N_e^\gamma$). If there were no nonphotonic contributions ($R_{\text{NP}} = 0$), then we would have $R_{\text{CN}} = R_\gamma$. The lower plot in Fig. 17 shows that R_{CN} gradually decreases with increasing p_T^e , while R_γ slightly increases with p_T^e . The difference between R_{CN} and R_γ proves the existence of nonphotonic electrons.

The converter method is applied for $0.3 \leq p_T^e < 1.6$ GeV/ c , and the cocktail method is applied for $p_T^e \geq 1.6$ GeV/ c . Boxes in the lower plot in Fig. 17 are systematic errors of R_{NP} from each method. R_{NP} increases with p_T^e and is more than 1.0 in $p_T^e \gtrsim 1.6$ GeV/ c . This plot gives an important demonstration that the amount of conversion material is relatively small in PHENIX.

To tune the normalization of the photonic electron spectra in the cocktail, the converter/cocktail ratio of photonic electrons is calculated for all centrality classes in Au+Au collisions. The ratio in MB is fitted by a constant (converter/cocktail = 1.182). The constant is applied to correct the cocktail spectra of photonic electrons for all centrality classes in Au+Au collisions. The ratios of photonic electron yield from the converter method to that from the corrected cocktail method for all centrality classes in 2004 Au+Au collisions are shown in Fig. 18. The curves in each plot indicate the systematic errors of the cocktail method. Figure 19 shows the converter/cocktail ratio (after scaling by 1.182) of photonic electrons in 2005 $p+p$ collisions.

K. Kaon decay background

After the subtraction of photonic electrons, almost all of the remaining background is from kaon decays. Kaons contribute to the nonphotonic electron spectra via K_{e3} decay and are only substantial at low p_T^e (< 1 GeV/ c). Since kaons have a long lifetime, the decay electrons do not originate from the primary collision vertex. Therefore, their contribution can only be determined reliably in a full detector simulation. This simulation was performed similarly to the π^0 simulation. It is done for charged kaons and K_L^0 to estimate the final electron rate. The input spectra have a parametrization obtained by the PHENIX kaon measurements [49].

To compare kaon contributions with photonic and non-photonic electrons, the ratio of the electron yield from

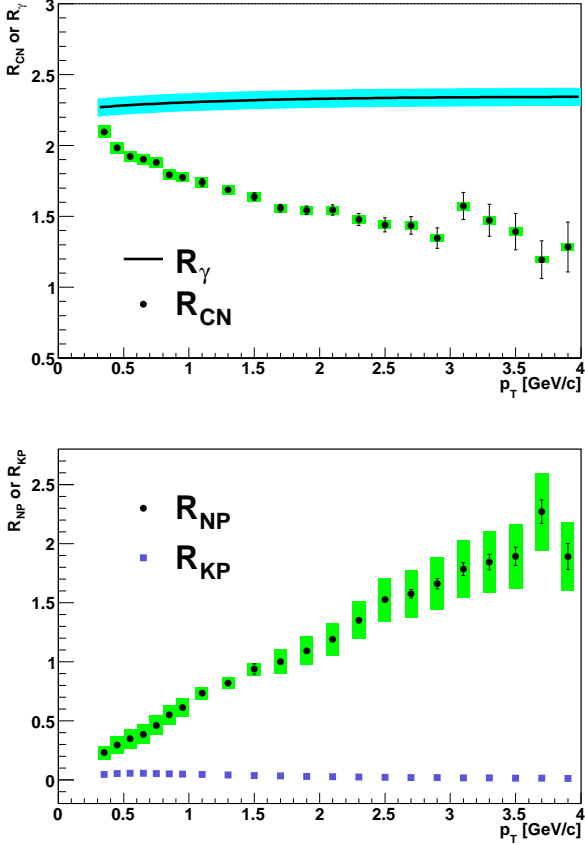


FIG. 17: (Color online) (upper) Ratio of inclusive electrons with/without the converter (R_{CN} , points with systematic error boxes) and ratio of photonic electrons with/without the converter (R_γ , solid line with a systematic error band). (lower) The ratio of nonphotonic yield to photonic electron yield (R_{NP} , filled circles) and the ratio of electron yield from kaon decays to photonic electron yield (R_{KP} , filled squares) as a function of p_T^e for MB. Filled circles with statistical error bars indicate R_{NP} produced by both the converter and cocktail methods.

kaon decays over the photonic electron yield (R_{KP}) is shown as filled squares in the lower plot of Fig. 17. The background from kaons becomes negligible above a p_T^e of 1 GeV/c.

L. Invariant spectra

The invariant cross section for single electrons from heavy-flavor decay in $p + p$ collisions is calculated using the following formula,

$$E \frac{d^3\sigma^{\text{HF}}}{dp^3} = \frac{1}{\mathcal{L}} \frac{1}{2\pi p_T} \frac{N_e^{\text{HF}}}{\Delta p_T \Delta y} \frac{1}{A\epsilon_{\text{rec}}} \frac{1}{\epsilon_{\text{bias}}}, \quad (11)$$

where \mathcal{L} is the integrated luminosity; N_e^{HF} is the electron yield from heavy-flavor decay after subtraction of photonic and nonphotonic background contributions; $A\epsilon_{\text{rec}}$

is the product of the geometrical acceptance and reconstruction efficiency described in III F. For the PH data set, $A\epsilon_{\text{rec}}$ also includes the PH trigger efficiency described in III G. The cross sections from the MB and the PH data sets are consistent with each other in overlapping p_T regions.

M. Systematic uncertainties in invariant spectra

In the $p + p$ analysis, systematic uncertainties are categorized into (a) inclusive electron spectra, (b) cocktail subtraction, and (c) converter subtraction. Category (a) is common to both the converter and cocktail methods, and includes the uncertainties in luminosity (9.6%), geometrical acceptance (4%), eID efficiency (3%) (from comparing to conversion electrons and simulation), and the PH trigger efficiency (3% at the plateau). Uncertainties in cocktail subtraction (category (b)) include the normalization (8%) and p_T dependent shape uncertainty (2% at $p_T \simeq 2$ GeV/c, increasing to 6% at 9 GeV/c) which originates from increased measurement errors on the background sources. In the converter analysis (category (c)) the dominant uncertainties are in R_γ (2.7%) and in the relative acceptance in the converter and the normal runs (1.0%).

In the Au+Au analysis there is no trigger efficiency correction, but there is additional uncertainty from the correction due to multiplicity-dependent efficiency loss. A conservative systematic uncertainty of 4% was added, ascertained from the differences of the two columns in Table V.

These uncertainties are propagated into the uncertainties in the heavy-flavor electron yields and added in quadrature. At low (high) p_T the uncertainties are amplified (reduced) to large (small) uncertainties in the heavy-flavor electron signal by approximately a factor of $1/(S/B)$, where S/B is the ratio of the nonphotonic electron yield to the photonic electron yield.

N. Inclusive electron v_2

The value of the inclusive electron v_2 was measured with the reaction plane method which can be written as

$$\frac{dN}{d\phi} = N_0 \{1 + 2v_2 \cos(2(\phi - \Psi))\}, \quad (12)$$

where N_0 is a normalization constant, ϕ is the azimuthal angle of electrons, and Ψ is the reaction plane angle. The reaction plane was determined from the multiplicity in each segment of the beam-beam counters. As the measurement of the reaction plane is sensitive to non-flow effects such as jets, resonance decays and HBT correlations, the reaction plane was measured in two well-separated rapidity intervals. Since each BBC is roughly three units of pseudorapidity away from the central arms, non-flow effects in the reaction plane measurement are

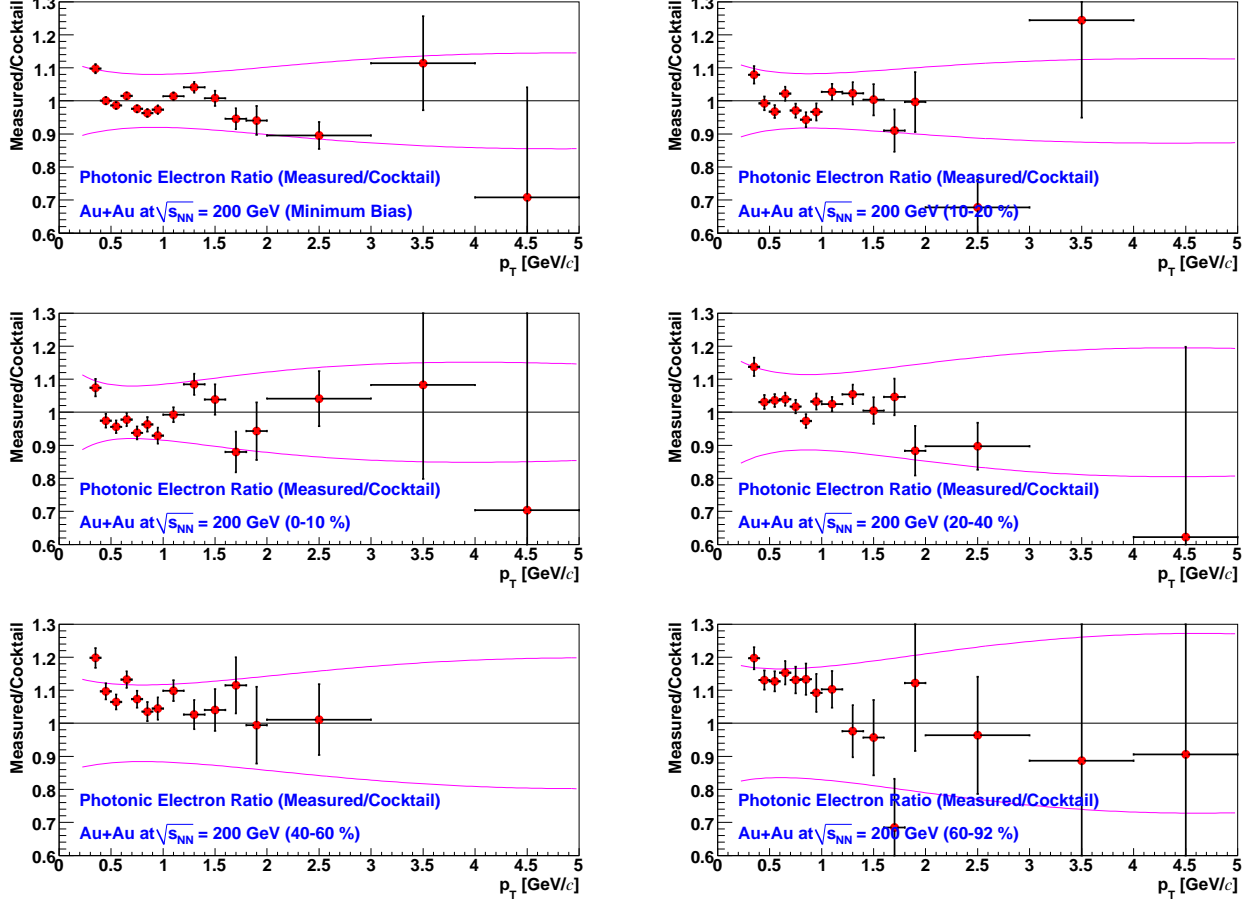


FIG. 18: (Color online) The ratio of photonic electrons measured by the converter method to the cocktail calculation in Au+Au collisions for the indicated centralities. The upper and lower curves show the systematic error of the cocktail. Error bars are statistical only.

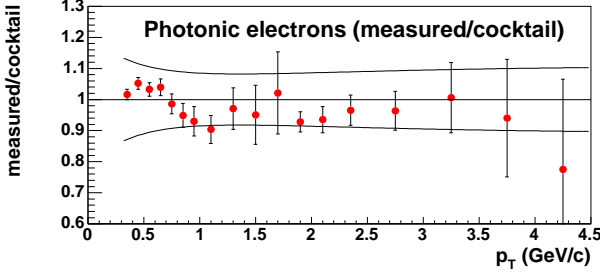


FIG. 19: (Color online) The ratio of photonic electrons measured by the converter method to the cocktail calculation in 2005 $p+p$ collisions. The data from the MB (PH) data set are shown below (above) 1.8 GeV/c. The upper and lower curves show the systematic error of the cocktail. Error bars are statistical only.

expected to be small. Figure 20 shows the azimuthal distribution of inclusive electrons for various centrality and p_T ranges, fit to the form of Eqn. 12. One can see from the agreement of the curves and data points that

higher order Fourier coefficients do not contribute much to the measured azimuthal electron distribution. Using the reaction plane measured with the BBCs, the inclusive electron v_2 was calculated as $v_2 = \langle \cos(2(\phi - \Psi_{\text{meas}})) \rangle$. The true v_2 with respect to the true reaction plane can be expressed in terms of the observed v_2 with respect to the measured reaction plane as [64, 65]

$$v_2 = \frac{v_2^{\text{meas}}}{\langle \cos(2(\Psi_{\text{meas}} - \Psi_{\text{true}})) \rangle}. \quad (13)$$

Two methods were used to extract $\langle \cos(2(\Psi_{\text{meas}} - \Psi_{\text{true}})) \rangle$. The first is an analytical calculation [64, 65]

$$\langle \cos(2(\Psi_{\text{meas}} - \Psi_{\text{true}})) \rangle = \frac{\sqrt{\pi}}{2\sqrt{2}} \chi \exp\left(\frac{-\chi^2}{4}\right) \left[I_0\left(\frac{\chi^2}{4}\right) + I_1\left(\frac{\chi^2}{4}\right) \right] \quad (14)$$

where χ is equal to $v_2^{\text{meas}} \sqrt{2N}$, and N is the BBC multiplicity. This method was verified to be well approximated

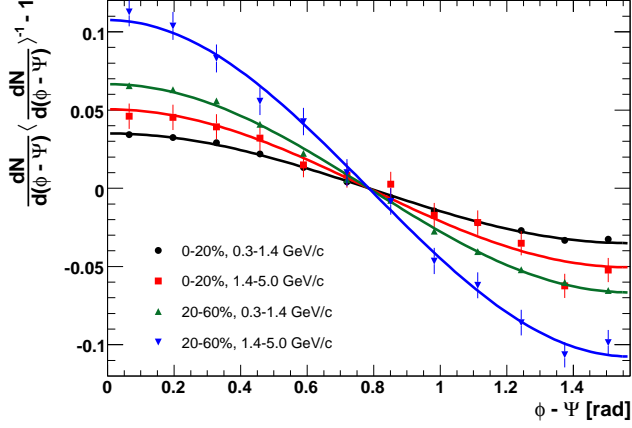


FIG. 20: (Color online) Azimuthal distributions relative to the reaction plane for various centrality and transverse momenta. The distributions have been normalized to their average value and centered around 0.

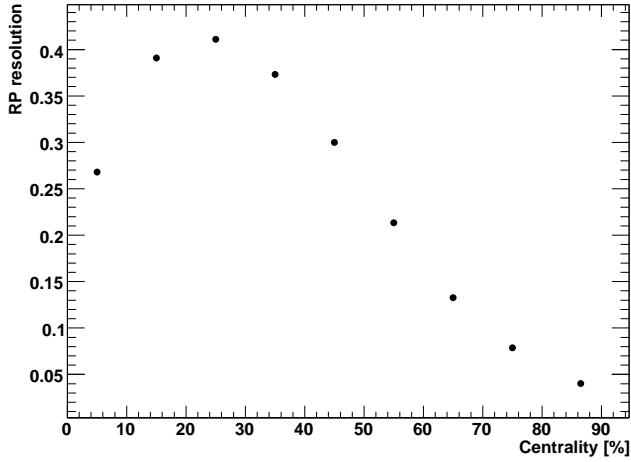


FIG. 21: Reaction plane resolution as a function of centrality.

by [65]

$$\langle \cos(2(\Psi_{\text{meas}} - \Psi_{\text{true}})) \rangle \sim \sqrt{2 \langle \cos(2(\Psi_{\text{meas}}^N - \Psi_{\text{meas}}^S)) \rangle} \quad (15)$$

with $\Psi_{\text{meas}}^{N(S)}$ is the measured reaction plane using only the north (south) BBC.

Figure 21 shows the reaction plane resolution determined from Equation 15. Less than 10% of background remains due to accidental RICH associations of hadrons. Contributions from such background sourced was subtracted as:

$$\frac{dN}{d(\phi - \Psi_{R.P.})} = \frac{dN_{\text{cand}}^e}{d(\phi - \Psi_{R.P.})} - \frac{dN_{\text{back}}^e}{d(\phi - \Psi_{R.P.})}, \quad (16)$$

where N_{cand}^e is the number of electrons identified by the RICH and N_{back}^e is the number of the background particles. The number of random associations are obtained by

replacing the north and the south sides of the RICH in the software, as described previously. The v_2 for a given centrality bin $[a, b]$ can be expressed as

$$v_2^{\text{bin}} = \frac{\int_a^b v_2^{\text{meas}}(C) \frac{dN_{e^+,e^-}}{dC} dC}{\int_a^b \frac{dN_{e^+,e^-}}{dC} dC}. \quad (17)$$

where $res(C)$ is the reaction plane resolution for a given centrality C . Due to lack of statistics, Equation 17 was approximated by a Riemann sum over 10% centrality bins. It was verified that v_2 is not sensitive to changing the bins for the Riemann sum. This is because the integrand in the numerator of Equation 17 is quite flat with centrality, as the resolution grows with both the measured v_2 and the particle multiplicity. Figure 22 shows the transverse momentum and centrality dependence of the inclusive electron v_2 . The minimum-bias v_2 is shown in Fig. 23.

O. Background v_2 cocktail

The azimuthal distribution of electrons ($dN^e/d\phi$) is given as the sum of the azimuthal distributions of photonic electrons ($dN^\gamma/d\phi$) and nonphotonic electrons ($dN^{\text{non-}\gamma}/d\phi$):

$$\frac{dN_e}{d\phi} = \frac{dN_e^\gamma}{d\phi} + \frac{dN_e^{\text{non-}\gamma}}{d\phi}. \quad (18)$$

Expanding Eq. 18 into the Fourier expansion, the non-photonic electron v_2 can be expressed as

$$v_{2_e}^{\text{non-}\gamma} = \frac{(1 + R_{\text{NP}})v_{2_e} - v_{2_e}^\gamma}{R_{\text{NP}}}. \quad (19)$$

where v_{2_e} is the v_2 of inclusive electrons, $v_{2_e}^\gamma$ is the v_2 of the photonic electrons, and R_{NP} is the ratio of non-photonic to photonic electron yields which was defined in section III J. The photonic electron v_2 can be estimated from the v_2 of electrons from various photonic sources as

$$v_{2_e}^\gamma = \sum R_i v_{2_e}^i \quad (20)$$

where R_i is the relative contribution of electron source i to the background and $v_{2_e}^i$ is electron v_2 from the electron source.

The dominant sources of photonic electrons are photon conversions and Dalitz decays from π^0 . In addition, we also took into account electrons from η and direct photon decays when calculating the photonic electron v_2 . The relative contributions of electrons from those sources are shown in Fig. 24. The other sources were ignored when calculating the photonic electron v_2 due to their small

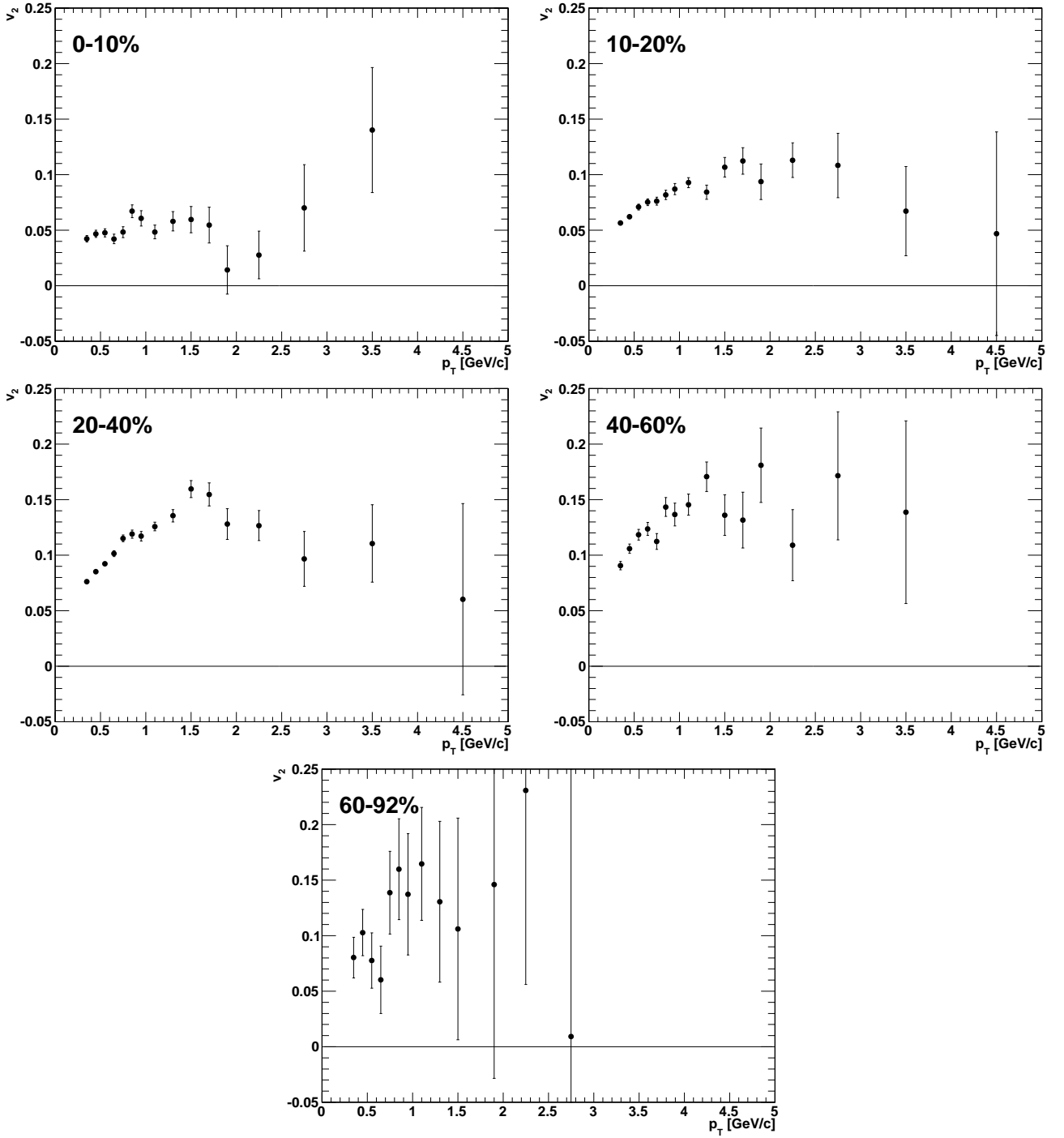


FIG. 22: p_T dependence of inclusive electron v_2 , for different centrality bins. A 5% systematic scale uncertainty is not shown.

contribution. The measured v_2 for π^\pm and π^0 was used as input for a simulation of $\pi^0 \rightarrow e^\pm v_2$, and transverse kinetic energy scaling [12] was assumed for the η , ρ , and ω . The direct photon v_2 was assumed to be zero. The decay electron v_2 from π^0 and η from Monte Carlo simulations are shown in Fig. 25 and Fig. 26. The photonic electron v_2 that was calculated from the results is shown in Fig. 27. The middle solid line is the mean value of

the photonic electron v_2 and the upper and lower dashed lines show one standard deviation of the systematic uncertainty. The uncertainty mainly comes from the uncertainty of the measured input v_2 . The v_2 from photonic sources for various centralities is shown in Fig. 27.

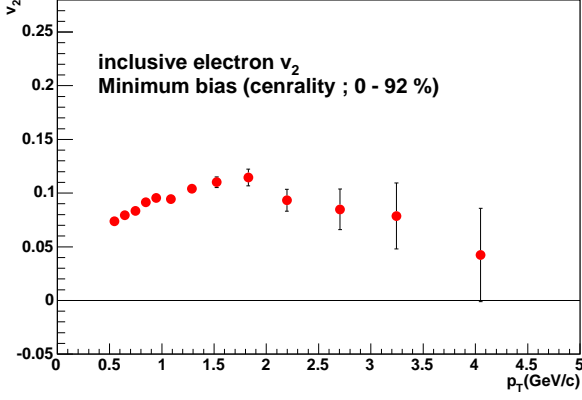


FIG. 23: (Color online) Inclusive electron v_2 for minimum bias events as a function p_T measured in Au+Au collisions at $\sqrt{s_{NN}} = 200$ GeV.

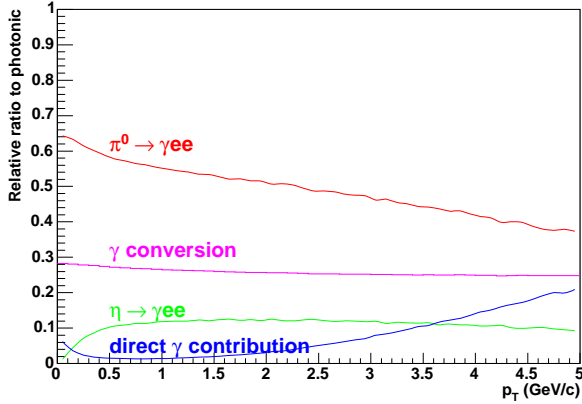


FIG. 24: (Color online) Relative contributions of electron v_2 from π^0 , η and direct γ to the background.

P. Photonic v_2 converter method

The photonic electron v_2 can be also determined by the converter method. Nonphotonic and photonic electron v_2 can be separated by using the inclusive electron v_2 measured with ($v_{2e}^{conv-in}$) and without ($v_{2e}^{conv-out}$) the converter as

$$v_{2e}^{non-\gamma} = \frac{R_\gamma(1 + R_{NP})v_{2e}^{conv-out} - (R_\gamma + R_{NP})v_{2e}^{conv-in}}{R_{NP}(R_\gamma - 1)} \quad (21)$$

$$v_{2e}^\gamma = \frac{(1 + R_{NP})v_{2e}^{conv-out} - (R_\gamma + R_{NP})v_{2e}^{conv-in}}{(1 - R_\gamma)}. \quad (22)$$

Figure 28 shows the inclusive electron v_2 with and without the converter. If the photonic electrons and non-photonic electrons have the same v_2 , the v_2 measured

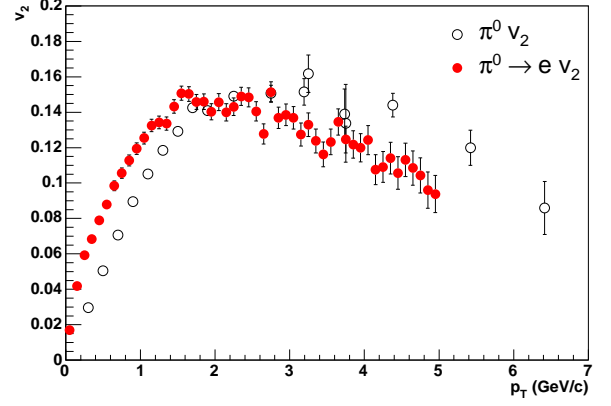


FIG. 25: (Color online) Electron v_2 from π^0 decay as a function of p_T , from a simulation.

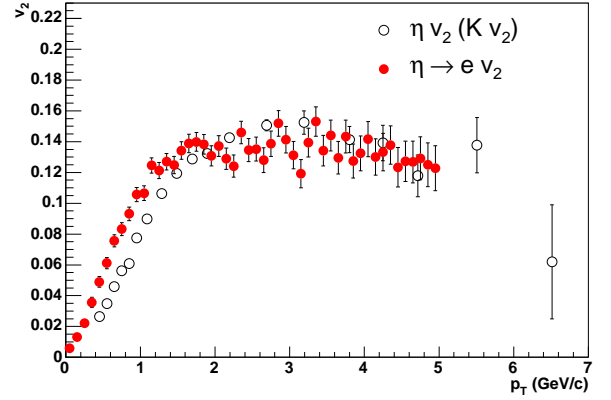


FIG. 26: (Color online) Electron v_2 from η decay as a function of p_T , from a simulation.

with and without the converter would be the same. Due to the small statistics of the converter runs, v_2 measured with the converter has a large statistical uncertainty. The photonic electron v_2 obtained by the converter method is shown as open squares in Fig. 29. The result is consistent with the photonic electron v_2 determined by the cocktail method within statistical uncertainty.

Q. Heavy flavor v_2 and systematic uncertainties

The remaining background after subtracting photonic background is kaon decay as described previously. The electron v_2 from kaon decays was also calculated by a Monte Carlo simulation assuming transverse kinetic energy scaling and it was removed from the nonphotonic electron sample. The electron v_2 from kaon decays was subtracted from the nonphotonic electron v_2 as

$$v_{2e}^{heavy} = \frac{v_{2e}^{non-\gamma} - R_{KNP}v_{2e}^K}{1 - R_{KNP}}. \quad (23)$$

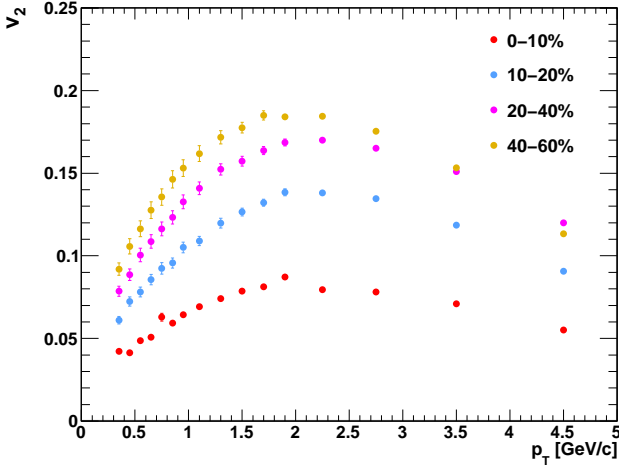


FIG. 27: (Color online) Electron v_2 from photonic sources as a function of p_T and centrality.

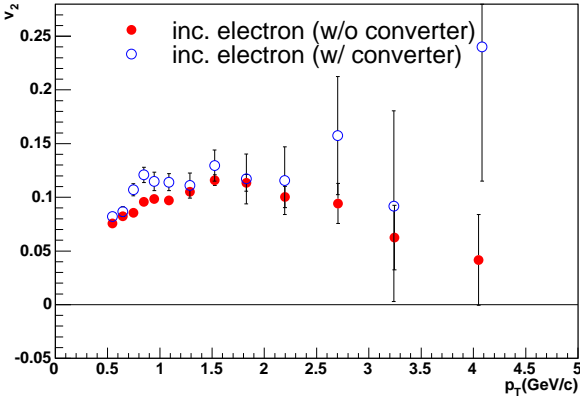


FIG. 28: (Color online) Inclusive electron v_2 with and without the converter installed.

Here R_{KNP} is the ratio of the yield of electrons from kaon decays and from all other nonphotonic sources ($R_{KNP} = N_e^K / N_e^{\text{non-}\gamma}$), and v_2^{heavy} is the v_2 of electrons from heavy flavor decays. After subtracting kaon decays, the main source of nonphotonic electrons remaining is heavy flavor decays.

Systematic uncertainties of the heavy flavor electron v_2 are summarized below.

- Reaction plane determination: The systematic uncertainty of the reaction plane determination was estimated by measuring the inclusive electron v_2 separately with the north BBC, the south BBC, and both the north and south BBCs combined. The maximum difference is about 5 % and we apply it as the uncertainty due to the reaction plane determination.
- Electron identification: The systematic uncertainty from electron identification was estimated by mea-

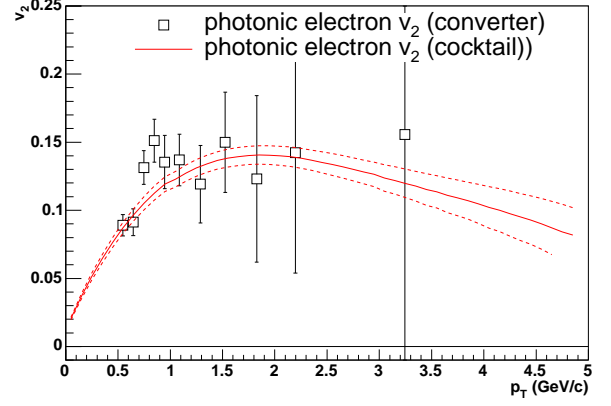


FIG. 29: (Color online) Photonic electron v_2 determined by two independent methods, the cocktail and the converter method. The lines are determined by the cocktail method and the squared points are obtained by the converter method.

suring the inclusive electron v_2 while changing the electron identification cuts from the standard cuts which were described in previous section. In this analysis we changed the cut parameters of E/p , n_0 and $\chi^2/npe0$. The relative change in v_2 from varying the cuts on E/p is about 2%, while for n_0 it is about 2% and for $\chi^2/npe0$ it is 1%. The total systematic uncertainty assigned from electron identification is 3 %.

- Background v_2 : As described in the previous section, the uncertainties from the photonic electron v_2 come from the π^0 v_2 and kaon v_2 , which have about 5 % uncertainties. We applied these values to the uncertainty of the photonic electron v_2 . We also applied 5 % for the v_2 from three-body kaon decays.
- R_{NP} : The systematic uncertainty of R_{NP} comes from the uncertainties of inclusive electron spectra and the subtracted background spectra. The systematic uncertainty of the inclusive electron spectra includes the uncertainties in the geometrical acceptance, the reconstruction efficiency and the occupancy correction, as described previously.

The total systematic uncertainty was obtained by a quadratic sum of the above uncertainties.

IV. RESULTS

A. Heavy-flavor electron cross sections ($p + p$)

Fig. 30 (a) shows the invariant differential cross section of electrons from heavy-flavor decays. Fig. 30 (b) shows the yield divided by a FONLL calculation [66]. All background has been subtracted. The data from the two

analysis methods (converter and cocktail) are combined: at low p_T ($p_T < 1.6$ GeV/ c) the converter subtraction method is applied to the MB data set; at intermediate p_T ($1.6 < p_T < 2.6$ GeV/ c) the converter method is applied to the PH data set; and at high p_T ($p_T > 2.6$ GeV/ c) the cocktail method is applied to the PH data set.

Figure 31 shows the ratio of nonphotonic electrons (including charmonium, bottomonium, and Drell-Yan) to the photonic background.

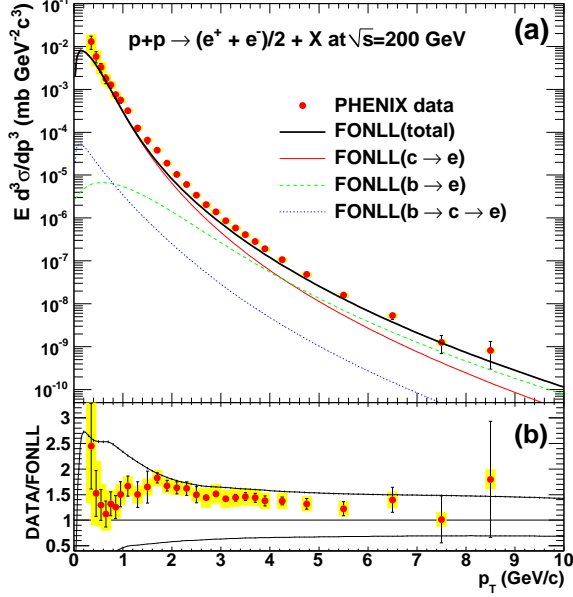


FIG. 30: (Color online) (a) Invariant differential cross sections of single electrons as a function of p_T in $p+p$ collisions at $\sqrt{s} = 200$ GeV. The error bars (bands) represent the statistical (systematic) errors. The curves are the FONLL calculations [66]. (b) The ratio of FONLL/Data as a function of p_T . The upper (lower) curve shows the theoretical upper (lower) limit of the FONLL calculation. In both panels, a 10% normalization uncertainty is not shown.

B. Heavy flavor electron invariant yield (Au+Au)

The differential invariant yield spectra as a function of p_T^e for the measured signal electrons from heavy flavor decays are calculated as in Eq. 24. N_i^{evt} is the number of events in a centrality class i ($i = 0-10\%$, $10-20\%$, $20-40\%$, $40-60\%$, and $60-92\%$). $\epsilon^{\text{Hadron}}(p_T^e)$ is the hadron contamination factor that is mentioned in III E. $\epsilon_{\Delta y}^{\text{acc}}(p_T^e)$ is the acceptance correction in III F. $\epsilon_i^{\text{embed}}$ is the embedding efficiency in III H. Δp_T^e is the p_T^e bin width. Δy is the rapidity range ($|y| < 0.5$) where the input e^\pm are distributed at the first stage of single particle simulation for the acceptance calculation (see III F). $N_i^{\text{HF}}(p_T^e, e^-)$ and $N_i^{\text{HF}}(p_T^e, e^+)$ are the resulting counts of signal electrons and positrons from heavy flavor decays by the converter method or cocktail method.

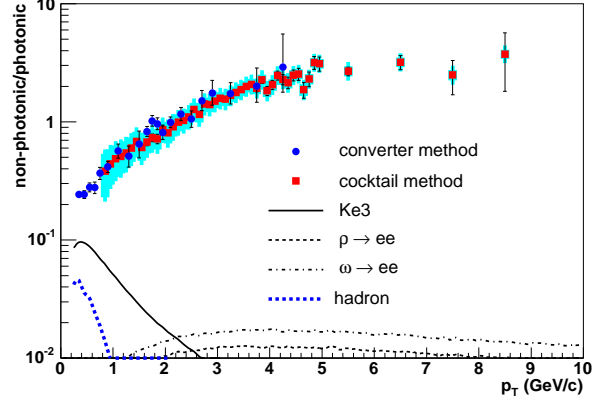


FIG. 31: (Color online) Ratio of nonphotonic electrons to photonic background. Error bars are statistical errors and the error bands show the cocktail systematic errors. The solid, dashed, dot-dashed, and dotted curves are the remaining nonphotonic background from Ke3 , $\rho \rightarrow e^+e^-$, $\omega \rightarrow e^+e^-$, and hadron contamination, respectively.

$$\frac{1}{2\pi p_T^e} \frac{d^2 N_i^{\text{HF}}}{dp_T^e dy} \equiv \frac{1}{2\pi p_T^e N_i^{\text{evt}}} \times \frac{1 - \epsilon^{\text{Hadron}}(p_T^e)}{\epsilon_{\Delta y}^{\text{acc}}(p_T^e) \cdot \epsilon_i^{\text{embed}}} \quad (24)$$

$$\times \frac{1}{\Delta p_T^e \Delta y} \times \frac{N_i^{\text{HF}}(p_T^e, e^-) + N_i^{\text{HF}}(p_T^e, e^+)}{2}$$

Figure 32 shows the invariant yield of inclusive and nonphotonic electrons in Au+Au collisions for various ranges in centrality. From top to bottom the spectra correspond to data in MB events, the five centrality classes, and the 2005 $p+p$ data. The various curves are fits to the $p+p$ data scaled by powers of ten for clarity (each factor is shown in the legend of Fig. 32). These spectra are produced by the converter method for $0.3 < p_T < 1.6$ GeV/ c and by the cocktail method for $1.6 < p_T < 9.0$ GeV/ c . The boxes and bars are systematic and statistical errors for each data point, respectively. Most of the nonphotonic electron yield is from the decay of open heavy flavor mesons. The curves overlaid in the right panel of Fig. 32 are the fit to the corresponding data from $p+p$ collisions with the spectral shape taken from a FONLL calculation [66] and scaled by the nuclear thickness function T_{AuAu} for each centrality class. They are also scaled by powers of ten for clarity. Each scaled FONLL curve almost agrees with the measured data in the low- p_T region. On the other hand, we can see the disagreement in the high- p_T region between the measured data and the FONLL curve in the minimum bias, 0–10%, 10–20%, and 20–40% centrality classes. The data points are lower than each FONLL curve at high- p_T . To quantify the suppression, the nuclear modification factor is calculated in the next subsection.

The insert box in the right panel of Fig. 32 shows the ratio of signal (electrons from heavy-flavor decays) to

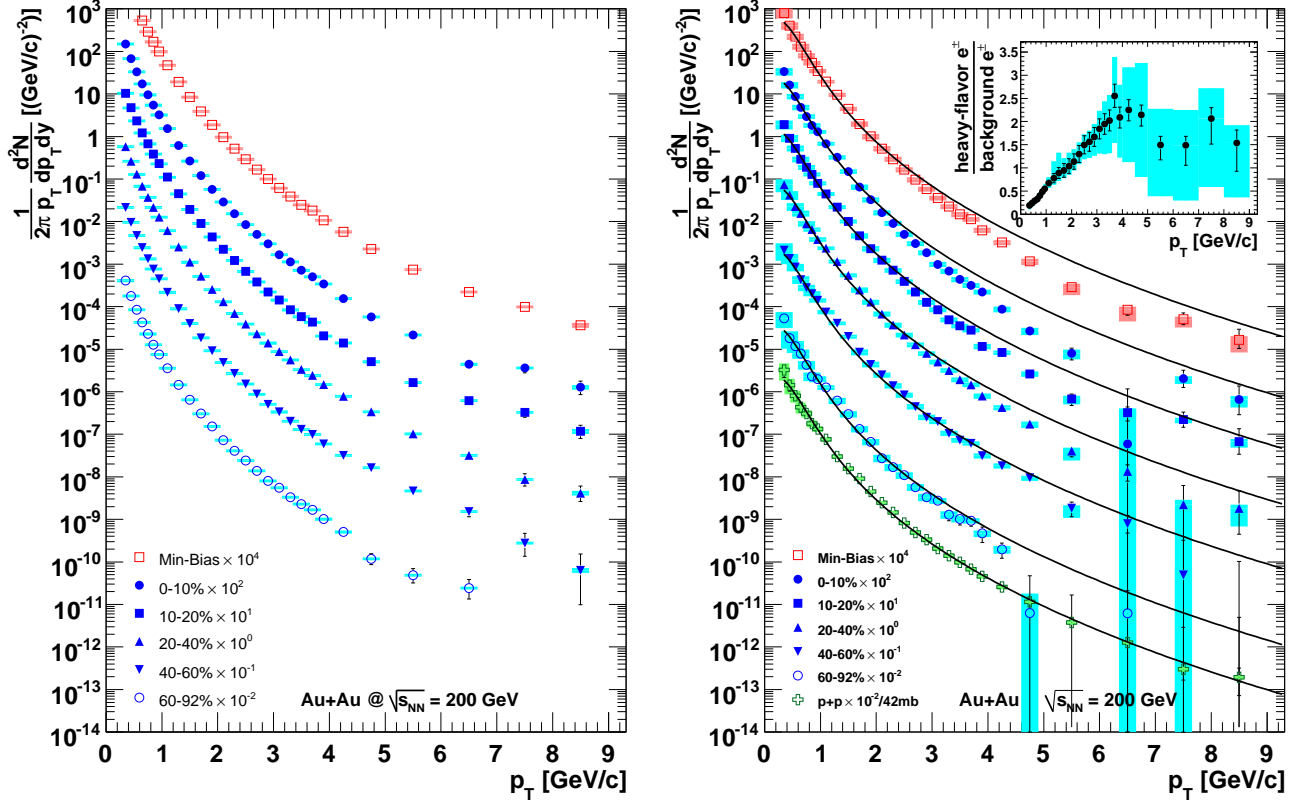


FIG. 32: (Color online) Invariant yields of (left) inclusive electrons and (right) open heavy flavor electrons for different Au+Au centrality classes, scaled by powers of ten for clarity. Error bars (boxes) depict statistical (systematic) uncertainties. The insert shows the ratio of these electrons to those from background sources in minimum bias events. The curves are scaled fits to the $p + p$ spectrum.

background as a function of p_T for minimum bias events. This signal/background ratio (R_{SB}) is calculated as:

$$R_{SB} = \frac{N_e^{HF}}{N_e^\gamma + N_e^{KV}} = \frac{N_e^{\text{Non-}\gamma} - N_e^{KV}}{N_e^\gamma + N_e^{KV}}. \quad (25)$$

Here, $N_e^{\text{Non-}\gamma}$ is the measured nonphotonic electron yield, N_e^γ is the yield of photonic electron background, and N_e^{KV} is the yield of electron backgrounds from kaons, vector mesons, quarkonia, and Drell-Yan. Filled circles with statistical error bars show R_{SB} produced by both the converter and cocktail methods. Boxes are systematic errors of R_{SB} . The yields from the converter and cocktail methods are combined at $p_T = 1.6$ GeV/c. The signal to background increases rapidly with p_T , reaching one for $p_T \approx 1.5$ GeV/c, reflecting the small amount of conversion material in the detector acceptance.

C. $R_{\text{AuAu}}(p_T)$

As seen in Fig. 32, the Au+Au spectra agree well with the $p+p$ reference at low p_T^e for all centrality classes, but a large suppression with respect to $p+p$ develops towards high p_T^e in central collisions. To quantify the suppression

effect, the nuclear modification factors, $R_{\text{AuAu}}(p_T^e)$ is calculated:

$$R_{\text{AuAu}}(p_T^e) = \frac{dN_{\text{AuAu}}^e/dp_T^e}{\langle N_{\text{coll}} \rangle \times dN_{pp}^e/dp_T^e} \quad (26)$$

$$= \frac{dN_{\text{AuAu}}^e/dp_T^e}{\langle T_{\text{AuAu}} \rangle \times d\sigma_{pp}^e/dp_T^e} \quad (27)$$

where $dN_{\text{AuAu}}^e/dp_T^e$ is the differential invariant yield in Au+Au collisions and dN_{pp}^e/dp_T^e ($d\sigma_{pp}^e/dp_T^e$) is the differential invariant yield (cross section) in $p+p$ collisions at a given p_T^e bin. For $p_T^e < 1.6$ GeV/c, dN_{pp}^e/dp_T^e ($d\sigma_{pp}^e/dp_T^e$) is taken from the 2005 $p + p$ data. At higher p_T , the fits shown in Fig. 32 are used to remove statistical fluctuations, and the statistical error is moved to a systematic error in the shape of R_{AuAu} . $T_{\text{AuAu}}(b)$ is the nuclear thickness function for A+A at an impact parameter (b) and $N_{\text{coll}}(b) = T_{\text{AuAu}}(b) \times \sigma_{pp}^{\text{in}}$. Here, σ_{pp}^{in} is the inelastic scattering cross section of $p+p$ collisions (42 [mb]). $R_{\text{AuAu}}(p_T^e)$ for each centrality class is shown in Fig. 33. Systematic errors consist of contributions from T_{AuAu} (a horizontal band around $R_{\text{AuAu}}(p_T^e) = 1.0$), and from $p+p$ and Au+Au data (vertical bands for each data point). The statistical errors are shown as vertical bars for each data point. Data points and errors for each centrality

class are listed in the Appendix.

If no nuclear modification exists and binary scaling is correct, R_{AuAu} should be unity. In all centrality classes, R_{AuAu} is consistent within errors with unity for $p_T < 2$ GeV/ c . However, we can see very clear suppression for 0–10%, 10–20%, 20–40%, and minimum bias events in the high- p_T region. This observed strong suppression in the high- p_T region indicates that the medium created by Au+Au collisions is so dense that not only light quarks, but also heavy quarks lose their energy, or merely that heavy quarks in Au+Au collisions are not produced as compared with scaled $p+p$ collisions. The total integrated yield in Au+Au collisions is compared with the binary-scaled yield in $p+p$ collisions in the next subsection.

D. Integrated $R_{\text{AuAu}}(N_{\text{part}})$

We calculate the p_T^e -integrated R_{AuAu} as a function of N_{part} as:

$$R_{\text{AuAu}}^{p_T^e}(N_{\text{part}}) = \frac{N_{\text{AuAu}}^e(p_T)}{\langle T_{\text{AuAu}} \rangle \times \sigma_{pp}^e(p_T)} = \frac{N_{\text{AuAu}}^e(p_T)}{\langle N_{\text{coll}} \rangle \times N_{pp}^e(p_T)} \quad (28)$$

where $N_{\text{AuAu}}^e(p_T)$ is the total electron yield above a transverse momentum of p_T . Figure 34 shows $R_{\text{AuAu}}^{p_T^e}(N_{\text{part}})$ for electrons from heavy-flavor decays for six different integrated p_T^e ranges as a function of the number of participant nucleons, N_{part} . When the lower limit of integration is reduced to $p_T^e = 0.3$ GeV/ c , which includes more than half of the heavy-flavor decay electrons predicted by the FONLL calculation in $p+p$ collisions, R_{AuAu} is close to unity for all N_{part} . This behavior suggests that the total yield of electrons from heavy flavor decays in Au+Au collisions is the same as the binary-scaled yield in $p+p$ collisions. The observed strong suppression phenomenon can be interpreted as the result of softened heavy quarks due to energy loss in the created medium. For $p_T^e > 0.6, 0.8, 2.0, 3.0,$ and 4.0 GeV/ c , R_{AuAu} decreases systematically with centrality. The behavior seems to be similar to the observed suppression for π^0 and η mesons [6, 50]. However, quantitative comparison with the suppression of the light mesons requires an understanding of the decay kinematics of open charm and bottom mesons.

E. Total charm cross section

We determine the total charm cross section in $p + p$ from the heavy-flavor electron invariant cross sections shown in Fig. 30. The heavy-flavor electron cross section at low p_T is dominated by charm, while the bottom contribution is small, order of 1%.

We follow the following steps to determine the total charm cross section.

1. The invariant cross section is extrapolated to $p_T=0$ to obtain the integrated cross section $d\sigma^e/dy$ at $y=0$ over all p_T .
2. The cross section is converted to a charm cross section at $y = 0$ ($d\sigma_{cc}/dy|_{y=0}$) using a total electron branching ratio of charm ($\text{BR}(c \rightarrow e)$) as

$$\frac{d\sigma_{cc}}{dy} = \frac{1}{\text{BR}(c \rightarrow e)} \frac{1}{C_{e/D}} \frac{d\sigma^e}{dy} \quad (29)$$

Here $\text{BR}(c \rightarrow e)$ is the total charm to electron branching ratio, and $C_{e/D} = 0.935$ is a kinematical correction factor to account for the difference of rapidity distribution of electrons and D mesons.

3. Finally, the cross section is extrapolated to the entire rapidity range to obtain the total charm production cross section $\sigma_{c\bar{c}}$.

We use two methods for the step 1. In the first method, the total charm cross section in $p + p$ collisions is derived by numerically integrating the heavy-flavor electron cross section for $p_T > 0.4$ GeV/ c : $d\sigma_e(p_T > 0.4)/dy = 5.79 \pm 0.59 \pm 1.64 \mu\text{b}$. Here the systematic uncertainty is obtained by integrating the upper and the lower systematic uncertainty limits of the differential cross section, since the systematic uncertainties are essentially coherent. We don't include the lowest p_T point, at $p_T = 0.35$ GeV/ c since its large individual uncertainty would make the uncertainty in the numerical integral larger. The cross section is then extrapolated to $p_T = 0$ using the spectrum shape predicted by FONLL: $d\sigma_e(p_T > 0)/dy = 10.6 \pm 1.1 \pm 3.2 \mu\text{b}$. Here we have assigned 10% (a quarter of estimated cross section for $p_T < 0.4$ GeV/ c) to the systematic uncertainty of the extrapolation, and have subtracted contributions from $b \rightarrow e$ and $b \rightarrow c \rightarrow e$ cascade decays ($0.1\mu\text{b}$).

In the second method for the step 1, we use PYTHIA to calculate the spectrum shape from charm decay electrons. Here we use PYTHIA as an event generator for D -meson decays. Since electrons are from D and other charm hadron decays, its momentum distribution in low p_T part and the high p_T part are correlated. If one can adjust the p_T distributions of charm hadrons so that the electron spectrum for just above the un-measured region, $p_T > 0.3$ GeV/ c , is reproduced, the p_T distribution in the lower p_T region should be well described by the simulation.

Figure 35 shows comparisons between the PYTHIA calculations and the data. The five curves in are from PYTHIA calculations, and the red points are from the data. The PYTHIA curves are fitted to the data for the fit range $0.3 < p_T < 1.6$ GeV/ c , with their normalization to be the sole fitting parameter. The shapes of PYTHIA curves are fixed. The PYTHIA curves underestimate the data for high p_T ($p_T > 1.6$ GeV/ c). However, in the p_T ranges that is used for the fit, the PYTHIA curves can reasonably describe the data. The five curves corresponds to 5 different choices of $\langle k_T \rangle$ ranging from

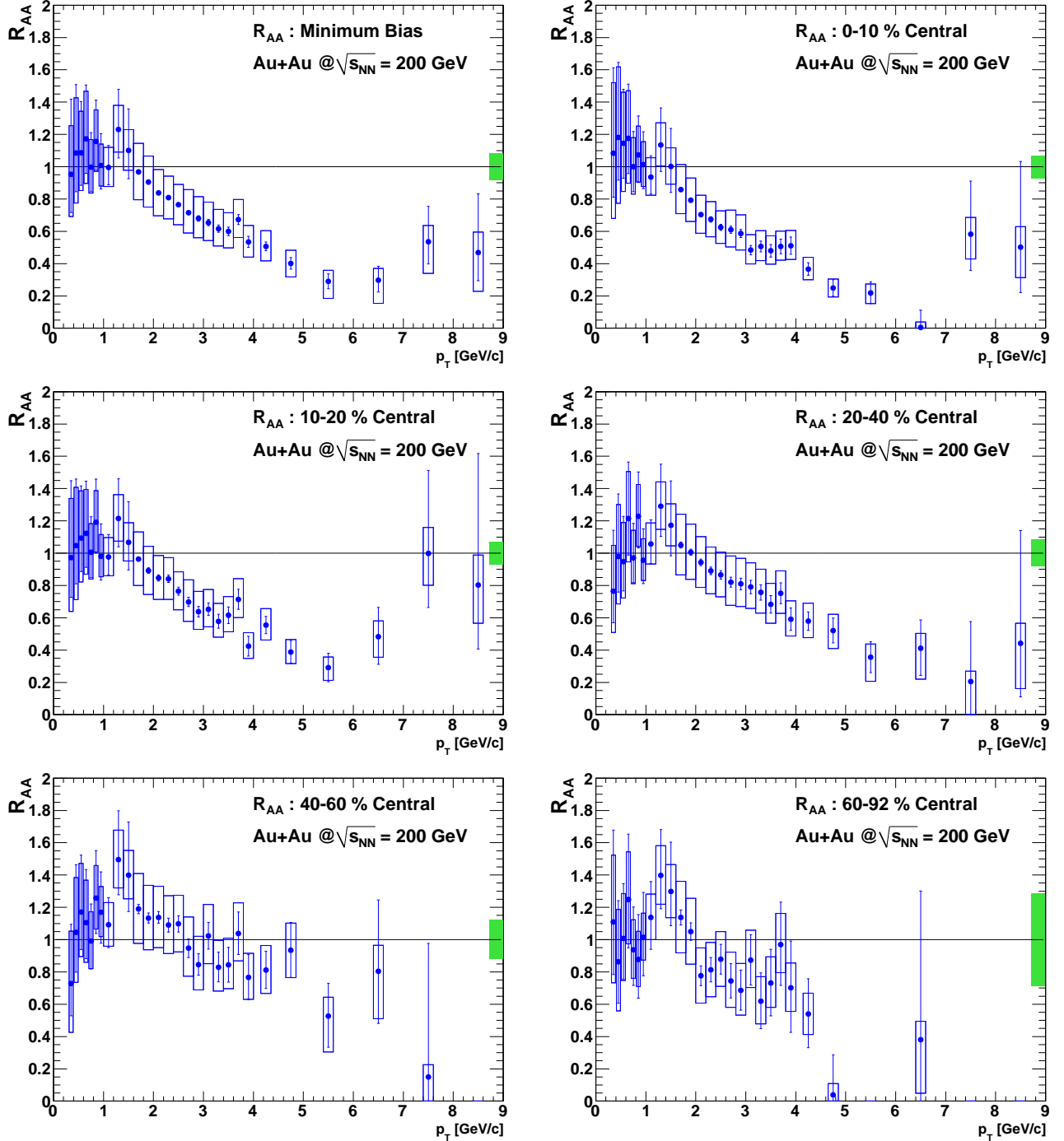


FIG. 33: (Color online) Open heavy flavor electron R_{AuAu} for the indicated centralities.

1.5 GeV/c to 3.5 GeV/c shown in the legend. The five curves are very similar in the low p_T region below the data. This is because the electron spectra in the region is mainly determined by the decay kinematics. Since the solid black curve ($\langle k_T \rangle = 2.5$ GeV/c) describes the data well, we use it as the central value. We note that similar values of $\langle k_T \rangle$ are found in our two hadron correlation analyses in $p + p$ [67].

Using the second method, we obtained $d\sigma^e/dy(p_T > 0) = 10.9 \pm 0.6 \pm 2.8 \mu b$. Here we have subtracted beauty contribution and added the systematic uncertainty of $\pm 1.4 \mu b$ in quadrature as the systematic uncertainty of this extrapolation procedure. This systematic uncertainty is estimated as 50% of the difference of the cross section with $\langle k_T \rangle = 3.5$ GeV/c (minimum cross section) and with $\langle k_T \rangle = 1.5$ GeV/c (maximum cross section).

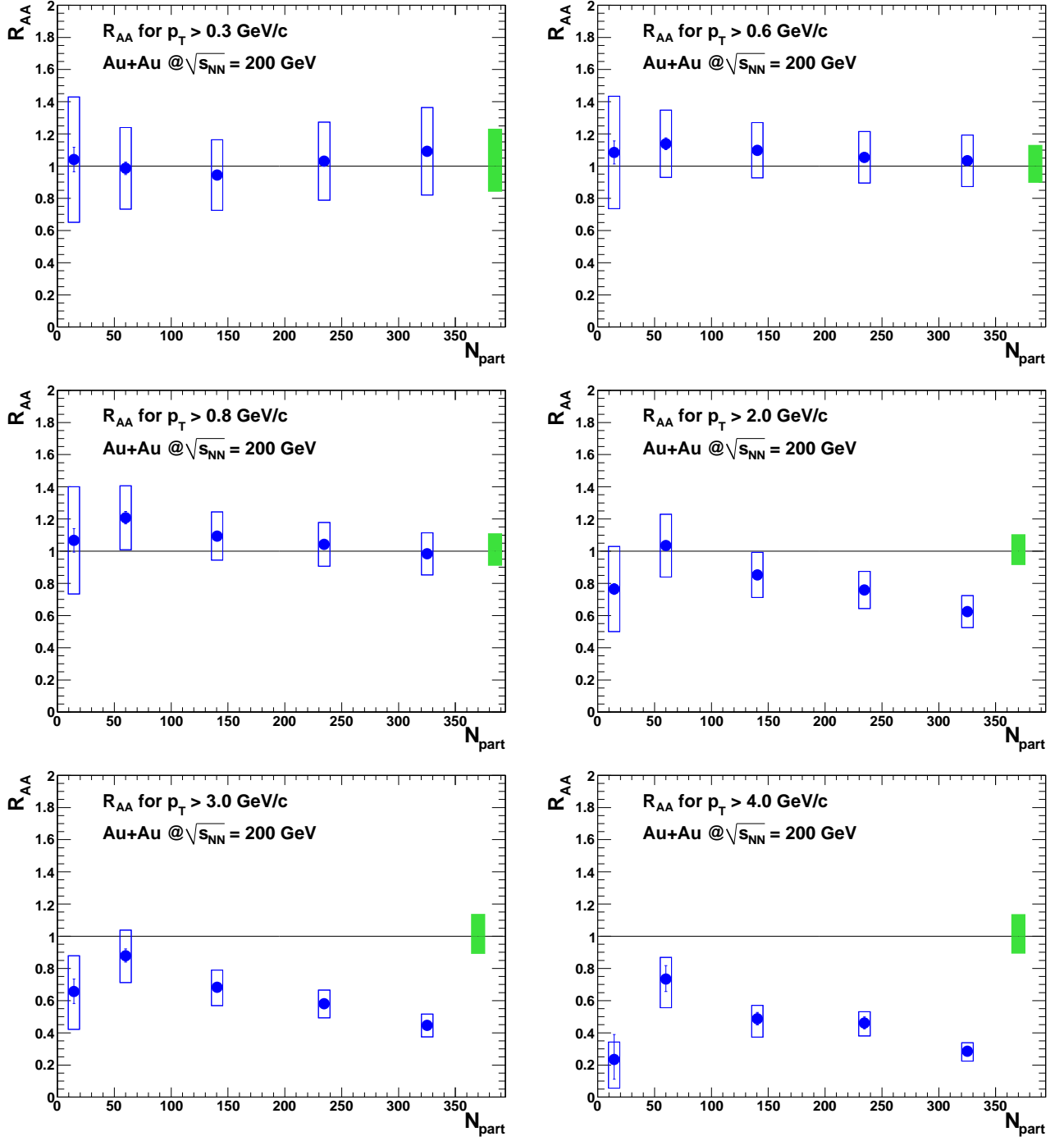


FIG. 34: (Color online) Nuclear modification factors R_{AuAu} for open heavy flavor electrons vs centrality, integrated above the indicated p_T^e ranges.

tion). Since the second method gives a value of $d\sigma^e/dy$ very close to that of the first method, we use the value obtained from the first method in the charm cross section calculation.

We determine the charm production cross section, $d\sigma_{c\bar{c}}/dy = 119 \pm 12 \pm 38 \mu\text{b}$ using Eq. (29). The branching ratio, $BR(c \rightarrow e) = 9.5 \pm 1.0\%$, is calculated us-

ing the following charmed hadron ratios: $D^+/D^0 = 0.45 \pm 0.10$, $D_s/D^0 = 0.25 \pm 0.10$, and $\Lambda_c/D^0 = 0.1 \pm 0.05$. In the step 3, we calculated the rapidity distribution of charm quark using HVQMNR [68] with CTEQ5M [69] PDF. The total charm cross section is determined to be $\sigma_{c\bar{c}} = 551 \pm 57^{\text{stat}} \pm 195^{\text{sys}} \mu\text{b}$. Here we have assigned a systematic uncertainty of 15% to the extrapolation to

TABLE VIII: Charm cross section per $N + N$ collision in centrality bins (0–10%,10–20%,20–40%,40–60%, 60–92% and Min Bias(MB)) in Au+Au and $p + p$. The second column showS the nuclear overlap integral T_{AA} of the centrality.

Centrality	T_{AA} (mb^{-1})	$\frac{d\sigma^e}{dy} _{p_T>0.4}$ (μb)	$\frac{d\sigma_{c\bar{c}}^e}{dy}$ (μb)	$\frac{d\sigma_{c\bar{c}}}{dy}$ (μb)	$\sigma_{c\bar{c}}$ (μb)
0–10%	22.8 ± 1.6	$6.50 \pm 0.12 \pm 0.92$	$11.9 \pm 0.2 \pm 2.0$	$134 \pm 2 \pm 27$	$620 \pm 11 \pm 156$
10–20%	14.4 ± 1.0	$6.30 \pm 0.13 \pm 0.96$	$11.6 \pm 0.2 \pm 2.1$	$130 \pm 3 \pm 27$	$600 \pm 12 \pm 155$
20–40%	7.07 ± 0.58	$6.15 \pm 0.13 \pm 1.07$	$11.3 \pm 0.2 \pm 2.2$	$127 \pm 3 \pm 29$	$586 \pm 12 \pm 159$
40–60%	2.16 ± 0.26	$6.64 \pm 0.22 \pm 1.28$	$12.2 \pm 0.4 \pm 2.6$	$137 \pm 5 \pm 33$	$633 \pm 21 \pm 180$
60–92%	0.35 ± 0.10	$5.98 \pm 0.42 \pm 1.68$	$11.0 \pm 0.8 \pm 2.4$	$123 \pm 9 \pm 39$	$570 \pm 40 \pm 201$
0–92% (MB)	6.14 ± 0.50	$5.96 \pm 0.08 \pm 0.96$	$10.9 \pm 0.2 \pm 2.1$	$123 \pm 2 \pm 27$	$568 \pm 8 \pm 150$
$p + p$	NA	$5.79 \pm 0.59 \pm 1.64$	$10.7 \pm 1.1 \pm 3.2$	$119 \pm 12 \pm 38$	$551 \pm 57 \pm 195$

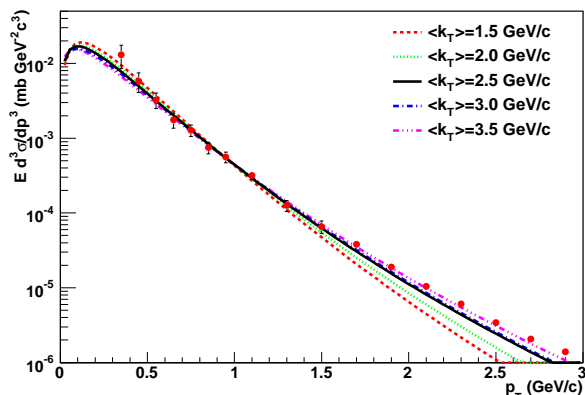


FIG. 35: (Color online) Comparison of electron p_T distribution calculated by PYTHIA and the data (filled circles). The five curves are electron p_T distributions from charm decay calculated using PYTHIA with different $\langle k_T \rangle$ values shown in the legend. All five curves are fitted to the data for $0.3 < p_T < 1.6$ GeV/c.

the full rapidity.

The charm cross section obtained here is slightly smaller than that published in [30] ($567 \pm 57^{\text{stat}} \pm 193^{\text{sys}} \mu\text{b}$) but agrees well within the systematic uncertainties. The difference comes from the fact that we now subtract the contributions from K_s^0 and J/ψ from the electron spectrum. The cross section is compatible with our previous measurement in the 2002 run [25] ($920 \pm 150^{\text{stat}} \pm 540^{\text{sys}} \mu\text{b}$) and agrees well with the value derived from the yield of the dielectron continuum [57] ($544 \pm 39^{\text{stat}} \pm 142^{\text{sys}} \pm 200^{\text{model}} \mu\text{b}$).

The FONLL cross section ($256_{-146}^{+400} \mu\text{b}$) is compatible with the data within its uncertainty. Although the data extends to high p_T where the bottom contribution is expected to be dominant, the present analysis does not separate charm and bottom contributions. The bottom cross section predicted by FONLL is $1.87_{-0.67}^{+0.99} \mu\text{b}$, and the upper FONLL curve is consistent with the data. The bottom cross section by FONLL is also consistent with the bottom cross section in $p + p$ we deduced from electron-hadron charge correlation [70] and dielectron continuum

mass distribution [57].

Total charm yields in Au+Au in various centrality bins are evaluated in a similar way from the heavy-flavor electron spectra. For each centrality bin, the heavy-flavor electron spectrum is integrated for $p_T > 0.4$ GeV/c to obtain $dN^e/dy|_{p_T>0.4}$. The electron cross section per $N + N$ collision, $d\sigma^e/dy|_{p_T>0.4}$ is then obtained as

$$\frac{d\sigma^e}{dy}|_{p_T>0.4} = \frac{1}{T_{AA}} \frac{dN^e}{dy}|_{p_T>0.4}. \quad (30)$$

The cross section is then extrapolated to $p_T = 0$ and the contribution from b decays and b cascade decays are then subtracted to obtain the electron cross section from charm decay per $N + N$ collision $d\sigma_{c\bar{c}}^e/dy$. Here we assume that $R_{AA} = 1.0$ for p_T -integrated b production. The cross section $d\sigma_{c\bar{c}}/dy$ is obtained using Eq.(29). Finally, the cross section is extrapolated to the full rapidity range using the rapidity distribution of charm from HVQMNR to obtain total charm cross section $\sigma_{c\bar{c}}$ per $N + N$ collision. We use the same correction factors $BR(c \rightarrow e)$, $C_{e/D}$, and rapidity distribution as in $p + p$ collisions. Table VIII summarizes the charm cross section per $N+N$ collisions in each centrality bins of Au+Au collisions. The charm cross sections per $N + N$ in Au+Au thus obtained agree well with the $p+p$ cross section for all centrality bins. The data are consistent with the results from our previous measurement in Au+Au collisions in the 2002 run [26] ($622 \pm 57^{\text{stat}} \pm 160^{\text{sys}} \mu\text{b}$ per NN).

Figure 36 shows $d\sigma_{c\bar{c}}^e/dy|_{p_T>0.4}$ per $N + N$ collision in Au+Au and $p + p$ as a function of N_{coll} . The cross section is more than half ($\simeq 54\%$) of the total electron cross section from charm decay $d\sigma_{c\bar{c}}^e/dy$. Fig. 33 shows that R_{AA} is consistent with unity for $p_T < 1.4$ GeV/c. Thus the shape of the electron spectrum in Au+Au and $p + p$ is almost independent of N_{coll} in the low p_T region. This indicates that the fraction of electron cross section below $p_T < 0.4$ GeV/c is almost independent of N_{coll} . In the following, we evaluate the N_{coll} dependence of the total charm cross section assuming that it is the same as the N_{coll} dependence of $d\sigma_{c\bar{c}}^e/dy|_{p_T>0.4}$.

To quantitatively evaluate the N_{coll} dependence of total charm cross section, we fit the data with a power-law function $A \cdot N_{\text{coll}}^\alpha$. We perform the fit with and without

TABLE IX: The results of power-law fits $A \cdot N_{\text{coll}}^\alpha$ shown in Fig. 36. In the fit, only statistical error is considered. The uncertainty of A and the first error of α are the statistical errors obtained from the fit. The second error of α is systematical uncertainty.

	$A(\mu\text{b})$	α	χ^2/NDF
Au+Au	6.00 ± 0.45	$1.0092 \pm 0.0120 \pm 0.0506$	6.4/3
Au+Au + pp	5.98 ± 0.34	$1.0097 \pm 0.0094 \pm 0.0403$	6.4/4

the $p + p$ data. The fitted curves are shown in Figure 36, and the results of the fits are summarized in Table IX.

Most of the sources of systematic uncertainties in the charm cross section are independent of N_{coll} and they do not affect the value of α . For the systematic uncertainties in α , we consider the following three remaining sources: (i) Multiplicity dependence of electron reconstruction efficiency (ii) systematic uncertainties in R_γ (iii) systematic uncertainties in T_{AA} . The systematic uncertainty from these sources are propagated to α and added in quadrature to obtain the total systematic uncertainty, which is shown as the second error of α in table IX. The value of α for Au+Au and $p + p$ combined is $\alpha = 1.0097 \pm 0.0094^{\text{stat}} \pm 0.0403^{\text{sys}}$, consistent with unity, indicating that total charm cross section scales with N_{coll} .

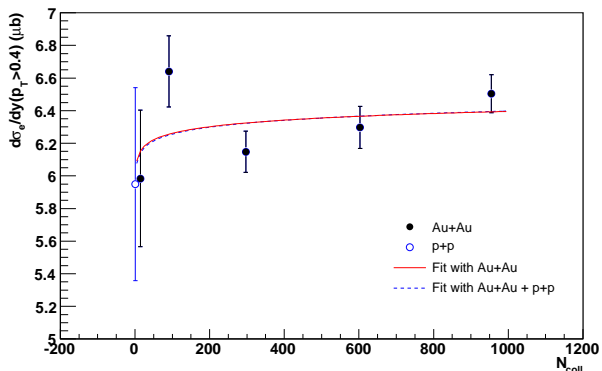


FIG. 36: (Color online) N_{coll} dependence of charm cross section per $N + N$ collisions in Au+Au and $p + p$ collisions. The error bar show the statistical errors only. The curves in the figure is the power-law fit $A \cdot N_{\text{coll}}^\alpha$.

F. Heavy flavor electron $v_2(p_T)$

The nonphotonic electron v_2 for minimum-bias events is shown in Fig. 37. The vertical lines are the statistical errors and the 1σ systematic uncertainties are shown as bands. The nonphotonic electron v_2 increases with p_T below 2.0 GeV/c then it saturates or perhaps decreases. This trend is similar to that of the meson v_2 (π and K). The main source of the nonphotonic electrons is semileptonic decays of heavy flavor mesons (charm and bottom).

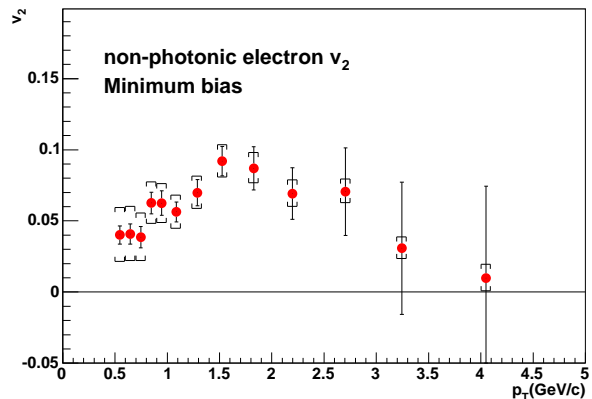


FIG. 37: (Color online) Nonphotonic electron v_2 as a function of p_T in Au+Au collisions at $\sqrt{s_{\text{NN}}} = 200$ GeV.

Therefore the nonphotonic electron v_2 that was obtained by subtracting photonic electrons and kaon decays from inclusive electrons should be dominated by heavy flavor electrons, which reflects the azimuthal anisotropy of heavy quarks. In this momentum region, electrons mainly decay from D mesons. Therefore the non-zero nonphotonic electron v_2 indicates that the D meson also has a non-zero v_2 .

Figure 38 show the v_2^{HF} for various centrality ranges. The p_T binning used is coarser than that shown in the minimum-bias v_2^{HF} due to lack of statistics. The v_2^{HF} for 60–93% collisions is not shown as the pion v_2 was not measured by PHENIX separately for that centrality range. At high p_T , the inclusive electron v_2 in the 60–93% centrality range was measured to be negative by between 2 and 3 standard deviations in the statistical error, and this accounts for the difference between the minimum-bias v_2^{HF} and the 0-60% v_2^{HF} .

V. DISCUSSION

A. Theory comparison ($R_{\text{AuAu}}(p_T^e)$)

Before the collection and analysis of RHIC data, it was generally expected that the dominant mechanism for the suppression of heavy quarks in the medium would be gluon radiation, and thus the heavy quarks would not be suppressed as much as the light quarks due to the dead-cone effect. Predictions from the BDMPS model and DGLV model for radiative energy loss can be seen in Fig. 39 [71, 72]. These models do not account for the suppression of the heavy flavor electrons, but they are sensitive to the relative admixture of D and B mesons produced in the collisions as D mesons are predicted to be suppressed due to gluon radiation more than are B mesons. However, recent measurements by PHENIX [70] suggest that the admixture of D and B is comparable to what was used in the BDMPS and DGLV calculations.

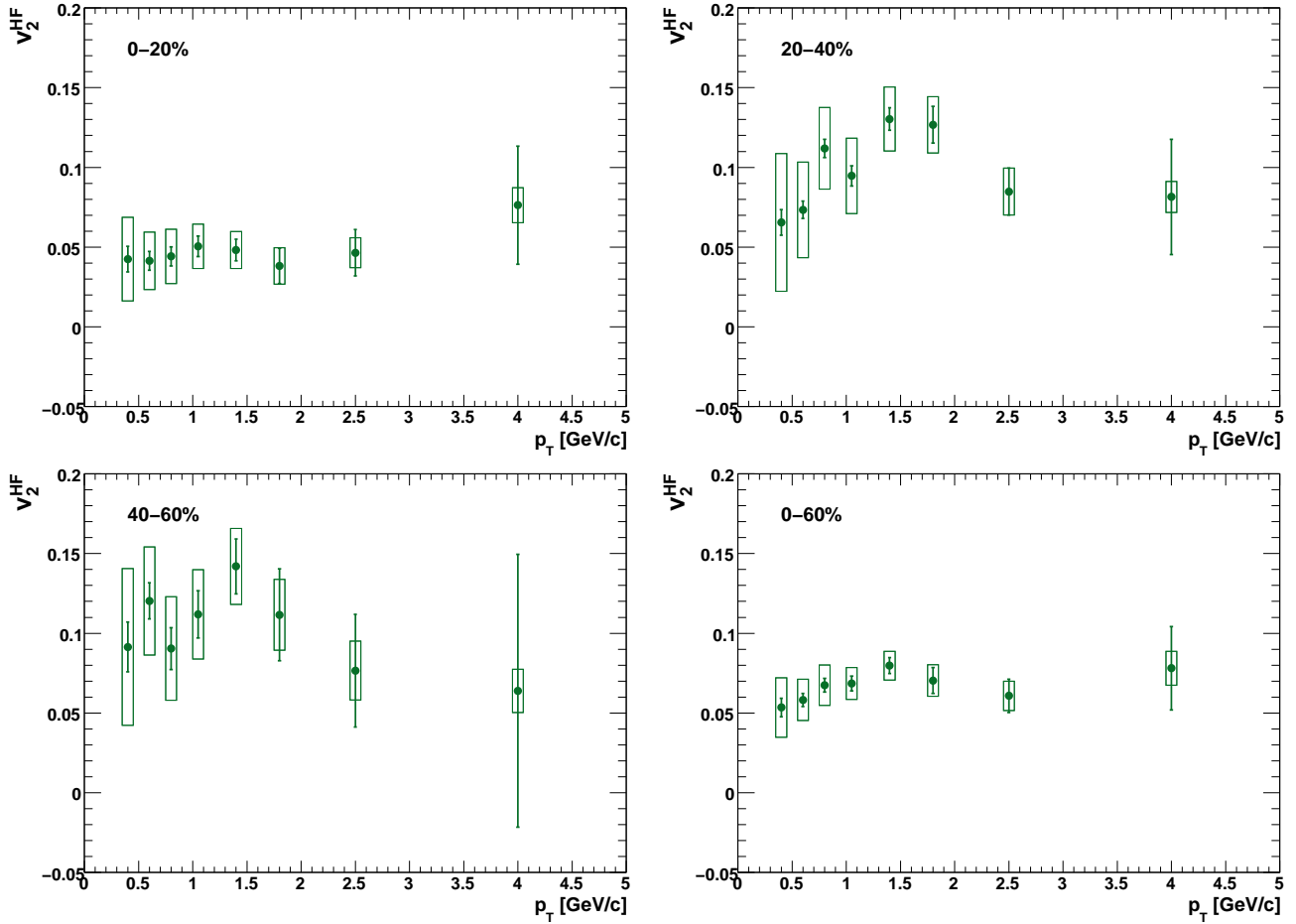


FIG. 38: (Color online) v_2^{HF} for the indicated centralities.

Mustafa [73] found that radiative and elastic scattering energy loss for heavy quarks are comparable over a very wide kinematic range accessible at RHIC. Contrary to what was previously thought, collisional energy loss should be taken into account in the calculation of suppression of heavy flavor mesons in Au+Au collisions. Figure 39 shows the DGLV prediction for suppression when collisional energy loss is taken into account in addition to radiative energy loss [72].

In [74], it was shown that a Langevin-based heavy quark transport model can qualitatively explain the large suppression (and azimuthal anisotropy) of electrons from heavy flavor decays in Au+Au collisions. The model places a heavy quark into a thermal medium, and assumes that the interaction of the heavy quark with the medium can be described by uncorrelated momentum kicks. Contrary to the models described above, the interaction in the Langevin model is given exclusively by elastic collisions, which is a good approximation for quarks which are not ultra-relativistic in the center of mass frame of the collision. The parameter which is tuned in this model is the heavy quark diffusion coefficient. While the above Langevin model fails to simultaneously describe R_{AA} and v_2 for a single value of the diffusion coef-

ficient, another Langevin-based model [75, 76] is in good agreement with both the suppression and anisotropy. In this model, the elastic scattering is mediated by resonance excitation of D and B-like states in the medium. The theoretical evidence for the existence of such resonance states comes from lattice computations. Figure 40 shows the calculations from these two models.

Recently, it has been suggested that collisional dissociation of heavy quarkonia in the quark-gluon plasma [77] may be a possible explanation for suppression of J/ψ production in heavy ion collisions. A. Adil and I. Vitev investigated the pQCD dynamics of open charm and bottom production and, in the framework of the GLV approach extended to composite $q\bar{q}$ systems, derived the medium induced dissociation probability for D and B mesons traveling through dense nuclear matter [78]. They showed that the effective energy loss, which arises from the sequential fragmentation and dissociation of heavy quarks and mesons, is sensitive to the interplay between the formation times of the hadrons and QGP and the detailed expansion dynamics of hot nuclear matter. Figure 41 shows their result as the band.

Most of the models calculate the nonphotonic electron production assuming the same chemical composition of

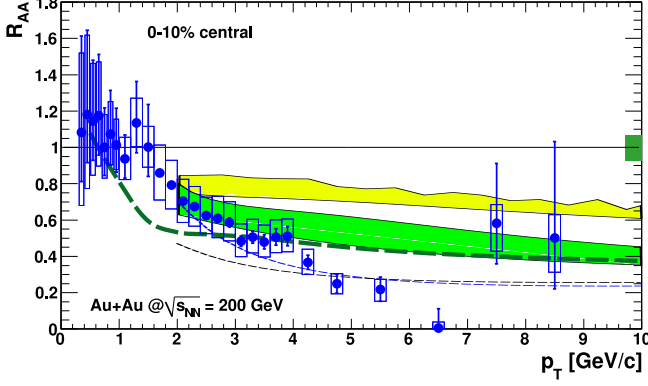


FIG. 39: (Color online) R_{AuAu} in 0–10% centrality class compared with energy loss models. The thick dashed curve is the BDMPs [71] calculation for electrons from D and B decays. The bands are DGLV [72] calculations for electrons from D and B decays. The lower band contains collisional energy loss as well as radiative energy loss. The thin dashed curves are DGLV calculations for electrons from D decays only.

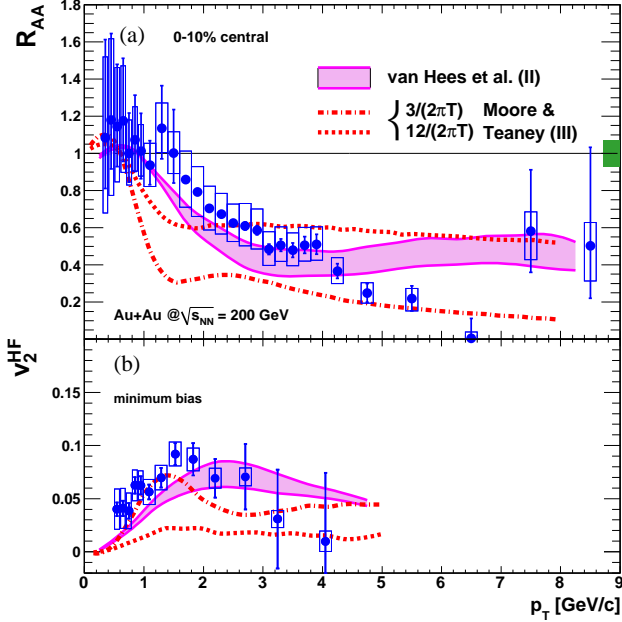


FIG. 40: (Color online) Comparison of Langevin-based models from [74–76] to the heavy flavor electron R_{AuAu} for 0–10% centrality and v_2 for minimum-bias collisions.

charm and beauty hadrons in p+p and Au+Au collisions. As it has been observed for the light hadrons [79], one could expect a modification of the charm hadron chemical composition in the most central Au+Au collisions. In particular, an enhancement of the Λ_c production has been predicted [80]. A Λ_c enhancement leads naturally to a nonphotonic electron R_{AA} smaller than one due to a smaller semileptonic decay branching ratio of charm baryons compared to charm mesons and also due to a softer spectrum of the electrons from the charm baryon

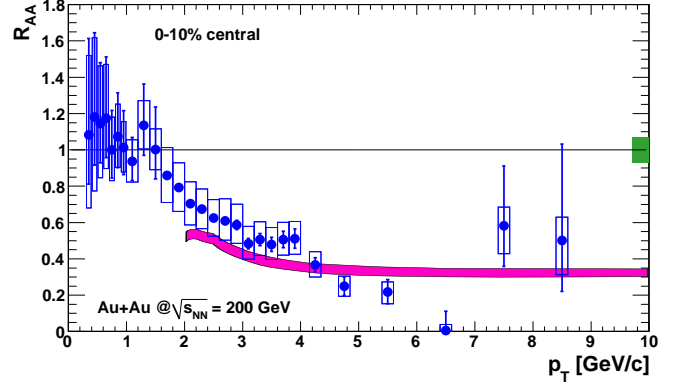


FIG. 41: (Color online) R_{AuAu} in 0–10% centrality class compared with a collisional dissociation model [78] (band) in Au+Au collisions.

decay. A R_{AA} of about 0.65 for electrons from charm hadron decay is predicted when a charm baryon to charm meson ratio in central Au+Au collisions close to one is assumed [81].

Gossiaux and Aichelin [82–84] calculated the R_{AA} from collisional energy loss in pQCD using a running coupling constant and replacing the Debye mass with a hard thermal loop calculation. The model finds a value close to the experimental R_{AA} for all centralities, while leaving room for a possible radiative contribution as well. Figure 42 shows the R_{AA} as a function of p_T and centrality from this model.

Kharzeev has predicted a universal bound on the energy of a parton escaping strongly coupled matter [85] in $\mathcal{N} = 4$ SUSY Yang-Mills theory, under some assumptions about the evolution of gauge fields in heavy-ion collisions. In the model, the R_{AA} at high p_T is given by a constant times $N_{\text{part}}/N_{\text{coll}}$ with the constant universal for all particle species.

B. Theory comparison (v_2)

The azimuthal anisotropy of heavy quarks gives information about the density of the colliding system. The collectivity of heavy quarks during the early stage of the collision is expected to be developed via the strong interaction inside the quark gluon plasma, which will be seen in the relatively low p_T region. On the other hand, the suppression and/or modification of the high p_T yield, which is caused by the interaction of the heavy quarks with the overlapped almond shape geometry and path length of the heavy quark inside the plasma, could also create an azimuthal anisotropy at higher p_T . Therefore, when considering the p_T dependence of the anisotropy parameter v_2 , it is important to understand these different effects as well as the relative fraction of bottom quarks compared to charm quarks. Several model predictions are compared to the experimental data in this

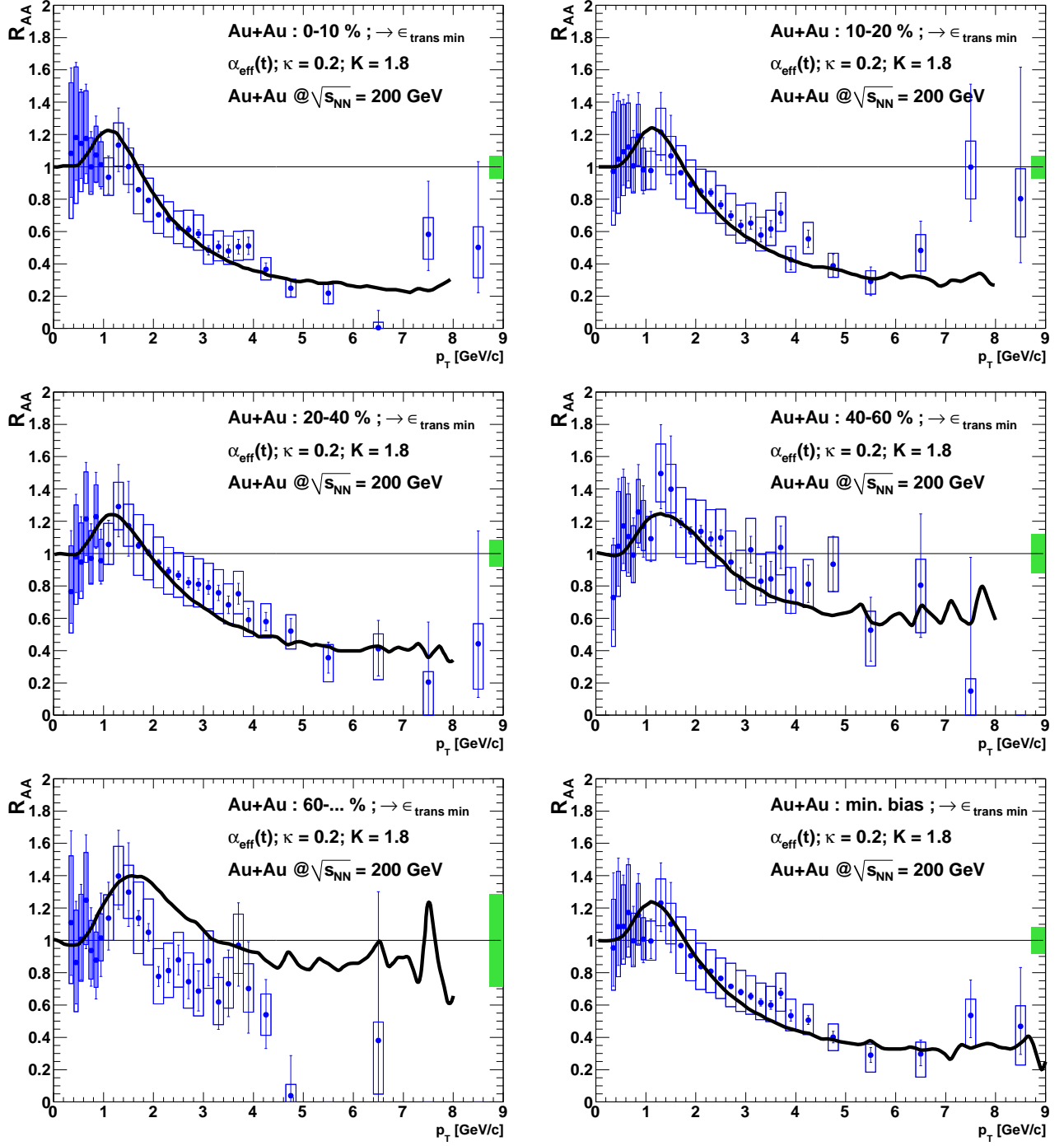


FIG. 42: (Color online) R_{AuAu} vs centrality and p_T from Gossiaux and Aichelin [82–84].

section.

Figure 43 shows a comparison of two different model calculations to experimental data for the nonphotonic electron v_2 from minimum-bias collisions. The models shown in this figure were also discussed in the previous section as they are also used to calculate R_{AA} . In the model of Moore and Teaney [74], a Langevin-based heavy quark transport calculation is performed in a perturba-

tive quark gluon plasma with hydrodynamic simulation. Two different calculations with two different assumptions for the value of the diffusion coefficient are shown as a solid curve for $D = 3/(2\pi T)$, which agrees with experimental data, and as a dashed curve for $D = 12/(2\pi T)$. In the model of Armesto et al. [71], the effect of heavy quark energy loss for $p_T > 2$ GeV/c is considered without any collective effect in the lower p_T region, which gives a

lower limit on v_2 at high p_T given by the energy loss and the geometry of the almond shape, with two values of the transport coefficient \hat{q} for the green solid curve $\hat{q} = 14 \text{ GeV}^2/\text{fm}$ and for the green dashed curve $\hat{q} = 4 \text{ GeV}^2/\text{fm}$.

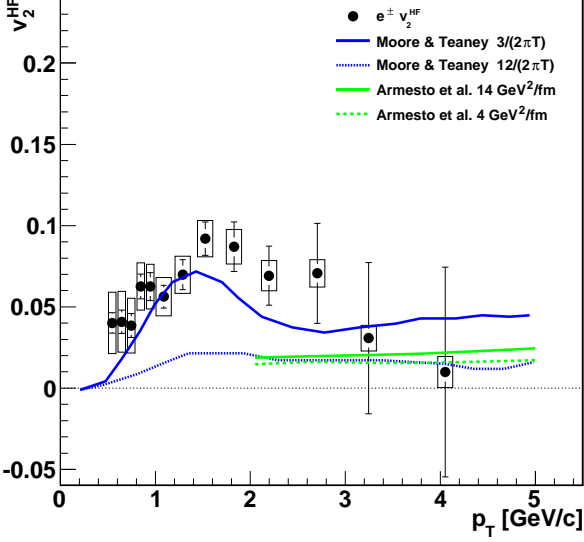


FIG. 43: (Color online) Comparison of experimental v_2 data with the models of Moore and Teaney [74] and Armesto et al. [71].

Figure 44 shows a set of comparisons of three model calculations with the experimental data. The model of Greco et al. [86] is based on the quark coalescence model with light and charm quarks v_2 , where the light quark v_2 is estimated from the measured meson v_2 and the same amount of radial flow is assumed for all quark species with the same saturating v_2 for the charm quark as for the light quark. The calculated electron v_2 from the D meson is labeled as “Greco et al. c flow”. On the other hand, the line labeled as “Greco et al. no c flow” assumes zero v_2 for the charm quark, and the predicted v_2 is given only by the light quark v_2 via the quark coalescence mechanism. The model of Zhang et al. [87] is a hybrid model starting with HIJING as an initial condition, followed by a parton cascade, and then a hadron cascade after a hadronization with a quark coalescence model. This is based on a multiphase transport model including rescattering of the charm quark with the other partons. The line labeled “Zhang et al. 10 mb” is the resulting electron v_2 from D-meson decay with the charm quark parton-scattering cross section of $\sigma_p = 10 \text{ mb}$, while the line labeled “Zhang et al. 3 mb” corresponds to $\sigma_p = 3 \text{ mb}$. The model of van Hees et al. [75, 76], discussed in the previous section as it is also used to calculate R_{AA} , includes resonant interactions in a strongly interacting QGP and parton coalescence of both charm and bottom quarks. The band with shows the results of this model, while the result with only charm quarks is shown as the

line labeled “van Hees et al. c only”, and the result without resonances is shown as the line labeled “van Hees et al. no reso”. Both the resonance and the coalescence are responsible for the large magnitude of the measured electron v_2 in the low p_T region, while the reduction or flattening of v_2 at high p_T requires the bottom quark contribution.

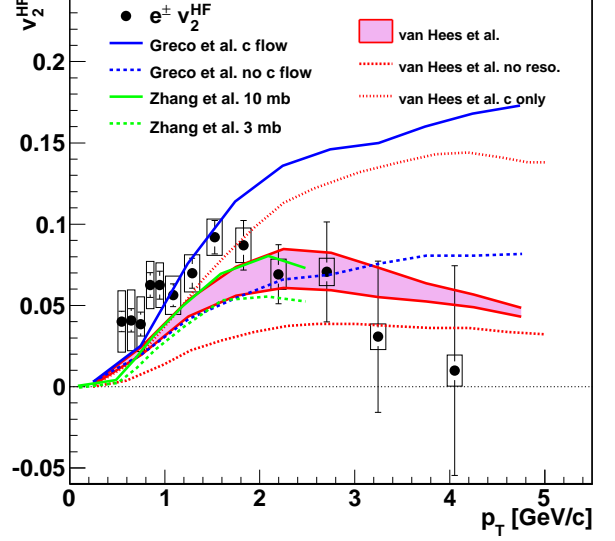


FIG. 44: (Color online) Theory comparison of experimental v_2 data with the models of Greco et al. [86], Zhang et al. [87], and van Hees et al. [75, 76].

A pQCD-based elastic scattering model [82–84] with running coupling constant is used to calculate v_2 as well as the R_{AA} . The minimum-bias v_2 from this model is shown in Fig. 45. The v_2 is very sensitive to the interaction time, and a later freeze-out can produce a larger v_2 [82].

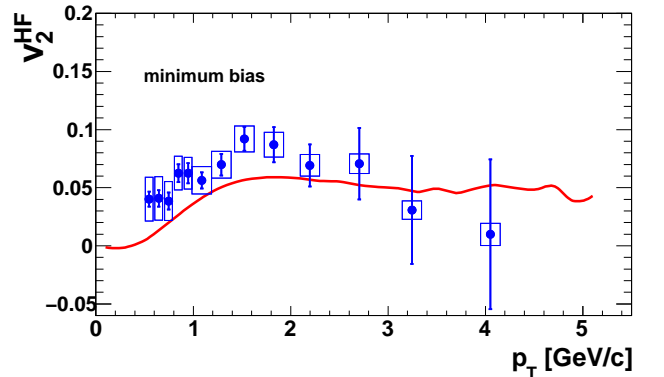


FIG. 45: (Color online) Minimum-bias v_2 compared with a model calculation from Gossiaux and Aichelin [82–84].

Various models discussed in this section indicate strong interaction of heavy quarks with the high energy density

matter created in heavy-ion collisions at RHIC and also support quark coalescence (recombination) as a dominant hadronization mechanism, which would mean that the heavy quarks are also a part of the quark gluon plasma. Therefore the sizable event anisotropy parameter v_2 of electrons from heavy quarks measured at low p_T should be related with the collectivity of the heavy quark. The reduction or flattening of v_2 in the high p_T region would have to be caused by the change of the dominant mechanism from the collectivity of the heavy quark to the energy loss of the heavy quark, especially when most of the heavy quarks are charm quarks. However the reduction can also be qualitatively understood by an increase of the relative fraction of bottom quarks as a function of p_T and a smaller magnitude of event anisotropy for the heavier quark.

In order to determine the charm quark v_2 , the measured nonphotonic electron v_2 is compared to that expected from coalescent production of D mesons. Chi square values are calculated for different combinations of light and charm quark v_2 values. The p_T range is restricted to below 2 GeV/c in order to be sensitive to only the charm quark, and not to the bottom quark. The quark coalescence is assumed to occur at similar velocities, therefore it gives the momentum ratio of about 1/6 for light/charm quarks, which is given by the ratio of the effective mass of the quarks. A common shape of v_2 vs p_T for both light and charm quarks is assumed, where this shape is determined by the light hadron v_2 . For given v_2 values of light and charm quarks, π , K and proton v_2 's and electron v_2 from D mesons are calculated, then the total chi-square sum is calculated and plotted in Fig. 46 as a function of the light quark v_2 (horizontal axis) and charm quark v_2 (vertical axis). Both the horizontal and vertical axes are normalized to the measured light quark v_2 , so that unity corresponds to the light quark v_2 . The chi-square minimum lies at about equal light quark and heavy quark v_2 magnitudes, although the relative error in v_2 is much larger for the charm quark than for the light quark. This indicates a common quark collectivity in the quark gluon plasma phase.

C. Viscosity to entropy ratio η/s

The ratio of shear viscosity η to entropy density s is a key parameter that determines the damping rate in a relativistic system. At temperature T , characteristic damping times τ are of order η/sT [88].

While the apparent success of ideal hydrodynamics in describing particle spectra and elliptic flow patterns at RHIC would imply a vanishing value of η , straightforward arguments based on the uncertainty principle suggest that the viscosity for any thermal system must be non-zero [89]. This observation was extended by Kovtun, Son and Starinets (KSS) [90], who demonstrated that conformal field theories with gravity duals have a ratio of viscosity η to entropy density s of $1/4\pi$ (in natural

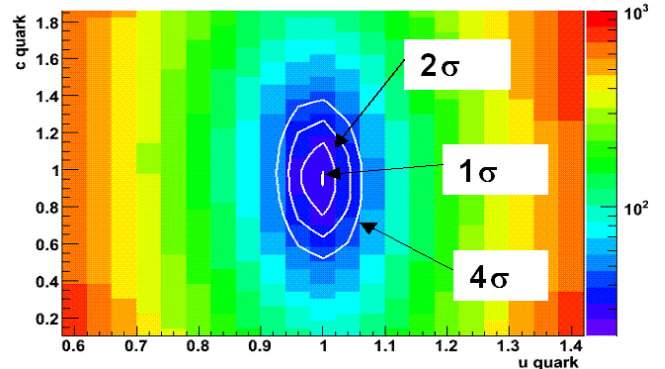


FIG. 46: (Color online) χ^2 map as a function of the light quark v_2 (horizontal axis) and charm quark v_2 (vertical axis), each divided by the measured light quark v_2 .

units). KSS conjectured that this value is a bound for any relativistic thermal field theory, that is, $\eta/s \geq 1/4\pi$.

The results presented in Section IV for $R_{\text{AuAu}}(p_T^e)$ and $v_2(p_T^e)$ show that heavy quarks lose energy in the medium, while acquiring a substantial component of the medium's collective flow. Both of these effects may be regarded as the damping of the initial non-equilibrium dynamics of the "external" heavy quark by the medium. The simultaneous description of these phenomena by the model of van Hees et al. provides a straightforward, albeit indirect, method to infer the ratio of viscosity to entropy density. The resonance model employed in Ref. [75] leads to an estimate for the heavy quark spatial diffusion constant $D_s \sim (4-6)/2\pi T$ for temperatures T in the range $0.2 \text{ GeV} < T < 0.4 \text{ GeV}$ (see also Figure 23 of Ref. [91]). Moore and Teaney [74] perform a perturbative calculation of this quantity, and find that for a medium with three light flavors the ratio of D_s to the hydrodynamic diffusion constant $\eta/(\epsilon+p)$ for the bulk (ϵ is the energy density and p the pressure of the medium) has a value of ~ 6 roughly independent of the coupling strength $\sim m_D/T$, where m_D is the Debye mass. They argue that the weak variation with coupling strength is to be expected in this *ratio* of transport coefficients, making it plausible that it remains near 6 in the strongly-coupled regime. In this case, and approximating the thermodynamic identity $\epsilon + p = Ts + \mu_B n_B \approx Ts$ appropriate for the baryon-free central region, one readily finds $\eta/s \sim (1.33 - 2)/4\pi$, that is, a value near the KSS bound and consistent with other estimates for the RHIC plasma based on flow [92, 93], fluctuations [94], entropy production [95] and detailed hydrodynamic calculations [96, 97]. It should be noted that these various estimates are based on observables of the "bulk" medium, in flavor channels dominated by u , d and s quarks, while the result presented here relies explicitly on the coupling of heavy flavor to the medium. The consistency of the derived value of η/s supports both the strong coupling of heavy flavor to the medium and the low value of η/s for the RHIC

plasma.

VI. SUMMARY AND CONCLUSIONS

This article has detailed the measurement of the yield of single electrons from semileptonic decays of heavy flavor mesons at midrapidity in $p+p$ and Au+Au collisions at $\sqrt{s_{NN}} = 200$ GeV, as well as the azimuthal anisotropy parameter v_2 of such electrons in Au+Au collisions. The unexpectedly large suppression of heavy flavor electrons in Au+Au collisions relative to those from $p+p$ collisions and the large v_2 of heavy flavor electrons has generated much theoretical work. In a system as complicated as this medium, confidence from any given model depends on its ability to describe multiple observables simultaneously. The intermediate-mass range dilepton measurement [98] at PHENIX is dominated by correlated decays of charm mesons which are not included in the calculations of any published model. In the coming years, PHENIX will measure the yields and flow of bottom and charm mesons separately, which will further constrain the interpretation of the data.

VII. ACKNOWLEDGEMENTS

We thank the staff of the Collider-Accelerator and Physics Departments at Brookhaven National Laboratory and the staff of the other PHENIX participating institutions for their vital contributions. We acknowledge support from the Office of Nuclear Physics in the Office of Science of the Department of Energy, the National Science Foundation, a sponsored research grant from Renaissance Technologies LLC, Abilene Christian University Research Council, Research Foundation of SUNY, and Dean of the College of Arts and Sciences, Vanderbilt University (USAA), Ministry of Education, Culture, Sports, Science, and Technology and the Japan Society for the Promotion of Science (Japan), Conselho Nacional de Desenvolvimento Científico e Tecnológico and Fundação de Amparo à Pesquisa do Estado de São Paulo (Brazil), Natural Science Foundation of China (People's Republic of China), Ministry of Education, Youth and Sports (Czech Republic), Centre National de la Recherche Scientifique, Commissariat à l'Énergie Atomique, and Institut National de Physique Nucléaire et de Physique des Particules (France), Ministry of Industry, Science and Technologies, Bundesministerium für Bildung und Forschung, Deutscher Akademischer Austausch Dienst, and Alexander von Humboldt Stiftung (Germany), Hungarian National Science Fund, OTKA (Hungary), Department of Atomic Energy (India), Israel Science Foundation (Israel), Korea Research Foundation and Korea Science and Engineering Foundation (Korea), Ministry of Education and Science, Russia Academy of Sciences, Federal Agency of Atomic Energy (Russia), VR and the Wallenberg Foundation (Sweden), the

USA Civilian Research and Development Foundation for the Independent States of the Former Soviet Union, the US-Hungarian Fulbright Foundation for Educational Exchange, and the US-Israel Binational Science Foundation.

APPENDIX: DATA TABLES

Data are presented in this Appendix for the minimum bias events (0–92%) and for each centrality class (0–10%, 10–20%, 20–40%, 40–60%, and 60–92%) for Au+Au collisions at $\sqrt{s_{NN}} = 200$ GeV at midrapidity. Tables X–XII tabulate the differential invariant yield of heavy flavor electrons. Tables XIII–XV give the nuclear modification factor R_{AuAu} of heavy flavor electrons. Table XVII shows v_2 for heavy flavor electrons. Table XVIII gives the differential invariant cross section of heavy flavor electrons.

TABLE X: Differential invariant yield of electrons ($(N_{e^+} + N_{e^-})/2$) from heavy-flavor decays for (upper, minimum bias) 0–92% and (lower) 0–10% centrality classes. The p_T^e is in units of GeV/ c . The yield and corresponding errors are in units of (GeV/ c) $^{-2}$

Centrality	p_T^e	Invariant yield	Stat. error (+)	Stat. error (–)	Sys. error (+)	Sys. error (–)
0–92%	0.30	7.30×10^{-2}	3.01×10^{-3}	2.97×10^{-3}	1.94×10^{-2}	1.91×10^{-2}
	0.50	3.74×10^{-2}	1.29×10^{-3}	1.27×10^{-3}	7.73×10^{-3}	7.63×10^{-3}
	0.60	2.09×10^{-2}	6.55×10^{-4}	6.47×10^{-4}	3.66×10^{-3}	3.61×10^{-3}
	0.70	1.22×10^{-2}	3.86×10^{-4}	3.82×10^{-4}	1.94×10^{-3}	1.92×10^{-3}
	0.80	7.46×10^{-3}	2.32×10^{-4}	2.30×10^{-4}	1.04×10^{-3}	1.03×10^{-3}
	0.80	5.04×10^{-3}	1.54×10^{-4}	1.52×10^{-4}	6.09×10^{-4}	6.03×10^{-4}
	0.90	3.27×10^{-3}	1.06×10^{-4}	1.05×10^{-4}	3.70×10^{-4}	3.67×10^{-4}
	1.10	1.84×10^{-3}	4.74×10^{-5}	4.60×10^{-5}	1.95×10^{-4}	1.90×10^{-4}
	1.30	8.21×10^{-4}	2.04×10^{-5}	1.99×10^{-5}	9.04×10^{-5}	8.81×10^{-5}
	1.50	3.90×10^{-4}	8.81×10^{-6}	8.62×10^{-6}	4.35×10^{-5}	4.26×10^{-5}
	1.70	1.87×10^{-4}	2.56×10^{-6}	2.56×10^{-6}	2.87×10^{-5}	2.87×10^{-5}
	1.90	9.49×10^{-5}	1.35×10^{-6}	1.35×10^{-6}	1.40×10^{-5}	1.40×10^{-5}
	2.10	5.05×10^{-5}	7.71×10^{-7}	7.71×10^{-7}	7.18×10^{-6}	7.18×10^{-6}
	2.30	2.91×10^{-5}	4.83×10^{-7}	4.83×10^{-7}	3.90×10^{-6}	3.90×10^{-6}
	2.50	1.71×10^{-5}	3.12×10^{-7}	3.12×10^{-7}	2.18×10^{-6}	2.18×10^{-6}
	2.70	9.98×10^{-6}	2.12×10^{-7}	2.12×10^{-7}	1.26×10^{-6}	1.26×10^{-6}
	2.90	6.07×10^{-6}	1.50×10^{-7}	1.50×10^{-7}	7.54×10^{-7}	7.54×10^{-7}
	3.10	3.87×10^{-6}	1.11×10^{-7}	1.11×10^{-7}	4.67×10^{-7}	4.67×10^{-7}
	3.30	2.45×10^{-6}	8.27×10^{-8}	8.27×10^{-8}	2.93×10^{-7}	2.93×10^{-7}
	3.50	1.61×10^{-6}	6.39×10^{-8}	6.39×10^{-8}	1.91×10^{-7}	1.91×10^{-7}
3.70	1.25×10^{-6}	5.23×10^{-8}	5.23×10^{-8}	1.38×10^{-7}	1.38×10^{-7}	
3.90	7.05×10^{-7}	3.94×10^{-8}	3.90×10^{-8}	8.40×10^{-8}	8.40×10^{-8}	
4.20	3.81×10^{-7}	1.71×10^{-8}	1.71×10^{-8}	4.38×10^{-8}	4.38×10^{-8}	
4.80	1.48×10^{-7}	1.03×10^{-8}	1.02×10^{-8}	1.76×10^{-8}	1.76×10^{-8}	
5.50	4.04×10^{-8}	4.45×10^{-9}	4.37×10^{-9}	5.61×10^{-9}	5.61×10^{-9}	
6.50	1.18×10^{-8}	2.22×10^{-9}	2.15×10^{-9}	1.61×10^{-9}	1.61×10^{-9}	
7.50	5.84×10^{-9}	1.59×10^{-9}	1.53×10^{-9}	6.93×10^{-10}	6.93×10^{-10}	
8.50	1.93×10^{-9}	1.02×10^{-9}	6.87×10^{-10}	3.37×10^{-10}	3.37×10^{-10}	
0–10%	0.30	3.35×10^{-1}	1.63×10^{-2}	1.61×10^{-2}	6.70×10^{-2}	6.60×10^{-2}
	0.50	1.62×10^{-1}	7.05×10^{-3}	6.95×10^{-3}	2.73×10^{-2}	2.69×10^{-2}
	0.60	8.75×10^{-2}	3.59×10^{-3}	3.55×10^{-3}	1.30×10^{-2}	1.28×10^{-2}
	0.70	4.83×10^{-2}	2.15×10^{-3}	2.12×10^{-3}	6.87×10^{-3}	6.79×10^{-3}
	0.80	2.96×10^{-2}	1.31×10^{-3}	1.30×10^{-3}	3.74×10^{-3}	3.70×10^{-3}
	0.80	1.83×10^{-2}	8.65×10^{-4}	8.57×10^{-4}	2.17×10^{-3}	2.14×10^{-3}
	0.90	1.29×10^{-2}	6.13×10^{-4}	6.07×10^{-4}	1.37×10^{-3}	1.36×10^{-3}
	1.10	6.78×10^{-3}	2.74×10^{-4}	2.66×10^{-4}	7.05×10^{-4}	6.83×10^{-4}
	1.30	3.25×10^{-3}	7.08×10^{-5}	6.89×10^{-5}	4.01×10^{-4}	3.90×10^{-4}
	1.50	1.50×10^{-3}	3.09×10^{-5}	3.02×10^{-5}	1.91×10^{-4}	1.86×10^{-4}
	1.70	6.62×10^{-4}	1.05×10^{-5}	1.05×10^{-5}	9.80×10^{-5}	9.80×10^{-5}
	1.90	3.32×10^{-4}	5.84×10^{-6}	5.84×10^{-6}	4.68×10^{-5}	4.68×10^{-5}
	2.10	1.70×10^{-4}	3.51×10^{-6}	3.51×10^{-6}	2.34×10^{-5}	2.34×10^{-5}
	2.30	9.52×10^{-5}	2.30×10^{-6}	2.30×10^{-6}	1.25×10^{-5}	1.25×10^{-5}
	2.5	5.45×10^{-5}	1.55×10^{-6}	1.55×10^{-6}	6.89×10^{-6}	6.89×10^{-6}
	2.7	3.32×10^{-5}	1.11×10^{-6}	1.11×10^{-6}	4.06×10^{-6}	4.06×10^{-6}
	2.9	2.03×10^{-5}	8.02×10^{-7}	8.02×10^{-7}	2.43×10^{-6}	2.43×10^{-6}
	3.1	1.11×10^{-5}	5.84×10^{-7}	5.79×10^{-7}	1.38×10^{-6}	1.38×10^{-6}
	3.3	7.73×10^{-6}	4.53×10^{-7}	4.48×10^{-7}	9.14×10^{-7}	9.14×10^{-7}
	3.5	4.96×10^{-6}	3.52×10^{-7}	3.48×10^{-7}	5.87×10^{-7}	5.87×10^{-7}
3.7	3.65×10^{-6}	2.82×10^{-7}	2.78×10^{-7}	4.08×10^{-7}	4.08×10^{-7}	
3.9	2.56×10^{-6}	2.32×10^{-7}	2.28×10^{-7}	2.84×10^{-7}	2.84×10^{-7}	
4.2	1.08×10^{-6}	9.32×10^{-8}	9.19×10^{-8}	1.28×10^{-7}	1.28×10^{-7}	
4.8	3.76×10^{-7}	5.51×10^{-8}	5.39×10^{-8}	4.88×10^{-8}	4.88×10^{-8}	
5.5	1.22×10^{-7}	2.50×10^{-8}	2.41×10^{-8}	1.72×10^{-8}	1.72×10^{-8}	
6.5	1.21×10^{-8}	1.11×10^{-8}	8.26×10^{-9}	3.20×10^{-9}	3.20×10^{-9}	
7.5	2.38×10^{-8}	1.15×10^{-8}	7.78×10^{-9}	2.66×10^{-9}	2.66×10^{-9}	
8.5	7.78×10^{-9}	6.97×10^{-9}	3.70×10^{-9}	1.25×10^{-9}	1.25×10^{-9}	

TABLE XI: Differential invariant yield of electrons $((N_{e^+} + N_{e^-})/2)$ from heavy-flavor decays for (upper) 10–20% and (lower) 20–40% centrality classes. The p_T^e is in units of GeV/c. The yield and corresponding errors are in units of $(\text{GeV}/c)^{-2}$

Centrality	p_T^e	Invariant yield	Stat. error (+)	Stat. error (-)	Sys. error (+)	Sys. error (-)
10–20%	0.3	1.90×10^{-1}	1.11×10^{-2}	1.09×10^{-2}	4.48×10^{-2}	4.42×10^{-2}
	0.5	9.11×10^{-2}	4.81×10^{-3}	4.75×10^{-3}	1.79×10^{-2}	1.77×10^{-2}
	0.6	5.29×10^{-2}	2.52×10^{-3}	2.49×10^{-3}	8.57×10^{-3}	8.48×10^{-3}
	0.7	2.92×10^{-2}	1.53×10^{-3}	1.51×10^{-3}	4.55×10^{-3}	4.50×10^{-3}
	0.8	1.88×10^{-2}	9.51×10^{-4}	9.42×10^{-4}	2.47×10^{-3}	2.45×10^{-3}
	0.8	1.29×10^{-2}	6.42×10^{-4}	6.36×10^{-4}	1.47×10^{-3}	1.46×10^{-3}
	0.9	7.93×10^{-3}	4.50×10^{-4}	4.46×10^{-4}	8.77×10^{-4}	8.70×10^{-4}
	1.1	4.47×10^{-3}	2.07×10^{-4}	2.01×10^{-4}	4.69×10^{-4}	4.55×10^{-4}
	1.3	2.20×10^{-3}	5.03×10^{-5}	4.90×10^{-5}	2.50×10^{-4}	2.44×10^{-4}
	1.5	1.01×10^{-3}	2.24×10^{-5}	2.19×10^{-5}	1.16×10^{-4}	1.13×10^{-4}
	1.7	4.69×10^{-4}	7.98×10^{-6}	7.98×10^{-6}	6.73×10^{-5}	6.73×10^{-5}
	1.9	2.41×10^{-4}	4.54×10^{-6}	4.54×10^{-6}	3.27×10^{-5}	3.27×10^{-5}
	2.10	1.28×10^{-4}	2.81×10^{-6}	2.81×10^{-6}	1.67×10^{-5}	1.67×10^{-5}
	2.3	7.54×10^{-5}	1.89×10^{-6}	1.89×10^{-6}	9.24×10^{-6}	9.24×10^{-6}
	2.5	4.18×10^{-5}	1.27×10^{-6}	1.27×10^{-6}	5.04×10^{-6}	5.04×10^{-6}
	2.7	2.38×10^{-5}	8.92×10^{-7}	8.92×10^{-7}	2.86×10^{-6}	2.86×10^{-6}
	2.9	1.40×10^{-5}	6.44×10^{-7}	6.44×10^{-7}	1.66×10^{-6}	1.66×10^{-6}
	3.1	9.37×10^{-6}	4.96×10^{-7}	4.91×10^{-7}	1.06×10^{-6}	1.06×10^{-6}
	3.3	5.59×10^{-6}	3.69×10^{-7}	3.65×10^{-7}	6.41×10^{-7}	6.41×10^{-7}
	3.5	3.98×10^{-6}	2.94×10^{-7}	2.90×10^{-7}	4.39×10^{-7}	4.39×10^{-7}
3.7	3.14×10^{-6}	2.48×10^{-7}	2.44×10^{-7}	3.25×10^{-7}	3.25×10^{-7}	
3.9	1.40×10^{-6}	1.71×10^{-7}	1.68×10^{-7}	1.68×10^{-7}	1.68×10^{-7}	
4.2	9.77×10^{-7}	8.13×10^{-8}	8.01×10^{-8}	1.05×10^{-7}	1.05×10^{-7}	
4.8	3.42×10^{-7}	4.82×10^{-8}	4.70×10^{-8}	3.92×10^{-8}	3.92×10^{-8}	
5.5	9.71×10^{-8}	2.10×10^{-8}	2.02×10^{-8}	1.26×10^{-8}	1.26×10^{-8}	
6.5	4.00×10^{-8}	1.20×10^{-8}	1.13×10^{-8}	4.53×10^{-9}	4.53×10^{-9}	
7.5	2.45×10^{-8}	1.13×10^{-8}	7.40×10^{-9}	2.38×10^{-9}	2.38×10^{-9}	
8.5	7.54×10^{-9}	6.78×10^{-9}	3.30×10^{-9}	1.07×10^{-9}	1.07×10^{-9}	
20–40%	0.3	7.35×10^{-2}	5.15×10^{-3}	5.09×10^{-3}	2.48×10^{-2}	2.45×10^{-2}
	0.5	4.19×10^{-2}	2.30×10^{-3}	2.28×10^{-3}	9.85×10^{-3}	9.74×10^{-3}
	0.6	2.25×10^{-2}	1.20×10^{-3}	1.19×10^{-3}	4.66×10^{-3}	4.61×10^{-3}
	0.7	1.55×10^{-2}	7.55×10^{-4}	7.47×10^{-4}	2.50×10^{-3}	2.48×10^{-3}
	0.8	8.93×10^{-3}	4.63×10^{-4}	4.59×10^{-4}	1.33×10^{-3}	1.31×10^{-3}
	0.8	6.50×10^{-3}	3.16×10^{-4}	3.13×10^{-4}	7.83×10^{-4}	7.76×10^{-4}
	0.9	3.79×10^{-3}	2.21×10^{-4}	2.19×10^{-4}	4.66×10^{-4}	4.63×10^{-4}
	1.1	2.38×10^{-3}	1.03×10^{-4}	9.98×10^{-5}	2.51×10^{-4}	2.44×10^{-4}
	1.3	1.15×10^{-3}	2.77×10^{-5}	2.70×10^{-5}	1.26×10^{-4}	1.23×10^{-4}
	1.5	5.45×10^{-4}	1.24×10^{-5}	1.21×10^{-5}	6.07×10^{-5}	5.95×10^{-5}
	1.7	2.56×10^{-4}	4.27×10^{-6}	4.27×10^{-6}	3.76×10^{-5}	3.76×10^{-5}
	1.9	1.31×10^{-4}	2.42×10^{-6}	2.42×10^{-6}	1.85×10^{-5}	1.85×10^{-5}
	2.10	7.12×10^{-5}	1.49×10^{-6}	1.49×10^{-6}	9.60×10^{-6}	9.60×10^{-6}
	2.3	4.00×10^{-5}	9.78×10^{-7}	9.78×10^{-7}	5.15×10^{-6}	5.15×10^{-6}
	2.5	2.35×10^{-5}	6.70×10^{-7}	6.70×10^{-7}	2.93×10^{-6}	2.93×10^{-6}
	2.7	1.41×10^{-5}	4.73×10^{-7}	4.73×10^{-7}	1.70×10^{-6}	1.70×10^{-6}
	2.9	8.86×10^{-6}	3.50×10^{-7}	3.50×10^{-7}	1.03×10^{-6}	1.03×10^{-6}
	3.1	5.62×10^{-6}	2.64×10^{-7}	2.64×10^{-7}	6.43×10^{-7}	6.43×10^{-7}
	3.3	3.63×10^{-6}	2.02×10^{-7}	2.00×10^{-7}	4.09×10^{-7}	4.09×10^{-7}
	3.5	2.25×10^{-6}	1.54×10^{-7}	1.52×10^{-7}	2.54×10^{-7}	2.54×10^{-7}
3.7	1.69×10^{-6}	1.26×10^{-7}	1.25×10^{-7}	1.80×10^{-7}	1.80×10^{-7}	
3.9	9.65×10^{-7}	9.42×10^{-8}	9.26×10^{-8}	1.10×10^{-7}	1.10×10^{-7}	
4.2	5.37×10^{-7}	4.21×10^{-8}	4.15×10^{-8}	5.84×10^{-8}	5.84×10^{-8}	
4.8	2.27×10^{-7}	2.57×10^{-8}	2.52×10^{-8}	2.47×10^{-8}	2.47×10^{-8}	
5.5	6.08×10^{-8}	1.11×10^{-8}	1.07×10^{-8}	7.65×10^{-9}	7.65×10^{-9}	
6.5	1.91×10^{-8}	5.75×10^{-9}	5.45×10^{-9}	2.28×10^{-9}	2.28×10^{-9}	
7.5	3.95×10^{-9}	4.02×10^{-9}	2.32×10^{-9}	5.98×10^{-10}	5.98×10^{-10}	
8.5	2.39×10^{-9}	2.85×10^{-9}	1.36×10^{-9}	3.98×10^{-10}	3.98×10^{-10}	

TABLE XII: Differential invariant yield of electrons ($(N_{e^+} + N_{e^-})/2$) from heavy-flavor decays for (upper) 40–60% and (lower) 60–92% centrality classes. The p_T^e is in units of GeV/c. The yield and corresponding errors are in units of $(\text{GeV}/c)^{-2}$

Centrality	p_T^e	Invariant yield	Stat. error (+)	Stat. error (-)	Sys. error (+)	Sys. error (-)
40–60%	0.3	2.13×10^{-2}	2.66×10^{-3}	2.63×10^{-3}	9.42×10^{-3}	9.31×10^{-3}
	0.5	1.36×10^{-2}	1.20×10^{-3}	1.18×10^{-3}	3.69×10^{-3}	3.65×10^{-3}
	0.6	8.48×10^{-3}	6.44×10^{-4}	6.38×10^{-4}	1.72×10^{-3}	1.70×10^{-3}
	0.7	4.30×10^{-3}	4.00×10^{-4}	3.96×10^{-4}	9.02×10^{-4}	8.94×10^{-4}
	0.8	2.78×10^{-3}	2.51×10^{-4}	2.49×10^{-4}	4.73×10^{-4}	4.69×10^{-4}
	0.8	2.03×10^{-3}	1.71×10^{-4}	1.70×10^{-4}	2.74×10^{-4}	2.72×10^{-4}
	0.9	1.41×10^{-3}	1.23×10^{-4}	1.22×10^{-4}	1.68×10^{-4}	1.67×10^{-4}
	1.1	7.48×10^{-4}	5.70×10^{-5}	5.55×10^{-5}	8.65×10^{-5}	8.42×10^{-5}
	1.3	4.05×10^{-4}	1.05×10^{-5}	1.03×10^{-5}	4.23×10^{-5}	4.13×10^{-5}
	1.5	1.98×10^{-4}	5.00×10^{-6}	4.90×10^{-6}	2.10×10^{-5}	2.06×10^{-5}
	1.7	8.78×10^{-5}	2.01×10^{-6}	2.01×10^{-6}	1.33×10^{-5}	1.33×10^{-5}
	1.9	4.64×10^{-5}	1.22×10^{-6}	1.22×10^{-6}	6.67×10^{-6}	6.67×10^{-6}
	2.10	2.59×10^{-5}	7.91×10^{-7}	7.91×10^{-7}	3.54×10^{-6}	3.54×10^{-6}
	2.3	1.50×10^{-5}	5.45×10^{-7}	5.45×10^{-7}	1.96×10^{-6}	1.96×10^{-6}
	2.5	9.10×10^{-6}	3.85×10^{-7}	3.85×10^{-7}	1.13×10^{-6}	1.13×10^{-6}
	2.7	5.05×10^{-6}	2.71×10^{-7}	2.71×10^{-7}	6.37×10^{-7}	6.37×10^{-7}
	2.9	2.90×10^{-6}	1.98×10^{-7}	1.96×10^{-7}	3.70×10^{-7}	3.70×10^{-7}
	3.1	2.27×10^{-6}	1.60×10^{-7}	1.58×10^{-7}	2.54×10^{-7}	2.54×10^{-7}
	3.3	1.25×10^{-6}	1.18×10^{-7}	1.16×10^{-7}	1.50×10^{-7}	1.50×10^{-7}
	3.5	8.68×10^{-7}	9.34×10^{-8}	9.18×10^{-8}	9.93×10^{-8}	9.93×10^{-8}
3.7	7.14×10^{-7}	7.86×10^{-8}	7.70×10^{-8}	7.43×10^{-8}	7.43×10^{-8}	
3.9	3.85×10^{-7}	5.82×10^{-8}	5.67×10^{-8}	4.40×10^{-8}	4.40×10^{-8}	
4.2	2.30×10^{-7}	2.62×10^{-8}	2.57×10^{-8}	2.41×10^{-8}	2.41×10^{-8}	
4.8	1.19×10^{-7}	1.75×10^{-8}	1.71×10^{-8}	1.17×10^{-8}	1.17×10^{-8}	
5.5	2.70×10^{-8}	7.04×10^{-9}	6.71×10^{-9}	3.21×10^{-9}	3.21×10^{-9}	
6.5	1.03×10^{-8}	4.37×10^{-9}	3.21×10^{-9}	1.08×10^{-9}	1.08×10^{-9}	
7.5	1.23×10^{-9}	2.74×10^{-9}	1.13×10^{-9}	2.04×10^{-10}	2.04×10^{-10}	
60–92%	0.3	5.28×10^{-3}	8.56×10^{-4}	8.47×10^{-4}	2.16×10^{-3}	2.14×10^{-3}
	0.5	1.83×10^{-3}	3.68×10^{-4}	3.65×10^{-4}	8.06×10^{-4}	7.97×10^{-4}
	0.6	1.18×10^{-3}	2.01×10^{-4}	1.99×10^{-4}	3.72×10^{-4}	3.69×10^{-4}
	0.7	7.89×10^{-4}	1.26×10^{-4}	1.25×10^{-4}	1.93×10^{-4}	1.91×10^{-4}
	0.8	4.27×10^{-4}	7.87×10^{-5}	7.81×10^{-5}	9.85×10^{-5}	9.77×10^{-5}
	0.8	2.30×10^{-4}	5.28×10^{-5}	5.24×10^{-5}	5.39×10^{-5}	5.34×10^{-5}
	0.9	1.99×10^{-4}	3.81×10^{-5}	3.78×10^{-5}	3.29×10^{-5}	3.27×10^{-5}
	1.1	1.27×10^{-4}	1.78×10^{-5}	1.74×10^{-5}	1.74×10^{-5}	1.69×10^{-5}
	1.3	6.15×10^{-5}	2.08×10^{-6}	2.03×10^{-6}	1.04×10^{-5}	1.01×10^{-5}
	1.5	2.99×10^{-5}	1.08×10^{-6}	1.06×10^{-6}	5.21×10^{-6}	5.10×10^{-6}
	1.7	1.39×10^{-5}	5.43×10^{-7}	5.43×10^{-7}	2.27×10^{-6}	2.27×10^{-6}
	1.9	7.09×10^{-6}	3.43×10^{-7}	3.43×10^{-7}	1.14×10^{-6}	1.14×10^{-6}
	2.10	3.08×10^{-6}	2.18×10^{-7}	2.18×10^{-7}	5.54×10^{-7}	5.54×10^{-7}
	2.3	1.91×10^{-6}	1.57×10^{-7}	1.56×10^{-7}	3.16×10^{-7}	3.16×10^{-7}
	2.5	1.25×10^{-6}	1.15×10^{-7}	1.14×10^{-7}	1.89×10^{-7}	1.89×10^{-7}
	2.7	6.77×10^{-7}	8.19×10^{-8}	8.06×10^{-8}	1.08×10^{-7}	1.08×10^{-7}
	2.9	4.09×10^{-7}	6.08×10^{-8}	5.97×10^{-8}	6.46×10^{-8}	6.46×10^{-8}
	3.1	3.27×10^{-7}	4.95×10^{-8}	4.84×10^{-8}	4.40×10^{-8}	4.40×10^{-8}
	3.3	1.68×10^{-7}	3.62×10^{-8}	3.52×10^{-8}	2.58×10^{-8}	2.58×10^{-8}
	3.5	1.30×10^{-7}	2.94×10^{-8}	2.84×10^{-8}	1.78×10^{-8}	1.78×10^{-8}
3.7	1.12×10^{-7}	2.52×10^{-8}	2.43×10^{-8}	1.33×10^{-8}	1.33×10^{-8}	
3.9	6.20×10^{-8}	1.92×10^{-8}	1.84×10^{-8}	8.08×10^{-9}	8.08×10^{-9}	
4.2	2.90×10^{-8}	7.93×10^{-9}	7.63×10^{-9}	3.82×10^{-9}	3.82×10^{-9}	
4.8	5.34×10^{-9}	4.10×10^{-9}	3.84×10^{-9}	1.14×10^{-9}	1.14×10^{-9}	
5.5	1.29×10^{-9}	2.17×10^{-9}	1.37×10^{-9}	3.59×10^{-10}	3.59×10^{-10}	
6.5	1.12×10^{-9}	1.48×10^{-9}	7.82×10^{-10}	1.51×10^{-10}	1.51×10^{-10}	

TABLE XIII: $R_{\text{AuAu}}(p_T^c)$ for (upper, minimum bias) 0–92% and (lower) 0–10% centrality classes.

Centrality	p_T^c	R_{AuAu}	Stat. error (+)	Stat. error (–)	Sys. error (+)	Sys. error (–)
0–92%	0.3	8.74×10^{-1}	4.27×10^{-1}	2.18×10^{-1}	3.19×10^{-1}	2.89×10^{-1}
	0.5	$1.01 \times 10^{+0}$	3.96×10^{-1}	2.24×10^{-1}	3.43×10^{-1}	3.15×10^{-1}
	0.6	$1.01 \times 10^{+0}$	2.96×10^{-1}	1.89×10^{-1}	2.65×10^{-1}	2.46×10^{-1}
	0.7	$1.10 \times 10^{+0}$	3.12×10^{-1}	2.01×10^{-1}	2.64×10^{-1}	2.46×10^{-1}
	0.8	9.34×10^{-1}	2.01×10^{-1}	1.42×10^{-1}	1.64×10^{-1}	1.54×10^{-1}
	0.8	$1.09 \times 10^{+0}$	2.42×10^{-1}	1.70×10^{-1}	1.77×10^{-1}	1.68×10^{-1}
	0.9	9.49×10^{-1}	1.87×10^{-1}	1.37×10^{-1}	1.30×10^{-1}	1.24×10^{-1}
	1.1	9.44×10^{-1}	1.29×10^{-1}	1.03×10^{-1}	1.17×10^{-1}	1.12×10^{-1}
	1.3	$1.06 \times 10^{+0}$	2.15×10^{-1}	1.54×10^{-1}	1.35×10^{-1}	1.29×10^{-1}
	1.5	9.66×10^{-1}	2.27×10^{-1}	1.55×10^{-1}	1.16×10^{-1}	1.11×10^{-1}
	1.7	9.11×10^{-1}	1.25×10^{-2}	1.25×10^{-2}	1.93×10^{-1}	1.76×10^{-1}
	1.9	8.55×10^{-1}	1.21×10^{-2}	1.21×10^{-2}	1.78×10^{-1}	1.62×10^{-1}
	2.1	8.00×10^{-1}	1.22×10^{-2}	1.22×10^{-2}	1.63×10^{-1}	1.48×10^{-1}
	2.3	7.79×10^{-1}	1.29×10^{-2}	1.29×10^{-2}	1.53×10^{-1}	1.38×10^{-1}
	2.50	7.47×10^{-1}	1.36×10^{-2}	1.36×10^{-2}	1.45×10^{-1}	1.29×10^{-1}
	2.7	6.90×10^{-1}	1.46×10^{-2}	1.46×10^{-2}	1.30×10^{-1}	1.15×10^{-1}
	2.9	6.47×10^{-1}	1.60×10^{-2}	1.60×10^{-2}	1.21×10^{-1}	1.07×10^{-1}
	3.1	6.23×10^{-1}	1.79×10^{-2}	1.79×10^{-2}	1.15×10^{-1}	1.01×10^{-1}
	3.3	5.84×10^{-1}	1.97×10^{-2}	1.97×10^{-2}	1.07×10^{-1}	9.44×10^{-2}
	3.5	5.59×10^{-1}	2.21×10^{-2}	2.21×10^{-2}	1.02×10^{-1}	8.99×10^{-2}
3.7	6.18×10^{-1}	2.59×10^{-2}	2.59×10^{-2}	1.10×10^{-1}	9.58×10^{-2}	
3.9	4.93×10^{-1}	2.76×10^{-2}	2.73×10^{-2}	9.03×10^{-2}	7.96×10^{-2}	
4.2	4.74×10^{-1}	2.12×10^{-2}	2.12×10^{-2}	8.55×10^{-2}	7.50×10^{-2}	
4.8	3.95×10^{-1}	2.75×10^{-2}	2.71×10^{-2}	7.24×10^{-2}	6.38×10^{-2}	
5.5	3.07×10^{-1}	3.38×10^{-2}	3.32×10^{-2}	6.03×10^{-2}	5.41×10^{-2}	
6.5	3.10×10^{-1}	5.85×10^{-2}	5.67×10^{-2}	6.06×10^{-2}	5.43×10^{-2}	
7.5	4.68×10^{-1}	1.27×10^{-1}	1.22×10^{-1}	8.56×10^{-2}	7.53×10^{-2}	
8.5	4.22×10^{-1}	2.23×10^{-1}	1.50×10^{-1}	9.42×10^{-2}	8.68×10^{-2}	
0–10%	0.3	$1.08 \times 10^{+0}$	5.30×10^{-1}	2.72×10^{-1}	4.37×10^{-1}	4.03×10^{-1}
	0.5	$1.18 \times 10^{+0}$	4.65×10^{-1}	2.64×10^{-1}	4.37×10^{-1}	4.07×10^{-1}
	0.6	$1.14 \times 10^{+0}$	3.36×10^{-1}	2.15×10^{-1}	3.18×10^{-1}	2.98×10^{-1}
	0.7	$1.17 \times 10^{+0}$	3.36×10^{-1}	2.18×10^{-1}	2.96×10^{-1}	2.77×10^{-1}
	0.8	$1.00 \times 10^{+0}$	2.17×10^{-1}	1.55×10^{-1}	1.80×10^{-1}	1.70×10^{-1}
	0.8	$1.07 \times 10^{+0}$	2.40×10^{-1}	1.71×10^{-1}	1.78×10^{-1}	1.69×10^{-1}
	0.9	$1.01 \times 10^{+0}$	2.03×10^{-1}	1.50×10^{-1}	1.42×10^{-1}	1.35×10^{-1}
	1.1	9.36×10^{-1}	1.32×10^{-1}	1.06×10^{-1}	1.19×10^{-1}	1.14×10^{-1}
	1.3	$1.13 \times 10^{+0}$	2.29×10^{-1}	1.64×10^{-1}	1.36×10^{-1}	1.30×10^{-1}
	1.5	$1.00 \times 10^{+0}$	2.35×10^{-1}	1.61×10^{-1}	1.15×10^{-1}	1.10×10^{-1}
	1.7	8.71×10^{-1}	1.38×10^{-2}	1.38×10^{-2}	1.81×10^{-1}	1.65×10^{-1}
	1.9	8.08×10^{-1}	1.42×10^{-2}	1.42×10^{-2}	1.65×10^{-1}	1.49×10^{-1}
	2.1	7.29×10^{-1}	1.50×10^{-2}	1.50×10^{-2}	1.46×10^{-1}	1.32×10^{-1}
	2.30	6.88×10^{-1}	1.66×10^{-2}	1.66×10^{-2}	1.34×10^{-1}	1.20×10^{-1}
	2.5	6.42×10^{-1}	1.83×10^{-2}	1.83×10^{-2}	1.24×10^{-1}	1.11×10^{-1}
	2.7	6.18×10^{-1}	2.07×10^{-2}	2.07×10^{-2}	1.15×10^{-1}	1.01×10^{-1}
	2.9	5.83×10^{-1}	2.31×10^{-2}	2.31×10^{-2}	1.07×10^{-1}	9.44×10^{-2}
	3.1	4.84×10^{-1}	2.54×10^{-2}	2.51×10^{-2}	9.01×10^{-2}	7.97×10^{-2}
	3.3	4.97×10^{-1}	2.91×10^{-2}	2.88×10^{-2}	9.07×10^{-2}	7.99×10^{-2}
	3.5	4.64×10^{-1}	3.29×10^{-2}	3.25×10^{-2}	8.47×10^{-2}	7.45×10^{-2}
3.7	4.89×10^{-1}	3.77×10^{-2}	3.72×10^{-2}	8.72×10^{-2}	7.62×10^{-2}	
3.9	4.83×10^{-1}	4.39×10^{-2}	4.31×10^{-2}	8.60×10^{-2}	7.51×10^{-2}	
4.2	3.62×10^{-1}	3.13×10^{-2}	3.08×10^{-2}	6.62×10^{-2}	5.83×10^{-2}	
4.8	2.71×10^{-1}	3.97×10^{-2}	3.88×10^{-2}	5.15×10^{-2}	4.59×10^{-2}	
5.5	2.49×10^{-1}	5.13×10^{-2}	4.95×10^{-2}	4.94×10^{-2}	4.44×10^{-2}	
6.5	8.61×10^{-2}	7.88×10^{-2}	5.88×10^{-2}	2.58×10^{-2}	2.47×10^{-2}	
7.5	5.14×10^{-1}	2.49×10^{-1}	1.68×10^{-1}	9.17×10^{-2}	8.02×10^{-2}	
8.5	4.60×10^{-1}	4.12×10^{-1}	2.18×10^{-1}	9.77×10^{-2}	8.92×10^{-2}	

TABLE XIV: $R_{\text{AuAu}}(p_T^e)$ for (upper) 10–20% and (lower) 20–40% centrality classes.

Centrality	p_T^e	R_{AuAu}	Stat. error (+)	Stat. error (–)	Sys. error (+)	Sys. error (–)
10–20%	0.3	9.72×10^{-1}	4.76×10^{-1}	2.46×10^{-1}	3.66×10^{-1}	3.34×10^{-1}
	0.5	$1.05 \times 10^{+0}$	4.13×10^{-1}	2.36×10^{-1}	3.62×10^{-1}	3.33×10^{-1}
	0.6	$1.09 \times 10^{+0}$	3.22×10^{-1}	2.08×10^{-1}	2.92×10^{-1}	2.72×10^{-1}
	0.7	$1.12 \times 10^{+0}$	3.22×10^{-1}	2.11×10^{-1}	2.71×10^{-1}	2.53×10^{-1}
	0.8	$1.01 \times 10^{+0}$	2.20×10^{-1}	1.58×10^{-1}	1.77×10^{-1}	1.67×10^{-1}
	0.8	$1.19 \times 10^{+0}$	2.67×10^{-1}	1.91×10^{-1}	1.95×10^{-1}	1.85×10^{-1}
	0.9	9.82×10^{-1}	1.99×10^{-1}	1.48×10^{-1}	1.34×10^{-1}	1.28×10^{-1}
	1.1	9.76×10^{-1}	1.39×10^{-1}	1.12×10^{-1}	1.21×10^{-1}	1.16×10^{-1}
	1.3	$1.22 \times 10^{+0}$	2.45×10^{-1}	1.76×10^{-1}	1.48×10^{-1}	1.41×10^{-1}
	1.5	$1.07 \times 10^{+0}$	2.51×10^{-1}	1.72×10^{-1}	1.21×10^{-1}	1.16×10^{-1}
	1.7	9.74×10^{-1}	1.66×10^{-2}	1.66×10^{-2}	2.00×10^{-1}	1.81×10^{-1}
	1.9	9.25×10^{-1}	1.75×10^{-2}	1.75×10^{-2}	1.85×10^{-1}	1.67×10^{-1}
	2.1	8.68×10^{-1}	1.90×10^{-2}	1.90×10^{-2}	1.70×10^{-1}	1.52×10^{-1}
	2.3	8.61×10^{-1}	2.15×10^{-2}	2.15×10^{-2}	1.63×10^{-1}	1.45×10^{-1}
	2.50	7.78×10^{-1}	2.37×10^{-2}	2.37×10^{-2}	1.47×10^{-1}	1.30×10^{-1}
	2.7	7.00×10^{-1}	2.63×10^{-2}	2.63×10^{-2}	1.29×10^{-1}	1.14×10^{-1}
	2.9	6.39×10^{-1}	2.93×10^{-2}	2.93×10^{-2}	1.17×10^{-1}	1.03×10^{-1}
	3.1	6.43×10^{-1}	3.40×10^{-2}	3.37×10^{-2}	1.15×10^{-1}	1.01×10^{-1}
	3.3	5.67×10^{-1}	3.74×10^{-2}	3.70×10^{-2}	1.02×10^{-1}	8.97×10^{-2}
	3.5	5.88×10^{-1}	4.34×10^{-2}	4.29×10^{-2}	1.04×10^{-1}	9.11×10^{-2}
3.7	6.65×10^{-1}	5.23×10^{-2}	5.16×10^{-2}	1.15×10^{-1}	9.98×10^{-2}	
3.9	4.19×10^{-1}	5.11×10^{-2}	5.01×10^{-2}	7.68×10^{-2}	6.77×10^{-2}	
4.2	5.18×10^{-1}	4.31×10^{-2}	4.24×10^{-2}	9.10×10^{-2}	7.91×10^{-2}	
4.8	3.89×10^{-1}	5.48×10^{-2}	5.35×10^{-2}	7.02×10^{-2}	6.15×10^{-2}	
5.5	3.14×10^{-1}	6.79×10^{-2}	6.54×10^{-2}	5.99×10^{-2}	5.33×10^{-2}	
6.5	4.50×10^{-1}	1.35×10^{-1}	1.27×10^{-1}	8.07×10^{-2}	7.07×10^{-2}	
7.5	8.39×10^{-1}	3.88×10^{-1}	2.53×10^{-1}	1.42×10^{-1}	1.22×10^{-1}	
8.5	7.03×10^{-1}	6.32×10^{-1}	3.08×10^{-1}	1.40×10^{-1}	1.26×10^{-1}	
20–40%	0.3	7.65×10^{-1}	3.76×10^{-1}	1.96×10^{-1}	2.82×10^{-1}	2.56×10^{-1}
	0.5	9.79×10^{-1}	3.87×10^{-1}	2.21×10^{-1}	3.21×10^{-1}	2.93×10^{-1}
	0.6	9.47×10^{-1}	2.80×10^{-1}	1.81×10^{-1}	2.43×10^{-1}	2.24×10^{-1}
	0.7	$1.21 \times 10^{+0}$	3.48×10^{-1}	2.27×10^{-1}	2.89×10^{-1}	2.69×10^{-1}
	0.8	9.71×10^{-1}	2.12×10^{-1}	1.53×10^{-1}	1.70×10^{-1}	1.60×10^{-1}
	0.8	$1.23 \times 10^{+0}$	2.75×10^{-1}	1.96×10^{-1}	1.97×10^{-1}	1.86×10^{-1}
	0.9	9.56×10^{-1}	1.94×10^{-1}	1.45×10^{-1}	1.32×10^{-1}	1.26×10^{-1}
	1.1	$1.06 \times 10^{+0}$	1.49×10^{-1}	1.21×10^{-1}	1.29×10^{-1}	1.24×10^{-1}
	1.3	$1.29 \times 10^{+0}$	2.61×10^{-1}	1.87×10^{-1}	1.51×10^{-1}	1.43×10^{-1}
	1.5	$1.17 \times 10^{+0}$	2.75×10^{-1}	1.88×10^{-1}	1.33×10^{-1}	1.27×10^{-1}
	1.7	$1.08 \times 10^{+0}$	1.81×10^{-2}	1.81×10^{-2}	2.25×10^{-1}	2.04×10^{-1}
	1.9	$1.03 \times 10^{+0}$	1.89×10^{-2}	1.89×10^{-2}	2.09×10^{-1}	1.90×10^{-1}
	2.1	9.81×10^{-1}	2.05×10^{-2}	2.05×10^{-2}	1.95×10^{-1}	1.75×10^{-1}
	2.3	9.30×10^{-1}	2.27×10^{-2}	2.27×10^{-2}	1.80×10^{-1}	1.61×10^{-1}
	2.5	8.91×10^{-1}	2.54×10^{-2}	2.54×10^{-2}	1.71×10^{-1}	1.52×10^{-1}
	2.7	8.46×10^{-1}	2.84×10^{-2}	2.84×10^{-2}	1.55×10^{-1}	1.37×10^{-1}
	2.9	8.20×10^{-1}	3.24×10^{-2}	3.24×10^{-2}	1.49×10^{-1}	1.31×10^{-1}
	3.1	7.86×10^{-1}	3.68×10^{-2}	3.68×10^{-2}	1.41×10^{-1}	1.24×10^{-1}
	3.3	7.50×10^{-1}	4.17×10^{-2}	4.13×10^{-2}	1.34×10^{-1}	1.17×10^{-1}
	3.5	6.77×10^{-1}	4.63×10^{-2}	4.57×10^{-2}	1.21×10^{-1}	1.06×10^{-1}
3.7	7.26×10^{-1}	5.44×10^{-2}	5.37×10^{-2}	1.27×10^{-1}	1.11×10^{-1}	
3.9	5.87×10^{-1}	5.73×10^{-2}	5.63×10^{-2}	1.05×10^{-1}	9.24×10^{-2}	
4.2	5.80×10^{-1}	4.54×10^{-2}	4.48×10^{-2}	1.02×10^{-1}	8.92×10^{-2}	
4.8	5.26×10^{-1}	5.96×10^{-2}	5.84×10^{-2}	9.28×10^{-2}	8.09×10^{-2}	
5.5	4.01×10^{-1}	7.31×10^{-2}	7.08×10^{-2}	7.52×10^{-2}	6.67×10^{-2}	
6.5	4.36×10^{-1}	1.32×10^{-1}	1.25×10^{-1}	8.01×10^{-2}	7.06×10^{-2}	
7.5	2.75×10^{-1}	2.80×10^{-1}	1.62×10^{-1}	5.65×10^{-2}	5.13×10^{-2}	
8.5	4.54×10^{-1}	5.42×10^{-1}	2.58×10^{-1}	9.85×10^{-2}	9.03×10^{-2}	

TABLE XV: $R_{\text{AuAu}}(p_T^e)$ for (upper) 40–60% and (lower) 60–92% centrality classes.

Centrality	p_T^e	R_{AuAu}	Stat. error (+)	Stat. error (-)	Sys. error (+)	Sys. error (-)
40–60%	0.3	7.27×10^{-1}	3.65×10^{-1}	2.01×10^{-1}	3.23×10^{-1}	3.03×10^{-1}
	0.5	$1.04 \times 10^{+0}$	4.18×10^{-1}	2.46×10^{-1}	3.39×10^{-1}	3.09×10^{-1}
	0.6	$1.17 \times 10^{+0}$	3.51×10^{-1}	2.32×10^{-1}	2.99×10^{-1}	2.76×10^{-1}
	0.7	$1.10 \times 10^{+0}$	3.28×10^{-1}	2.23×10^{-1}	2.62×10^{-1}	2.44×10^{-1}
	0.8	9.89×10^{-1}	2.28×10^{-1}	1.72×10^{-1}	1.80×10^{-1}	1.71×10^{-1}
	0.8	$1.25 \times 10^{+0}$	2.94×10^{-1}	2.18×10^{-1}	2.01×10^{-1}	1.90×10^{-1}
	0.9	$1.17 \times 10^{+0}$	2.49×10^{-1}	1.92×10^{-1}	1.59×10^{-1}	1.51×10^{-1}
	1.1	$1.09 \times 10^{+0}$	1.68×10^{-1}	1.41×10^{-1}	1.38×10^{-1}	1.32×10^{-1}
	1.3	$1.49 \times 10^{+0}$	3.02×10^{-1}	2.17×10^{-1}	1.83×10^{-1}	1.75×10^{-1}
	1.5	$1.40 \times 10^{+0}$	3.28×10^{-1}	2.25×10^{-1}	1.53×10^{-1}	1.46×10^{-1}
	1.7	$1.22 \times 10^{+0}$	2.79×10^{-2}	2.79×10^{-2}	2.57×10^{-1}	2.34×10^{-1}
	1.9	$1.19 \times 10^{+0}$	3.11×10^{-2}	3.11×10^{-2}	2.45×10^{-1}	2.22×10^{-1}
	2.1	$1.17 \times 10^{+0}$	3.57×10^{-2}	3.57×10^{-2}	2.33×10^{-1}	2.10×10^{-1}
	2.3	$1.14 \times 10^{+0}$	4.15×10^{-2}	4.15×10^{-2}	2.22×10^{-1}	1.99×10^{-1}
	2.50	$1.13 \times 10^{+0}$	5.78×10^{-2}	4.78×10^{-2}	2.16×10^{-1}	1.92×10^{-1}
	2.7	9.93×10^{-1}	5.34×10^{-2}	5.34×10^{-2}	1.86×10^{-1}	1.65×10^{-1}
	2.9	8.81×10^{-1}	6.01×10^{-2}	5.95×10^{-2}	1.66×10^{-1}	1.48×10^{-1}
	3.1	$1.04 \times 10^{+0}$	7.32×10^{-2}	7.24×10^{-2}	1.85×10^{-1}	1.62×10^{-1}
	3.3	8.49×10^{-1}	8.00×10^{-2}	7.88×10^{-2}	1.56×10^{-1}	1.37×10^{-1}
	3.5	8.54×10^{-1}	9.19×10^{-2}	9.03×10^{-2}	1.54×10^{-1}	1.35×10^{-1}
3.7	$1.01 \times 10^{+0}$	1.11×10^{-1}	1.09×10^{-1}	1.75×10^{-1}	1.51×10^{-1}	
3.9	7.66×10^{-1}	1.16×10^{-1}	1.13×10^{-1}	1.38×10^{-1}	1.21×10^{-1}	
4.2	8.12×10^{-1}	9.27×10^{-2}	9.09×10^{-2}	1.41×10^{-1}	1.23×10^{-1}	
4.8	9.03×10^{-1}	1.33×10^{-1}	1.30×10^{-1}	1.54×10^{-1}	1.32×10^{-1}	
5.5	5.82×10^{-1}	1.52×10^{-1}	1.45×10^{-1}	1.07×10^{-1}	9.39×10^{-2}	
6.5	7.75×10^{-1}	3.28×10^{-1}	2.40×10^{-1}	1.35×10^{-1}	1.17×10^{-1}	
7.5	2.79×10^{-1}	6.24×10^{-1}	2.57×10^{-1}	6.06×10^{-2}	5.56×10^{-2}	
60–92%	0.3	$1.11 \times 10^{+0}$	5.69×10^{-1}	3.26×10^{-1}	4.14×10^{-1}	3.76×10^{-1}
	0.5	8.62×10^{-1}	3.80×10^{-1}	2.56×10^{-1}	3.25×10^{-1}	3.04×10^{-1}
	0.6	$1.01 \times 10^{+0}$	3.39×10^{-1}	2.51×10^{-1}	2.78×10^{-1}	2.59×10^{-1}
	0.7	$1.25 \times 10^{+0}$	4.05×10^{-1}	3.00×10^{-1}	2.95×10^{-1}	2.75×10^{-1}
	0.8	9.38×10^{-1}	2.64×10^{-1}	2.21×10^{-1}	1.86×10^{-1}	1.77×10^{-1}
	0.8	8.77×10^{-1}	2.78×10^{-1}	2.40×10^{-1}	1.74×10^{-1}	1.68×10^{-1}
	0.9	$1.01 \times 10^{+0}$	2.77×10^{-1}	2.39×10^{-1}	1.49×10^{-1}	1.43×10^{-1}
	1.1	$1.14 \times 10^{+0}$	2.22×10^{-1}	1.97×10^{-1}	1.44×10^{-1}	1.38×10^{-1}
	1.3	$1.40 \times 10^{+0}$	2.84×10^{-1}	2.05×10^{-1}	1.85×10^{-1}	1.78×10^{-1}
	1.5	$1.30 \times 10^{+0}$	3.07×10^{-1}	2.12×10^{-1}	1.67×10^{-1}	1.61×10^{-1}
	1.7	$1.19 \times 10^{+0}$	4.64×10^{-2}	4.64×10^{-2}	2.60×10^{-1}	2.39×10^{-1}
	1.9	$1.12 \times 10^{+0}$	5.43×10^{-2}	5.43×10^{-2}	2.44×10^{-1}	2.24×10^{-1}
	2.1	8.56×10^{-1}	6.06×10^{-2}	6.06×10^{-2}	1.98×10^{-1}	1.84×10^{-1}
	2.3	8.95×10^{-1}	7.38×10^{-2}	7.31×10^{-2}	1.97×10^{-1}	1.81×10^{-1}
	2.50	9.55×10^{-1}	8.84×10^{-2}	8.73×10^{-2}	2.00×10^{-1}	1.82×10^{-1}
	2.7	8.21×10^{-1}	9.93×10^{-2}	9.78×10^{-2}	1.73×10^{-1}	1.58×10^{-1}
	2.9	7.66×10^{-1}	1.14×10^{-1}	1.12×10^{-1}	1.61×10^{-1}	1.47×10^{-1}
	3.1	9.24×10^{-1}	1.40×10^{-1}	1.37×10^{-1}	1.79×10^{-1}	1.60×10^{-1}
	3.3	7.01×10^{-1}	1.51×10^{-1}	1.47×10^{-1}	1.45×10^{-1}	1.32×10^{-1}
	3.5	7.92×10^{-1}	1.78×10^{-1}	1.73×10^{-1}	1.54×10^{-1}	1.38×10^{-1}
3.7	9.76×10^{-1}	2.19×10^{-1}	2.11×10^{-1}	1.78×10^{-1}	1.57×10^{-1}	
3.9	7.62×10^{-1}	2.36×10^{-1}	2.26×10^{-1}	1.45×10^{-1}	1.29×10^{-1}	
4.2	6.33×10^{-1}	1.73×10^{-1}	1.66×10^{-1}	1.21×10^{-1}	1.08×10^{-1}	
4.8	2.50×10^{-1}	1.92×10^{-1}	1.80×10^{-1}	6.38×10^{-2}	6.00×10^{-2}	
5.5	1.72×10^{-1}	2.89×10^{-1}	1.83×10^{-1}	5.35×10^{-2}	5.14×10^{-2}	
6.5	5.20×10^{-1}	6.86×10^{-1}	3.62×10^{-1}	1.01×10^{-1}	8.99×10^{-2}	

TABLE XVI: p_T^e -integrated nuclear modification factors R_{AuAu} .

p_T^e (GeV/c)	N_{part}	R_{AuAu}	Stat. error (+)	Stat error (-)	Sys. error (\pm)	Common fractional error from $p+p$ cross section.
> 0.30	14.5	$1.04 \times 10^{+0}$	7.64×10^{-2}	7.55×10^{-2}	3.88×10^{-1}	$+2.325 \times 10^{-1} - 1.587 \times 10^{-1}$
	59.95	9.86×10^{-1}	3.90×10^{-2}	3.86×10^{-2}	2.53×10^{-1}	
	140.4	9.43×10^{-1}	2.29×10^{-2}	2.26×10^{-2}	2.19×10^{-1}	
	234.6	$1.03 \times 10^{+0}$	2.38×10^{-2}	2.35×10^{-2}	2.43×10^{-1}	
	325.2	$1.09 \times 10^{+0}$	2.20×10^{-2}	2.17×10^{-2}	2.71×10^{-1}	
> 0.60	14.5	$1.08 \times 10^{+0}$	7.16×10^{-2}	7.09×10^{-2}	3.49×10^{-1}	$+1.309 \times 10^{-1} - 1.037 \times 10^{-1}$
	59.95	$1.14 \times 10^{+0}$	3.71×10^{-2}	3.67×10^{-2}	2.08×10^{-1}	
	140.4	$1.10 \times 10^{+0}$	2.11×10^{-2}	2.09×10^{-2}	1.71×10^{-1}	
	234.6	$1.05 \times 10^{+0}$	2.11×10^{-2}	2.08×10^{-2}	1.59×10^{-1}	
	325.2	$1.03 \times 10^{+0}$	1.84×10^{-2}	1.81×10^{-2}	1.59×10^{-1}	
> 0.8	14.5	$1.07 \times 10^{+0}$	7.27×10^{-2}	7.17×10^{-2}	3.33×10^{-1}	$+1.096 \times 10^{-1} - 8.989 \times 10^{-2}$
	59.95	$1.20 \times 10^{+0}$	3.82×10^{-2}	3.77×10^{-2}	1.97×10^{-1}	
	140.4	$1.09 \times 10^{+0}$	2.14×10^{-2}	2.11×10^{-2}	1.49×10^{-1}	
	234.6	$1.04 \times 10^{+0}$	2.13×10^{-2}	2.09×10^{-2}	1.35×10^{-1}	
	325.2	9.77×10^{-1}	1.81×10^{-2}	1.78×10^{-2}	1.29×10^{-1}	
> 2.0	14.5	7.78×10^{-1}	2.96×10^{-2}	2.92×10^{-2}	2.57×10^{-1}	$+1.096 \times 10^{-1} - 8.989 \times 10^{-2}$
	59.95	9.91×10^{-1}	1.66×10^{-2}	1.66×10^{-2}	1.77×10^{-1}	
	140.4	8.13×10^{-1}	9.13×10^{-3}	9.12×10^{-3}	1.25×10^{-1}	
	234.6	7.10×10^{-1}	8.52×10^{-3}	8.50×10^{-3}	1.03×10^{-1}	
	325.2	5.89×10^{-1}	6.64×10^{-3}	6.63×10^{-3}	8.88×10^{-2}	
> 3.0	14.5	7.04×10^{-1}	6.39×10^{-2}	5.98×10^{-2}	2.24×10^{-1}	$+9.049 \times 10^{-2} - 7.662 \times 10^{-2}$
	59.95	8.55×10^{-1}	3.35×10^{-2}	3.25×10^{-2}	1.40×10^{-1}	
	140.4	6.52×10^{-1}	1.67×10^{-2}	1.64×10^{-2}	9.09×10^{-2}	
	234.6	5.40×10^{-1}	1.56×10^{-2}	1.52×10^{-2}	7.12×10^{-2}	
	325.2	4.24×10^{-1}	1.17×10^{-2}	1.14×10^{-2}	5.90×10^{-2}	
> 4.0	14.5	3.99×10^{-1}	1.22×10^{-1}	9.72×10^{-2}	1.31×10^{-1}	$+0.066 \times 10^{-1} - 8.787 \times 10^{-2}$
	59.95	7.59×10^{-1}	6.73×10^{-2}	6.17×10^{-2}	1.22×10^{-1}	
	140.4	5.11×10^{-1}	3.16×10^{-2}	3.00×10^{-2}	7.14×10^{-2}	
	234.6	4.51×10^{-1}	3.09×10^{-2}	2.88×10^{-2}	5.96×10^{-2}	
	325.2	3.03×10^{-1}	2.19×10^{-2}	2.05×10^{-2}	4.42×10^{-2}	

TABLE XVII: Heavy-flavor $e^\pm v_2$ from Au+Au collisions, for the centralities indicated. The p_T is in units of GeV/c.

Centrality	p_T	v_2	stat error	syst error
0-92%	0.546	0.0401	0.00636	0.0189
	0.646	0.0408	0.00712	0.0188
	0.746	0.0385	0.00742	0.0168
	0.847	0.0626	0.00767	0.0145
	0.947	0.0625	0.00861	0.0137
	1.09	0.0563	0.00699	0.0118
	1.29	0.0698	0.00923	0.0115
	1.52	0.092	0.0103	0.0112
	1.83	0.087	0.0152	0.0107
	2.20	0.0692	0.0181	0.00931
	2.70	0.0706	0.0308	0.00842
	3.24	0.0308	0.0465	0.00789
	4.05	0.00986	0.0645	0.00957
	0-10%	0.40	5.13×10^{-2}	1.16×10^{-2}
0.60		3.52×10^{-2}	8.82×10^{-3}	6.77×10^{-3}
0.80		4.13×10^{-2}	9.13×10^{-3}	8.52×10^{-3}
1.05		4.20×10^{-2}	9.65×10^{-3}	5.45×10^{-3}
1.40		4.08×10^{-2}	1.02×10^{-2}	4.96×10^{-3}
1.80		7.05×10^{-3}	1.67×10^{-2}	7.54×10^{-3}
2.50		9.81×10^{-3}	2.22×10^{-2}	6.51×10^{-3}
4.00		1.09×10^{-1}	5.83×10^{-2}	1.31×10^{-2}
10-20%	0.40	2.90×10^{-2}	9.59×10^{-3}	2.03×10^{-2}
	0.60	5.01×10^{-2}	6.52×10^{-3}	1.13×10^{-2}
	0.80	4.78×10^{-2}	6.59×10^{-3}	1.07×10^{-2}
	1.05	6.28×10^{-2}	7.04×10^{-3}	8.54×10^{-3}
	1.40	5.89×10^{-2}	7.65×10^{-3}	8.19×10^{-3}
	1.80	8.25×10^{-2}	1.25×10^{-2}	7.07×10^{-3}
	2.50	9.60×10^{-2}	1.63×10^{-2}	6.34×10^{-3}
	4.00	4.04×10^{-2}	4.06×10^{-2}	5.44×10^{-3}
20-40%	0.40	6.55×10^{-2}	8.01×10^{-3}	1.82×10^{-2}
	0.60	7.34×10^{-2}	5.44×10^{-3}	1.36×10^{-2}
	0.80	1.12×10^{-1}	5.73×10^{-3}	1.05×10^{-2}
	1.05	9.47×10^{-2}	6.30×10^{-3}	1.01×10^{-2}
	1.40	1.30×10^{-1}	7.08×10^{-3}	8.69×10^{-3}
	1.80	1.27×10^{-1}	1.14×10^{-2}	8.36×10^{-3}
	2.50	8.48×10^{-2}	1.47×10^{-2}	8.17×10^{-3}
	4.00	8.15×10^{-2}	3.62×10^{-2}	6.29×10^{-3}
40-60%	0.40	9.14×10^{-2}	1.57×10^{-2}	2.10×10^{-2}
	0.60	1.20×10^{-1}	1.13×10^{-2}	1.49×10^{-2}
	0.80	9.05×10^{-2}	1.31×10^{-2}	1.63×10^{-2}
	1.05	1.12×10^{-1}	1.49×10^{-2}	1.25×10^{-2}
	1.40	1.42×10^{-1}	1.73×10^{-2}	1.07×10^{-2}
	1.80	1.12×10^{-1}	2.88×10^{-2}	1.19×10^{-2}
	2.50	7.66×10^{-2}	3.53×10^{-2}	1.20×10^{-2}
	4.00	6.39×10^{-2}	8.55×10^{-2}	1.03×10^{-2}

TABLE XVIII: Differential invariant cross section of electrons ($(N_{e^+} + N_{e^-})/2$) from heavy-flavor decays for 200 GeV $p + p$ collisions at midrapidity. The p_T^e is in units of GeV/c. The cross section and corresponding errors are in units of mb

p_T^e	Invariant yield	Stat. error	Sys. error
0.350	1.36×10^{-2}	4.45×10^{-3}	5.95×10^{-3}
0.400	6.05×10^{-3}	1.70×10^{-3}	2.39×10^{-3}
0.550	3.36×10^{-3}	7.56×10^{-4}	1.04×10^{-3}
0.650	1.81×10^{-3}	3.98×10^{-4}	5.12×10^{-4}
0.750	1.30×10^{-3}	2.28×10^{-4}	2.59×10^{-4}
0.850	7.50×10^{-4}	1.35×10^{-4}	1.35×10^{-4}
0.950	5.61×10^{-4}	9.14×10^{-5}	7.85×10^{-5}
1.10	3.18×10^{-4}	3.77×10^{-5}	3.64×10^{-5}
1.30	1.26×10^{-4}	2.10×10^{-5}	1.50×10^{-5}
1.50	6.58×10^{-5}	1.25×10^{-5}	6.56×10^{-6}
1.70	3.97×10^{-5}	2.07×10^{-6}	3.32×10^{-6}
1.90	1.99×10^{-5}	1.18×10^{-6}	1.65×10^{-6}
2.10	1.14×10^{-5}	7.44×10^{-7}	8.96×10^{-7}
2.30	6.83×10^{-6}	4.96×10^{-7}	5.09×10^{-7}
2.50	3.98×10^{-6}	3.63×10^{-7}	3.05×10^{-7}
2.70	2.44×10^{-6}	6.49×10^{-8}	2.80×10^{-7}
2.90	1.63×10^{-6}	4.77×10^{-8}	1.77×10^{-7}
3.10	1.05×10^{-6}	3.53×10^{-8}	1.10×10^{-7}
3.30	7.21×10^{-7}	2.73×10^{-8}	7.31×10^{-8}
3.50	5.04×10^{-7}	2.15×10^{-8}	4.89×10^{-8}
3.70	3.45×10^{-7}	1.70×10^{-8}	3.30×10^{-8}
3.90	2.37×10^{-7}	1.36×10^{-8}	2.25×10^{-8}
4.25	1.33×10^{-7}	5.95×10^{-9}	1.22×10^{-8}
4.75	6.13×10^{-8}	3.73×10^{-9}	5.45×10^{-9}
5.50	2.06×10^{-8}	1.79×10^{-9}	1.85×10^{-9}
6.50	6.62×10^{-9}	9.26×10^{-10}	5.72×10^{-10}
7.50	1.70×10^{-9}	5.73×10^{-10}	1.60×10^{-10}
8.50	9.72×10^{-10}	5.16×10^{-10}	8.07×10^{-11}

-
- [1] K. Adcox et al. (PHENIX Collaboration), Nucl. Phys. **A757**, 184 (2005).
- [2] I. Arsene et al. (BRAHMS Collaboration), Nucl. Phys. **A757**, 1 (2005).
- [3] B. B. Back et al. (PHOBOS Collaboration), Nucl. Phys. **A757**, 28 (2005).
- [4] J. Adams et al. (STAR Collaboration), Nucl. Phys. **A757**, 102 (2005).
- [5] K. Adcox et al. (PHENIX Collaboration), Phys. Rev. Lett. **88**, 022301 (2002).
- [6] S. S. Adler et al. (PHENIX Collaboration), Phys. Rev. Lett. **91**, 072301 (2003).
- [7] J. Adams et al. (STAR Collaboration), Phys. Rev. Lett. **91**, 172302 (2003).
- [8] P. Huovinen et al., Phys. Lett. **B503**, 58 (2001).
- [9] R. J. Fries, B. Muller, C. Nonaka, and S. A. Bass, Phys. Rev. C **68**, 044902 (2003).
- [10] S. S. Adler et al. (PHENIX Collaboration), Phys. Rev. Lett. **91**, 182301 (2003).
- [11] J. Adams et al. (STAR Collaboration), Phys. Rev. Lett. **92**, 052302 (2004).
- [12] A. Adare et al. (PHENIX Collaboration), Phys. Rev. Lett. **98**, 162301 (2007).
- [13] P. Arnold, J. Lenaghan, G. D. Moore, and L. G. Yaffe, Phys. Rev. Lett. **94**, 072302 (2005).
- [14] D. Molnar and S. A. Voloshin, Phys. Rev. Lett. **91**, 092301 (2003).
- [15] Y. L. Dokshitzer and D. E. Kharzeev, Phys. Lett. **B519**, 199 (2001).
- [16] N. Armesto, A. Dainese, C. A. Salgado, and U. A. Wiedemann, Phys. Rev. D **71**, 054027 (2005).
- [17] M. Cacciari, hep-ph/0407187 (2004).
- [18] D. Acosta et al., Phys. Rev. Lett. **91**, 241804 (2003).
- [19] F. W. Busser et al., Phys. Lett. **B53**, 212 (1974).
- [20] C. Albajar et al. (UA1 Collaboration), Phys. Lett. **B256**, 121 (1991).
- [21] O. Botner et al. (UA2 Collaboration), Phys. Lett. **B236**, 488 (1990).
- [22] D. Acosta et al. (CDF collaboration), Phys. Rev. D **65**, 052007 (2002).
- [23] S. Abachi et al. (D0 collaboration), Phys. Rev. Lett. **74**, 3548 (1995).
- [24] K. Adcox et al. (PHENIX Collaboration), Phys. Rev. Lett. **88**, 192303 (2002).
- [25] S. S. Adler et al. (PHENIX Collaboration), Phys. Rev. Lett. **96**, 032001 (2006).
- [26] S. S. Adler et al. (PHENIX Collaboration), Phys. Rev. Lett. **94**, 082301 (2005).
- [27] S. S. Adler et al. (PHENIX Collaboration), Phys. Rev. C **72**, 024901 (2005).
- [28] S. S. Adler et al. (PHENIX Collaboration), Phys. Rev. Lett. **96**, 032301 (2006).
- [29] B. I. Abelev et al. (STAR Collaboration), Phys. Rev. Lett. **98**, 192301 (2007; Erratum to be published).
- [30] A. Adare et al. (PHENIX Collaboration), Phys. Rev. Lett. **97**, 252002 (2006).
- [31] A. Adare et al. (PHENIX Collaboration), Phys. Rev. Lett. **98**, 172301 (2007).
- [32] K. Adcox et al. (PHENIX Collaboration), Nucl. Instrum. Methods **A499**, 469 (2003).
- [33] S. H. Aronson et al. (PHENIX Collaboration), Nucl. Instrum. Methods **A499**, 480 (2003).
- [34] K. Adcox et al. (PHENIX Collaboration), Nucl. Instrum. Methods **A499**, 489 (2003).
- [35] M. Aizawa et al. (PHENIX Collaboration), Nucl. Instrum. Methods **A499**, 508 (2003).
- [36] L. Aphecetche et al. (PHENIX Collaboration), Nucl. Instrum. Methods **A499**, 521 (2003).
- [37] M. Allen et al. (PHENIX Collaboration), Nucl. Instrum. Methods **A499**, 549 (2003).
- [38] C. Adler et al. (PHENIX Collaboration), Nucl. Instrum. Methods **A470**, 488 (2001).
- [39] Y. Akiba et al. (PHENIX Collaboration), Nucl. Instrum. Methods **A433**, 143 (1999).
- [40] S. S. Adler et al. (PHENIX Collaboration), Phys. Rev. Lett. **96**, 012304 (2006).
- [41] R. J. Glauber and G. Matthiae, Nucl. Phys. **B21**, 135 (1970).
- [42] D. Ben-Tzvi and M. B. Sandler, Patt. Rec. Lett. **11**, 167 (1990).
- [43] M. Ohlsson et al., Comp. Phys. Comm. **71**, 77 (1992).
- [44] J. T. Myrhiem and L. Bugge, Nucl. Instrum. Methods **A160**, 43 (1979).
- [45] A. Chikanian et al., Nucl. Instrum. Methods **A371**, 480 (1996).
- [46] *GEANT 3.2.1 Manual* (1994), CERN W5013, URL <http://wwwasdoc.web.cern.ch/wwwasdoc/pdfdir/geant.pdf>.
- [47] T. Sjöstrand et al., Comp. Phys. Comm. **135**, 238 (2001).
- [48] A. Adare et al. (PHENIX Collaboration), Phys. Rev. Lett. **101**, 232301 (2008).
- [49] S. S. Adler et al. (PHENIX Collaboration), Phys. Rev. C **69**, 034909 (2004).
- [50] S. S. Adler et al. (PHENIX Collaboration), Phys. Rev. Lett. **96**, 202301 (2006).
- [51] R. Averbek, pHENIX Internal Note (2001).
- [52] V. G. Ryabov, Nucl. Instrum. Meth. **A419**, 363 (1998).
- [53] S. S. Adler et al. (PHENIX Collaboration), Phys. Rev. D **71**, 071102 (2005).
- [54] S. S. Adler et al. (PHENIX Collaboration), Phys. Rev. Lett. **94**, 232301 (2005).
- [55] A. Adare et al. (PHENIX Collaboration), Phys. Rev. C **81**, 034911 (2010).
- [56] A. Adare et al., (PHENIX Collaboration), arXiv:0912.2082 [hep-ex] (2010).
- [57] A. Adare et al. (PHENIX Collaboration), Phys. Lett. **B670**, 313 (2009).
- [58] A. Frawley, T. Ullrich, and R. Vogt, Phys.Rept. **462**, 125 (2008).
- [59] W. Vogelsang, private communication (2009).
- [60] J. Pumplin et al., Journ. High Energy Phys. **0207**, 012 (2002).
- [61] A. Adare et al. (PHENIX Collaboration), Phys. Rev. Lett. **98**, 232301 (2007).
- [62] Y.-S. Tsai, Rev. Mod. Phys. **Vol. 46**, No.4, 815 (October 1974).
- [63] W. M. Yao et al., J. Phys. **33**, 1 (2006).
- [64] J.-Y. Ollitrault (1997), arXiv:nucl-ex/9711003.
- [65] A. M. Poskanzer and S. A. Voloshin, Phys. Rev. C **58**, 1671 (1998).
- [66] M. Cacciari, P. Nason, and R. Vogt, Phys. Rev. Lett. **95**, 122001 (2005).
- [67] S. S. Adler et al. (PHENIX Collaboration), Phys. Rev.

- D **74**, 072002 (2006).
- [68] M. L. Mangano, P. Nason, and G. Ridolfi, Nucl. Phys. **B405**, 507 (1993).
- [69] H. L. Lai et al., Eur. Phys. J. **C12**, 375 (2000).
- [70] A. Adare et al. (PHENIX Collaboration), Phys. Rev. Lett. **103**, 082002 (2009).
- [71] N. Armesto et al., Phys. Lett. **B637**, 362 (2006).
- [72] S. Wicks et al., nucl-th/0512076 (2006).
- [73] M. G. Mustafa, Phys. Rev. C **72**, 014905 (2005).
- [74] G. D. Moore and D. Teaney, Phys. Rev. C **71**, 064904 (2005).
- [75] H. van Hees, V. Greco, and R. Rapp, Phys. Rev. C **73**, 034913 (2006).
- [76] H. van Hees, M. Mannarelli, V. Greco, and R. Rapp, Phys. Rev. Lett. **100**, 192301 (2008).
- [77] C. Y. Wong, Phys. Rev. C **72**, 034906 (2005).
- [78] A. Adil and I. Vitev, Phys. Lett. **B649**, 139 (2007).
- [79] B. I. Abelev et al. (STAR Collaboration), Phys. Rev. Lett. **97**, 152301 (2006).
- [80] S. H. Lee, K. Ohnishi, S. Yasui, I. K. Yoo, and C. M. Ko, Phys. Rev. Lett. **100**, 222301 (2008).
- [81] G. Martinez-Garcia, S. Gadrat, and P. Crochet, Phys. Lett. **B663**, 533 (2008).
- [82] P. B. Gossiaux and J. Aichelin, Phys. Rev. C **78**, 014904 (2008).
- [83] P. B. Gossiaux, R. Bierkanndt, and J. Aichelin, Phys. Rev. C **79**, 044906 (2009).
- [84] P. B. Gossiaux and J. Aichelin, J. Phys. **G36**, 064028 (2009), arXiv:0901.2462 [nucl-th].
- [85] D. E. Kharzeev, arXiv:0806.0358 [hep-ph] (2008).
- [86] V. Greco, C. Ko, and R. Rapp, Phys. Lett. **B595**, 202 (2004).
- [87] B. Zhang, L. W. Chen, and C. M. Ko, Phys. Rev. C **72**, 024906 (2005).
- [88] G. Policastro, D. T. Son, and A. O. Starinets, Journ. High Energy Phys. **09**, 043 (2002).
- [89] P. Danielewicz and M. Gyulassy, Phys. Rev. D **31**, 53 (1985).
- [90] P. K. Kovtun, D. T. Son, and A. O. Starinets, Phys. Rev. Lett. **94**, 111601 (2005).
- [91] R. Rapp and H. van Hees, arXiv:0803.0901 [hep-ph] (2008).
- [92] R. A. Lacey et al., Phys. Rev. Lett. **98**, 092301 (2007).
- [93] H.-J. Drescher, A. Dumitru, C. Gombeaud, and J.-Y. Ollitrault, Phys. Rev. C **76**, 024905 (2007).
- [94] S. Gavin and M. Abdel-Aziz, Phys. Rev. Lett. **97**, 162302 (2006).
- [95] A. Dumitru, E. Molnar, and Y. Nara, Phys. Rev. C **76**, 024910 (2007).
- [96] P. Romatschke and U. Romatschke, Phys. Rev. Lett. **99**, 172301 (2007).
- [97] M. Luzum and P. Romatschke, Phys. Rev. C **78**, 034915 (2008), Erratum *ibid* **79**, 039903 (2009).
- [98] A. Adare et al. (PHENIX Collaboration), arXiv:0706.3034 [nucl-ex] (2007).